Contents

1 Introduction **1**

1.1 Motivations 1

1.2 Research program 2

2 Experimental methods **5**

2.1 Heavy-ion fusion-evaporation reactions 5

2.2 Detector assemblies 7

2.3 Experiments 9

2.3.1 The NORDBALL experiments 9

2.3.2 The EUROGAM II experiment 11

2.4 The NORDBALL array 13

2.4.1 The Germanium detectors 13

2.4.2 The ancillary detectors 15

2.4.3 The data acquisition system 17

2.5 The EUROGAM II array 19

2.5.1 The detector arrangement 19

2.5.2 Electronics and data acquisition 22

2.6 Data analysis 23

2.6.1 Preparation of data 24

2.6.2 Construction of the level schemes 28

3 Nuclear models **35**

3.1 The shell model 36

3.2 The interacting boson-fermion model 38

3.3 The cranked shell model 39

4 Spectroscopy of ^{108,109,110}Te nuclei **45**

4.1 Earlier studies 45

4.2 Experimental results 46

4.2.1 The ^{108}Te nucleus 46
4.2.2 The ^{109}Te nucleus 49
4.2.3 The ^{110}Te nucleus 55
4.3 Discussion 60
4.3.1 The ^{108}Te and ^{110}Te nuclei 60
4.3.2 The ^{109}Te nucleus 66

5 Structure of ^{98}Pd and ^{100}Pd nuclei 71
5.1 Previous studies 71
5.2 Experimental results 72
5.2.1 The level scheme of ^{98}Pd 72
5.2.2 The level scheme of ^{100}Pd 77
5.3 Discussion 86
5.3.1 The ^{98}Pd nucleus 86
5.3.2 The ^{100}Pd nucleus 87

6 Summary 97
6.1 Neutron deficient Te nuclei 97
6.2 Neutron deficient Pd nuclei 99
6.3 Perspectives 100

7 Összefoglalás 103
7.1 Neutronhiányos Te atommagok 103
7.2 Neutronhiányos Pd atommagok 105

A Acknowledgements 117

B Publications 119

List of Figures

2.1 Schematic illustration of the decay of the compound nucleus after a heavy-ion reaction. Encircled regions indicate the excitations of the residual nuclei after the emission of 3–5 particles (p). 6

2.2 Population pattern of the residual nuclei from the ^{58}Ni + ^{54}Fe reaction at 270 MeV bombarding energy. The shaded squares indicate nuclei investigated in this work. 10

2.3 Population pattern of the residual nuclei from the ^{58}Ni + ^{50}Cr reaction at 261 MeV bombarding energy. The shaded squares indicate nuclei investigated in this work. 12

2.4 The NORDBALL array. 13

2.5 Schematic view of the NORDBALL experimental setup. 14

2.6 Schematic picture of the Si detector setup: a) forward detectors, b) backward detectors. The beam axis passed through holes in the central pentagons. 16

2.7 Block diagram of the NORDBALL electronic circuit. 18

2.8 The EUROGAM II array. 20

2.9 Schematic view of the EUROGAM II clover detector. 21

2.10 The architecture of the EUROGAM electronics and data acquisition system. (taken from Ref. [38].) 22

2.11 The relative efficiency of the Ge detectors in NORDBALL and EUROGAM II arrays. The EUROGAM II array has a larger relative detection efficiency for high energy γ-rays. 25

2.12 Si ball energy spectra for different detector positions (rings). 27

2.13 Neutron ZC vs. TOF matrix used for off-line neutron-γ separation. . 28

2.14 Experimental spectrum obtained in the ^{54}Fe(^{28}Ni,2p) reaction channel and the cleaned spectrum for ^{110}Te, after the subtraction. A background supression of $\sim$3 orders of magnitude was achieved [43]. . 32

2.15 Schematics of Compton scattering between the segments of the clover detector. 34

3.1 Single-particle levels in the shell model: a) harmonic-oscillator potential, b) Woods-Saxon potential, c) inclusion of the spin-orbit term, d) number of nucleons in each orbital, e) its symbols and f) parity, g) number of nucleons at shell closures. (Figure is taken from Ref. [51].) 37

4.1 Total projection spectrum of ^{108}Te obtained from the cleaned 2p2n-gated matrix. Transitions labelled by C are known contaminants. . . 46

4.2 Assignment of γ-rays to the 2p2n+^{108}Te reaction channel (open circles) based on the comparison of their intensity ratios for different neutron and proton multiplicity with those of known γ-ray lines (filled circles). 47

4.3 The experimental level scheme of ^{108}Te obtained in our work. Only those transitions are shown in the level scheme the placement of which could be firmly establish from the coincidence analysis. 48

4.4 Total projection spectrum of ^{109}Te obtained from the sum of the 1n-, 1p1n-, and 2p1n-gated γ-γ matrices, after subtracting the contaminating channels. 50

4.5 Typical γ-γ coincidence spectra of ^{109}Te obtained from the cleaned 2p1n-gated matrix. Transitions are labelled by their energy, in keV. . 52

4.6 Proposed level scheme of ^{109}Te as obtained from the ^{54}Fe(^{58}Ni,2pnγ)^{109}Te reaction. All the spin values are tentative, and are given relative to the assumed ground state $I^{\pi} = 5/2^{+}$. The unfilled part of the 98 keV arrow reperesent the intensity of the conversion electrons, assuming pure M1 multipolarity. 54

4.7 Projection spectrum of ^{110}Te obtained from the sum of the 1p- and 2p-gated γ-γ matrices, after subtracting the contaminating channels. 55

4.8 Experimental intensity ratios for different proton multiplicities. Comparisons with results obtained for known γ-rays (filled symbols) confirm the assignment of the 658 keV transition to ^{110}Te (open symbol). 56

4.9 Typical γ-γ coincidence spectrum obtained from the sum of the 1p- and 2p- gated matrices. 57

4.10 Experimental level scheme of ^{110}Te deduced from this work. The width of the arrows are proprotional to the relative intensity of the transition. 58

4.11 Systematics of yrast states in the even-even Te isotopes as a function of the neutron number. 61

4.12 Neutron single-particle levels for ^{110}Te. The levels are labeled by their Nilsson quantum numbers $[Nn_z\Lambda]\Omega^\pi$. 62

4.13 Total Routhian Surface calculation for the lowest lying (π,α)=(+,0), vacuum configuration at $\hbar\omega = 0.31$ MeV; two minima are seen: $\beta_2 \approx 0.15$, $\gamma \approx 1°$ and $\beta_2 \approx 0.15$, $\gamma \approx 111°$. 63

4.14 Quasi-neutron Routhians for β_2=0.15, β_4=0.0 and γ=0°. 64

4.15 Experimental spin alignments i_x and experimental Routhians e' for the bands 2 and 3 of ^{110}Te plotted as a function of $\hbar\omega$ (circles=band 3; squares=band 2). The Harris parameters used for the reference configuration are J_0=7$\hbar^2$MeV^{-1} and J_1=20$\hbar^4$MeV^{-3}, and the value of the quantum number K used in the calculations are 0 for band 3 and 3 for band 2. 65

4.16 Comparison of the experimental levels with the theoretical calculations based on the interacting boson–fermion model. On the right hand side of the figure the main components of the calculated wave functions are also given. 68

4.17 Comparison of experimental and calculated spin I_x for the observed negative-parity band in ^{109}Te. 69

5.1 Gamma-ray gated spectra corresponding to ^{98}Pd obtained from the 2p2α-gated γ-γ matrix. 73

5.2 Proposed level scheme of ^{98}Pd. Tentative spin and parity assignments are shown in parentheses. 74

5.3 Selected γ-ray gated spectra of ^{100}Pd from the ^{58}Ni(^{50}Cr,4p1α) and the ^{70}Zn(^{36}S,6n) reactions. 80

5.4 Proposed level scheme of ^{100}Pd. The widths of the arrows are proportional to the observed γ-ray intensities. Below the 8716 keV level the intensities have been taken from the NORDBALL experiment, above that they have been taken from the EUROGAM II experiment, normalized with respect to the intensity of the 1071 keV transition. . . . 83

5.5 Comparison of the experimental (top) and theoretical (bottom) deviations of the band state energies from that predicted by the rotational model for a rigid body. Theoretical deviations are calculated for the region of band terminations. 88

5.6 Cranked Woods-Saxon quasiparticle Routhians for protons (top) and neutrons (bottom) calculated for ^{100}Pd as functions of rotational frequency $\hbar\omega$. Solid (dashed) and dotted (dashed-dotted) lines correspond to positive (negative) parity states with signature $\alpha = +1/2$ and $\alpha = -1/2$ ($\alpha = -1/2$ and $\alpha = +1/2$), respectively. The labels indicate the asymptotic quantum numbers of the Nilsson states to which the Routians correspond at $\hbar\omega = 0$. 90

5.7 I_x versus rotational frequency for the ground state band (a) and for the negative parity side-band (b) of ^{100}Pd (solid lines). The theoretical values (dashed line) are taken from the TRS calculation. 91

5.8 Development of octupole collectivity for the ground-state band calculated by use of Total Routhian Surface method. 96

List of Tables

2.1 Detector setup of the NORDBALL and EUROGAM II arrays. 9

2.2 Angular positions of the Ge detectors with respect to the beam axis in our NORDBALL configuration. 14

2.3 Angular positions of the Si detectors with respect to the beam direction in NORDBALL. The detector numbering corresponds to that of Fig. 2.6. 15

2.4 List of experimental parameters recorded on magnetic tape during the NORDBALL experiments. 18

2.5 Trigger conditions used in the NORDBALL experiments. 19

2.6 Physical quantities extracted from experimental data and the related data analysis techniques used in this work. See the text for a more detailed description of the specific methods and techniques. 24

3.1 Limiting cases in the IBFM. 40

4.1 Energies, relative intensities, angular correlation ratios R_{ang} and proposed multipolarities of γ-rays assigned to ^{108}Te. 49

4.2 Energies, relative intensities, angular correlation ratios R_{ang}, and angular momentum ΔI transferred by the γ-ray transitions assigned to ^{109}Te. Suggested spins and parities of the initial and final states of the transitions are given in the last column. 51

4.3 Energies, relative intensities, γ-γ angular correlation ratios, and spin assignments of γ-rays assigned to ^{110}Te. 59

5.1 Energies, intensities, angular correlation ratios and spin assignments of γ-rays assigned to ^{98}Pd. 75

5.2 Energies, relative intensities and angular correlation ratios for γ-ray transitions assigned to ^{100}Pd from the ^{50}Cr(^{58}Ni,4p1α)^{100}Pd reaction. The linear polarisation values P were determined from the ^{70}Zn(^{36}S,6n)^{100}Pd reaction. The proposed spin and parity for the levels is also listed. 77

5.3 Energies, relative intensities, DCO ratios and linear polarisation P for γ-rays assigned to the decay of ^{100}Pd states lying above 9 MeV from the ^{70}Zn+^{36}S reaction. The intensity of the 1071.2 keV transition has been taken as reference. 81

5.4 The reduced E1 transition probabilities in ^{100}Pd estimated from branching ratios compared to known values in ^{117,119}Cd. 95

Chapter 1

Introduction

1.1 Motivations

One of the most interesting regions in the nuclear chart is that around the doubly magic ^{100}Sn and neighbouring nuclei. This region has since long been the subject of many experimental and theoretical investigations. There are several reasons which make it so attractive for nuclear studies.

The ^{100}Sn is the heaviest self-conjugate (i.e. with the same number of neutrons and protons), doubly magic nucleus that is believed to have bound states. The observation of excited states in ^{100}Sn and its neighbours would make it possible to determine single-particle and single-hole energy levels around the $N = Z = 50$ doubly closed shell. This is crucial for testing the validity of various nuclear models. Also, due to the fact that both protons and neutrons occupy the same orbitals, enhanced residual interactions are expected, which may lead to important nuclear phenomena. At $N = Z$ the charge independence of the nuclear force may lead to a competition between $T = 1$ n-p pairs and $T = 1$ p-p and n-n pairs. In addition n-p pairs can also have $T = 0$ and this would compete with the $T = 1$ mode [1]. An interesting feature is that the ^{100}Sn lies very close to the so called proton drip-line, where the 'excess' of protons (or 'lack' of neutrons) is so large, that the nucleus is not bound any more with respect to proton emission. Indeed, the binding energy of the proton $g_{9/2}$ shell in ^{100}Sn was predicted to be only about 3 MeV in Ref. [2]. An open question relates to how the proton orbitals are affected by the augmented Coulomb repulsion due to the excess of protons when approaching the region of very neutron deficient nuclei. Yet another aspect to investigate in this region is the onset of deformation when adding more nucleons to the ^{100}Sn core.

Until very recently, most of the experimental information in this region has been

obtained from β-decay studies, and from measurements of proton and α radioactivity. With the advent of large γ-ray detector arrays, the in-beam study of nuclei far from the β-stability line has become a reality. Cross sections of the orders of μb and pb are now within reach. NORDBALL, in the Nordic countries, EUROBALL, in Europe, and GAMMASPHERE in the U.S.A. are examples of such detector systems. The primary goal was to increase the efficiency and resolving power of the γ-ray detection by putting together a large number of Ge detectors and operating them in coincidence (e.g. EUROGAM). Then various types of ancillary detectors were employed together with the Ge detectors to enhance the reaction channel selection (e.g. NORDBALL). The newest arrays like EUROBALL, or the planned EXOGAM, will use a very large number (N>100) of (segmented) Ge detectors, combined with powerful selective devices to achieve unprecedented γ-ray detection sensitivity.

Prior to our work, very limited experimental information for neutron-deficient Te and Pd nuclei in the vicinity of ^{100}Sn were available. Even-mass tellurium, xenon, and barium isotopes with $N \approx Z$ a little above ^{100}Sn ($Z, N \leq 58$) were predicted to exhibit specially strong octupole correlations [3], because orbitals differing in total and orbital momentum by $3\hbar$ approach the Fermi surface for both neutrons and protons, to which the possibility of enhanced proton-neutron interaction is added. In the case of the palladium isotopes, recent theoretical calculations [4] had predicted that in the $A \geq 100$ Ru and Pd nuclei it is possible to follow ground-state rotational bands up to their terminations at and above spin $I = 30\hbar$. Experimental information on such phenomena would result in a better understanding of how the competition of collective and single-particle degrees of freedom will behave, while approaching the proton drip-line. The vast landscape of nuclear phenomena one expects to be revealed in this region, combined with the availability of the experimental tools were the main motivations behind the work presented in this thesis.

1.2 Research program

In the framework of a program for in-beam studies by the NORDBALL collaboration, our research group in the Institute of Nuclear Research (ATOMKI), Debrecen participated in a series of experiments aiming at the production of previously unobserved very neutron deficient nuclei close to ^{100}Sn, and the study of their structure. Specifically, I was involved in the analysis and interpretation of the data from two of such experiments, where I investigated the structure of the neutron deficient ^{108,109,110}Te and ^{98,100}Pd using the NORDBALL detector system. The data from

the first NORDBALL experiment (the Te experiment) was prepared by the research groups of the Physics Department of the Royal Institute of Technology (RIT), in Stockholm and the The Svedberg Laboratory (TSL) of the Uppsala University. The subsequent data analysis with my major contribution, leading to the presented results for the ^{108,109,110}Te nuclei was performed in the ATOMKI in collaboration with the members of the mention research group. For the second NORDBALL experiment (the Pd experiment), I had the opportunity to be involved in the whole data preparation in Stockholm and Uppsala since the first moment, thanks to scholarships from the RIT and TSL. During the preliminary and later data analysis I made a significant contribution to the results obtained for the ^{98,100}Pd nuclei. For the study of the ^{100}Pd we have also used a data set obtained from a EUROGAM II experiment, carried out in collaboration with the Institut des Sciences Nucléaires (ISN), Grenoble, France.

In what follows, Chapter 2 describes the main features of the types of reactions used, the details of the experiments, the NORDBALL and EUROGAM II detector assemblies, and the data analysis techniques employed in this work. Chapter 3 briefly deals with various theoretical models, that were used to interpret the obtained experimental results, including the shell model, the interacting boson-fermion model and the cranking model. Chapter 4 contains an overview of earlier studies, the experimental results obtained in this work and their theoretical interpretation for ^{108,109,110}Te nuclei and so does Chapter 5 for the case of ^{98,100}Pd. A summary of the new obtained results is given in Chapter 6 and 7. Appendix A contains a list of the publications on which this thesis is based.

Chapter 2

Experimental methods

This chapter contains the experimental basis of the work presented in this thesis. The first section introduces the mechanism of the heavy-ion induced fusion-evaporation reactions, widely used for γ-spectroscopy studies of nuclei, e.g. far from the β-stability line. Then various characteristics of the detector assemblies, employed in the experiments with such reactions are summarized. It is followed by a detailed description of the performed experiments and the experimental setups, including the configuration of the specific detector systems we used. Since the major part of my own contributions relates to the experiments performed with the NORDBALL detector system, more emphasis has been put on describing the details of this multi-detector array, its configuration and the related experimental techniques. An experiment with the EUROGAM II spectrometer gave additional information to one set of the NORDBALL data, therefore a short description of that experimental setup and data analysis methods is also provided, enough to understand the presented experimental results. The methods and techniques commonly applied to analyse the huge amounts of data collected by such large detector arrays are finally discussed.

2.1 Heavy-ion fusion-evaporation reactions

In recent nuclear structure studies, heavy-ion induced fusion-evaporation reactions are mostly exploited to reach very high spin states in nuclei and for nuclear mass regions with exotic neutron-to-proton ratios, e.g. very neutron deficient nuclei near the double-magic ^{100}Sn nucleus. In a fusion-evaporation reaction, the incident particle is captured by the target nucleus to form the compound system. The heavier and the more energetic the projectile is, the more excitation energy and angular

momentum the compound nucleus will have. The decay of the compound nucleus (Fig. 2.1) proceeds mainly via neutron and charged particle emission. The relative probability of these decay channels depends on the excess or deficiency of neutrons over protons.

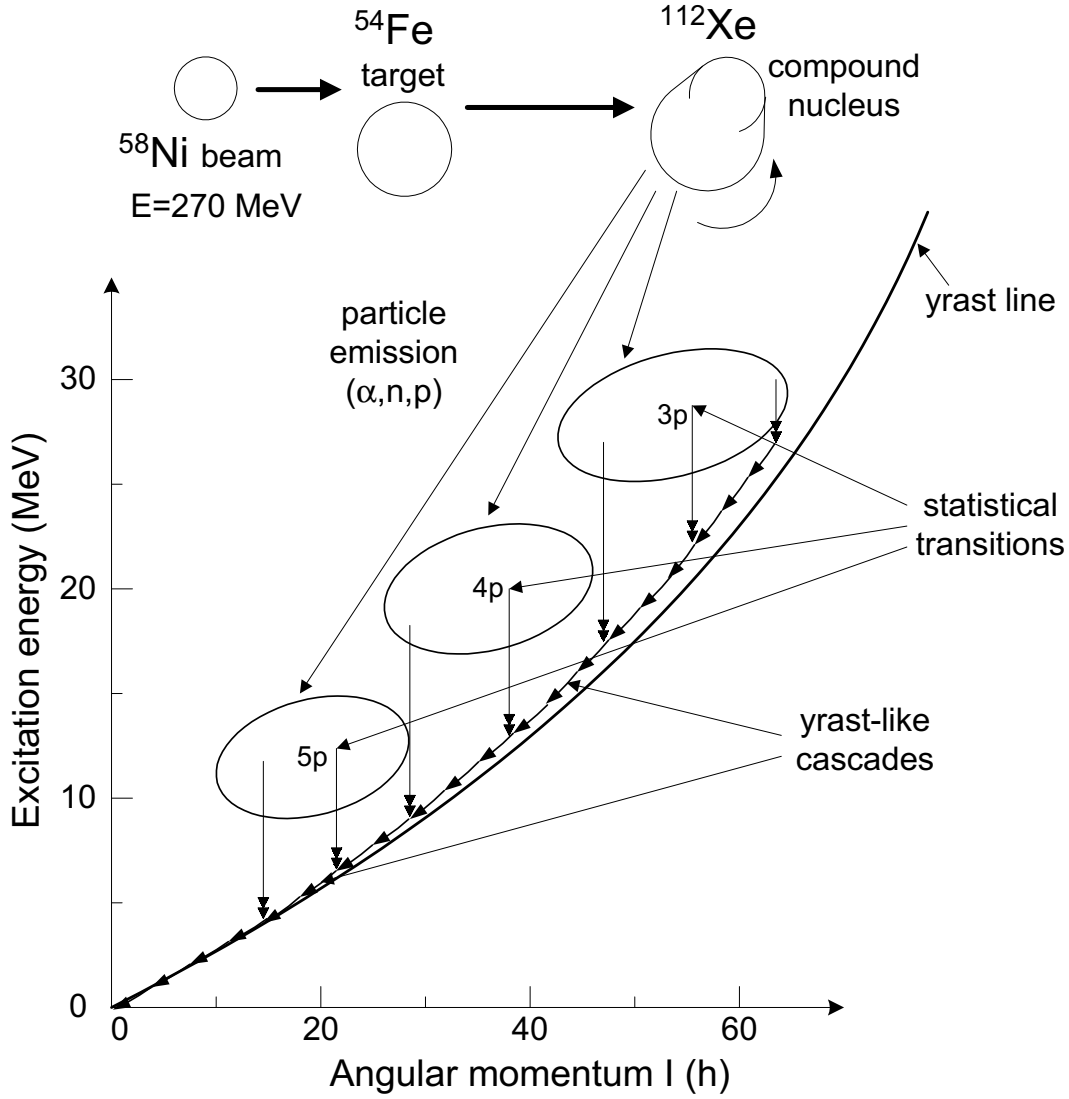

Figure 2.1: Schematic illustration of the decay of the compound nucleus after a heavy-ion reaction. Encircled regions indicate the excitations of the residual nuclei after the emission of 3–5 particles (p).

Neutron evaporation lowers the excitation energy of the intermediate system by the neutron separation energy (∼8 MeV), but takes away only little angular momentum (1$\hbar$ on average). Charged particles need to overcome the Coulomb barrier, and so must be emitted with higher energies. Particle evaporation takes place until the

excitation energy is lowered to the region of one neutron separation energy or less above the yrast line of a given final nucleus[1]. In this region, the decay of states to the ground state of the nucleus proceeds via γ-ray emission. At still high excitation energies above the yrast line, the level density is high, and statistical dipole ($E1$) transitions, bringing the nucleus towards the yrast line, dominate. Closer to the yrast line, the level density is lower and discrete γ-ray transitions can be resolved.

In the experiments discussed in this thesis neutron deficient projectiles were combined with neutron deficient targets to form compound systems very far from the β-stability line, in the Z≈N region near the doubly magic ^{100}Sn. In the decay of these extremely neutron deficient compound nuclei charged-particle emission becomes dominant over neutron evaporation. On the other hand, neutron evaporation takes the system further away from the line of β-stability, thus leading to the most exotic and interesting residual nuclei. Such reactions are characterized by a large number of exit channels (20-30) with cross sections in the range of 1-100 mb.

2.2 Detector assemblies

To study the γ-rays emitted during a fusion-evaporation reaction under the above mentioned conditions, special requirements must be set on the detector system. To extract the underlining physics from the complex γ-ray spectra in the weakest - and hence the most interesting - reaction channels is only possible with the use of efficient, high-resolution γ-ray spectrometers, and special techniques should be applied to preferentially select γ-rays belonging to a particular nucleus. Some of the principles and methods used to increase the performance and selectivity of the γ-detector arrays are discussed below.

The best energy resolution in γ-ray detection so far is achieved with high-purity (HP) Ge detectors. The photopeak efficiency of a Ge detector, however, is normally not so large (∼30% of a 7.6 x 7.6 cm NaI(Tl) crystal at a distance of 25 cm). Typical γ-ray spectra collected with such a detector consist of discrete lines as well as of a continuum background. The background associated with Compton scattering of γ-rays can be greatly reduced by the use of a large detector (Compton-supression shield or CSS), surrounding the Ge detector, the purpose of which is to detect the scattered photons. The signal from the CSS is then used to veto those unwanted events, which include a γ-ray escaping from the Ge detector. The quality of a Ge

[1]The yrast line is the sequence of all states that have the lowest energy for a given angular momentum.

detector can be characterised by the ratio of the photopeak area to the total area of the spectrum. A good Ge detector has a peak-to-total (P/T) ratio of ∼20% for 1 MeV γ-rays. With Compton-suppression, the P/T ratio can be increased up to ∼60%.

Furthermore, the sensitivity[2] of a γ-ray spectrometer can be substantially improved by using an array containing a large number of high-resolution, Compton-suppressed Ge detectors, and operating them to detect γ-rays in coincidence. The requirement that a γ-ray must be detected in coincidence with a specified set of known γ-transitions can then be used to select the events of interest. The more detectors the array has, the higher fold of γ-coincidence can be detected, and the higher the sensitivity of the array will be. However, one has to increase the number of detectors N to very high numbers ($N \geq 50$) in order to achieve a major increase in the detection sensitivity [5].

One may, instead of increasing the number of detectors, implement selective devices to generate a condition that can enhance the γ-rays of interest over a vast number of unrelated γ-rays. For example, the emitted γ-radiation can be detected in coincidence with the evaporated neutrons and charged-particles. By knowing the number and type of particles emitted after the formation of the compound system, the final nucleus from which the γ-rays originates can then be identified. A 4π γ-ray calorimeter, which is able to measure the multiplicity and the total γ-ray energy of an event, can also be used to select a specific reaction channel. This method is based on the fact that different reaction channels has different population distributions in the excitation energy vs. angular momentum plane (see Fig. 2.1). By gating on the multiplicity and sum-energy information it is possible to (roughly) separate γ-rays belonging to different residual nuclei.

The EUROGAM II array, equipped with as much as 54 γ-ray Ge detectors, applied the first approach to reaction channel selection, based on its large number of Ge detectors. The optimum coincidence fold for the array was 4. The second approach was exploited in the NORDBALL setup, where besides the γ-ray Ge detectors, additional ancillary detectors were used to select γ-rays belonging to a certain reaction channel. A comparison of these two arrays regarding the number and type of the used detectors is given in Table 2.1.

[2]The sensitivity of a γ-ray spectrometer is related to the minimum intensity a γ-transition must have, so that it can still be identified in the spectrum.

Table 2.1: Detector setup of the NORDBALL and EUROGAM II arrays.

Array	Ge detectors	Ancillary detectors
NORDBALL	15 coaxial	21-element charged-particle detector
		11-element neutron detector
		30-element sum-energy+multiplicity filter
EUROGAM II	30 coaxial	None
	24 clover	

2.3 Experiments

The new nuclear structure information to be presented in this work are based on the data obtained with the above mentioned detector systems. Two experiments were performed at the Tandem Accelerator Laboratory of the Niels Bohr Institute at Risø, Denmark, using the NORDBALL detector array to investigate nuclei, close to the proton dripline in the vicinity of ^{100}Sn. Out of the several nuclei, produced in these experiments, the structure of the neutron deficient ^{108,109,110}Te, and ^{98,100}Pd were studied by our research group in the ATOMKI, Debrecen. In the case of ^{100}Pd, data from another experiment carried out at the Vivitron accelerator, IReS, Strasbourg by means of the EUROGAM II spectrometer, was also used. The details of these experiments are given below, while the major features of these detector systems are the subject of subsequent sections.

2.3.1 The NORDBALL experiments

The Te experiment

In this experiment, the neutron deficient ^{108}Te, ^{109}Te and ^{110}Te isotopes were studied using the ^{58}Ni + ^{54}Fe $\rightarrow$ ^{112}Xe reaction. A 10 mg/cm^2 thick, self-supporting ^{54}Fe target, enriched to 99.8% was bombarded by a pulsed beam of ^{58}Ni ions, accelerated up to E_{lab}=270 MeV. The beam burst had a width of 10 ns, and the time between two bursts was 160 ns. A total of about 420 million γ-γ coincidence events were recorded on tape during this experiment. These γ-rays originated from a total of 29 residual nuclei, that were identified in the experiment. The obtained population pattern is shown in Fig. 2.2.

The strongest reaction channels involved the emission of 2-4 protons and none or 1 α particles, and accounted for 74% of the total observed yield. Nuclei populated

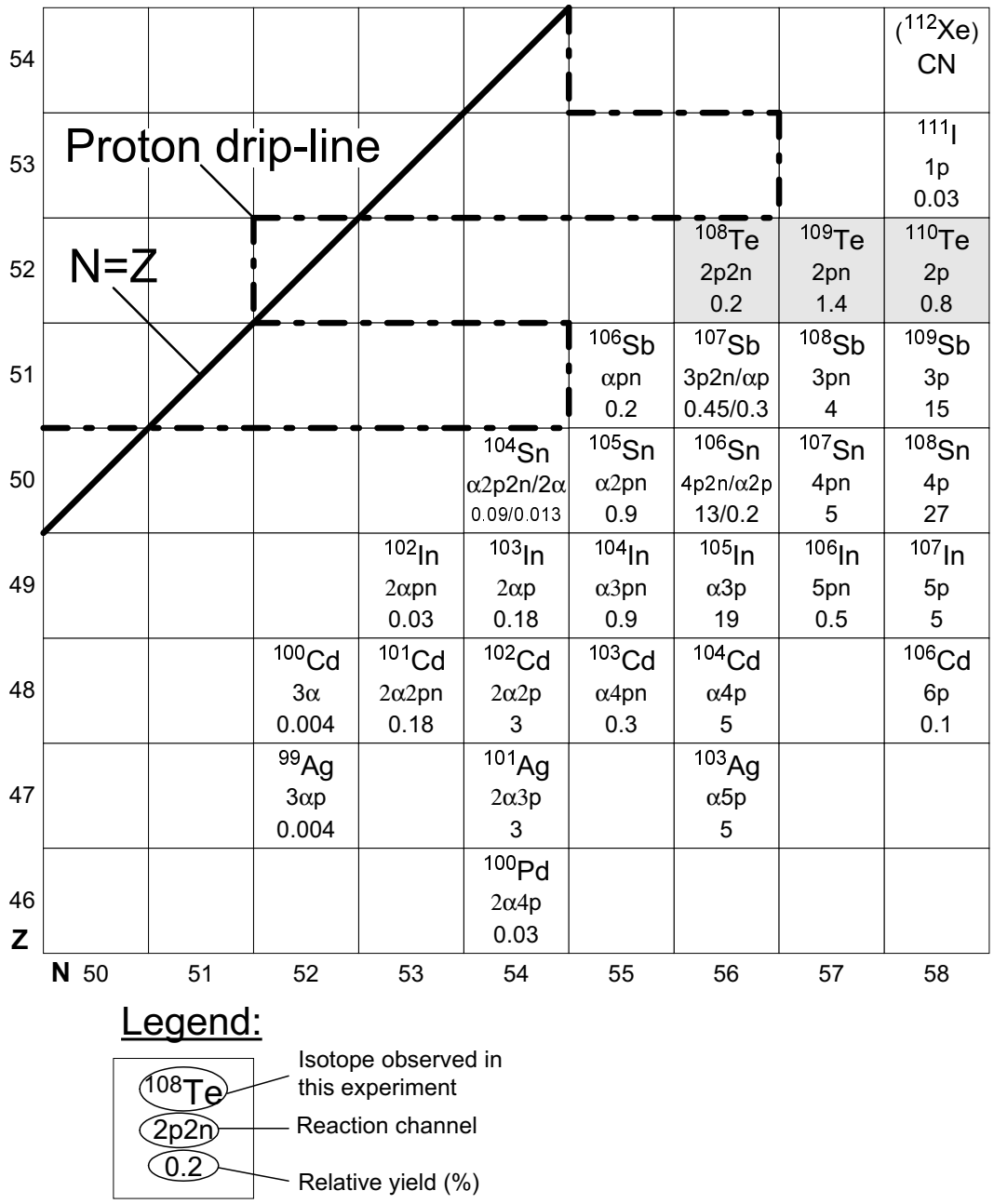

Figure 2.2: Population pattern of the residual nuclei from the ^{58}Ni + ^{54}Fe reaction at 270 MeV bombarding energy. The shaded squares indicate nuclei investigated in this work.

via 1n and 2n channels were observed, but no evidence for the population of 3n channels in this reaction was found. The weakest observed channel was the 3α channel, leading to the ^{100}Cd nucleus, with a relative yield of 0.004%. This would correspond to a cross section of about 20 μb.

In this experiment excited states of ^{102}In [6], ^{106,107,108}Sb, [7, 8], ^{108,109}Te [9, 10]

and ^{111}I [11] were observed for the first time. Furthermore, the level schemes for the majority of the observed nuclei were significantly extended. Experimental results obtained for the ^{108}Te, ^{109}Te and ^{110}Te [12] nuclei are presented in Chapter 4 of this thesis.

The Pd experiment

High-spin states of the neutron deficient ^{98}Pd and ^{100}Pd isotopes were studied in this experiment using the reaction ^{58}Ni+^{50}Cr$\rightarrow$^{108}Te at a beam energy of 261 MeV. Two ^{50}Cr targets were used during the experiment. The targets had a thickness of 4.8 and 3.5 mg/cm^2, and were deposited on Au backings of thickness 11 and 19.5 mg/cm^2, respectively. The targets were enriched to 96.8%, the main contaminant being ^{52}Cr (3.0%).

During the experiment, about $1.2{\cdot}10^9$ γ-γ coincidence events were collected over 25 days of effective beam time. The total data volume stored on magnetic tapes was about 300 GB. Thirty-one nuclei were identified in this experiment, with populations ranging from about 0.001% to 23% of the total yield. The closest nuclei to ^{100}Sn that could be identified were ^{99}Cd [13], and ^{101}In, for which excited states were observed for the first time in this experiment. New nuclear structure information was also obtained for ^{103,105}In [14, 15], $^{101-103}$Cd [16, 17, 18], ^{98,99}Ag [19, 20] and ^{98,100}Pd [21, 22]. The population pattern of the residual nuclei in this experiment is shown in Fig. 2.3. The strongest reaction channel was the 4p channel, leading to ^{104}Cd. The weakest channel to which γ-ray transitions were assigned was ^{99}Cd with a relative yield of 0.008%. The highest observed charged particle multiplicity was 6 (6p,5p1α). The relative yields for the ^{98}Pd and ^{100}Pd nuclei were measured to be 1.9% and 2.5%, respectively. Experimental results for these two nuclei are discussed in Chapter 5 of this thesis.

2.3.2 The EUROGAM II experiment

Excited states of the ^{100}Pd nucleus were also attained in a second experiment, carried out with the EUROGAM II γ-ray spectrometer. The main purpose of this experiment was to search for band terminations in ^{102}Pd and neighbouring nuclei. The high quality of the collected data enabled to extract information for ^{100}Pd in addition to that of the NORDBALL experiment.

The reaction used was ^{70}Zn + ^{36}S at 130 MeV beam energy. The zinc target consisted of two stacked 440 μg/cm^2 thick self-supporting ^{70}Zn foils enriched up to 70%.

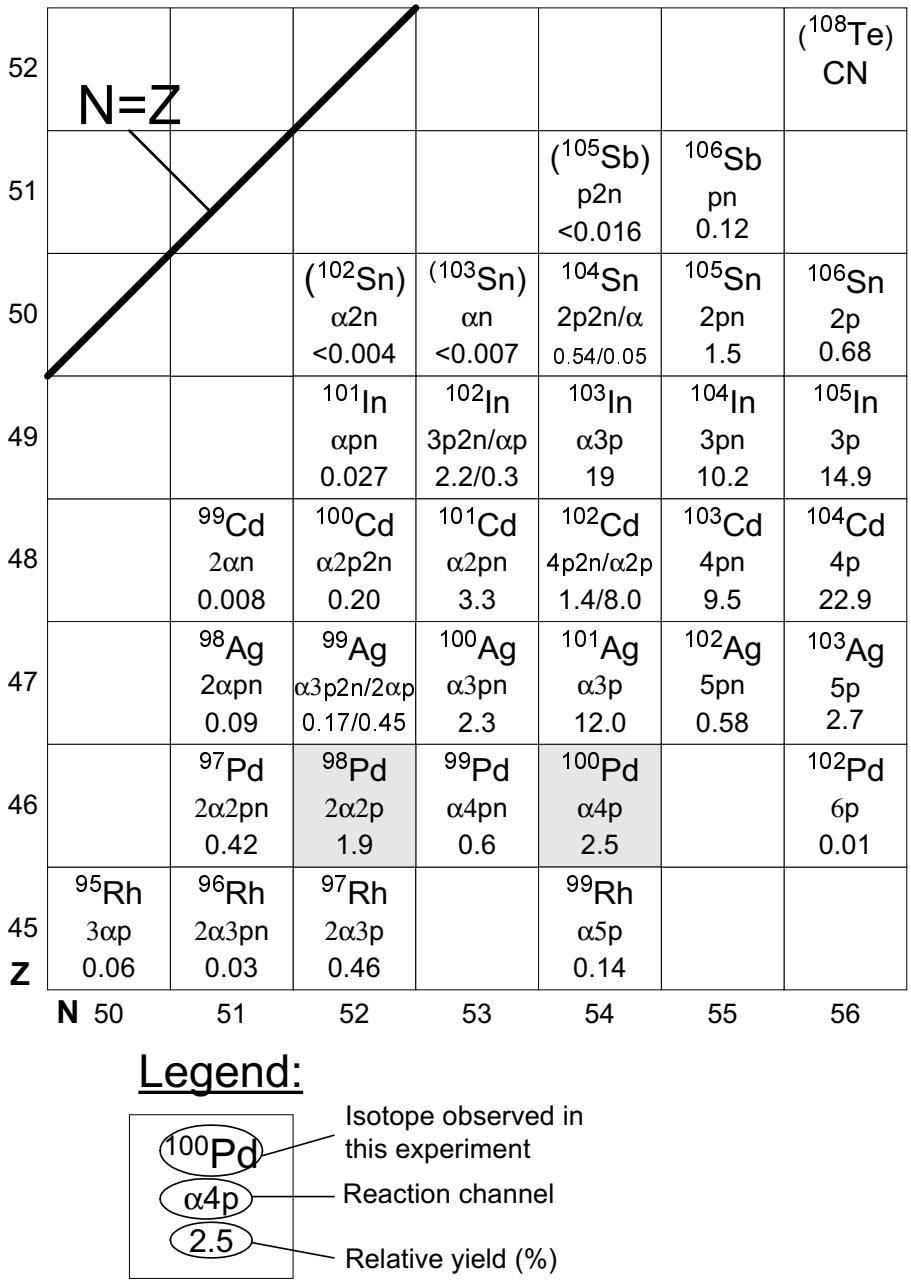

Figure 2.3: Population pattern of the residual nuclei from the ^{58}Ni + ^{50}Cr reaction at 261 MeV bombarding energy. The shaded squares indicate nuclei investigated in this work.

A total of 6 $\times$ 10^8 4-fold coincidence events were collected with the EUROGAM II array (the array will be described in Section 2.5 below).

Out of this experiment terminating bands were identified, e.g. in $^{101-103}$Pd [23, 24, 25] and $^{100-102}$Rh [26, 27, 28] isotopes. The results obtained for the ^{100}Pd nucleus from this experiment are presented in Chapter 5 of this thesis.

2.4 The NORDBALL array

The NORDBALL multi-detector array [29, 30] was built by the Nordic countries to pursue γ-spectroscopy studies. The geometry of the array was a truncated icosahedron, consisting of 12 pentagonal and 20 hexagonal surfaces, used to hold the different types of detectors. A photo of the NORDBALL array is shown in Fig. 2.4.

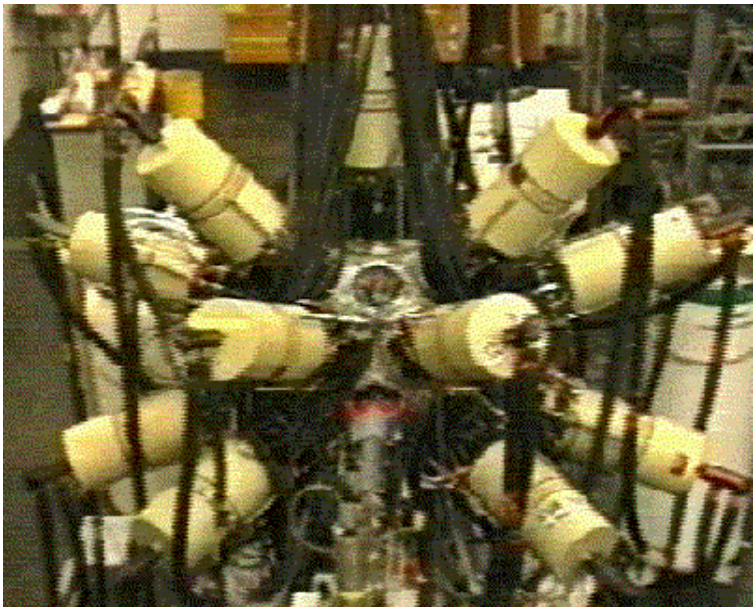

Figure 2.4: The NORDBALL array.

In the experiments discussed in this thesis the NORDBALL array was configured with Compton-supressed Ge detectors, a charged-particle detector array, a neutron detector assembly, and a sum-energy and multiplicity filter. The schematic view of the experimental setup is shown in Fig. 2.5. This setup, besides its high γ-ray detection efficiency, provided an excellent reaction-channel selectivity, due to the combined use of γ-ray, neutron and charged particle detectors. A detailed description of the specific constituents of the array and that of the data acquisition system is given in the remaining part of this section.

2.4.1 The Germanium detectors

The most important elements of the NORDBALL array were the Germanium γ-ray spectrometers. In our setup, NORDBALL was equipped with 15 high-purity

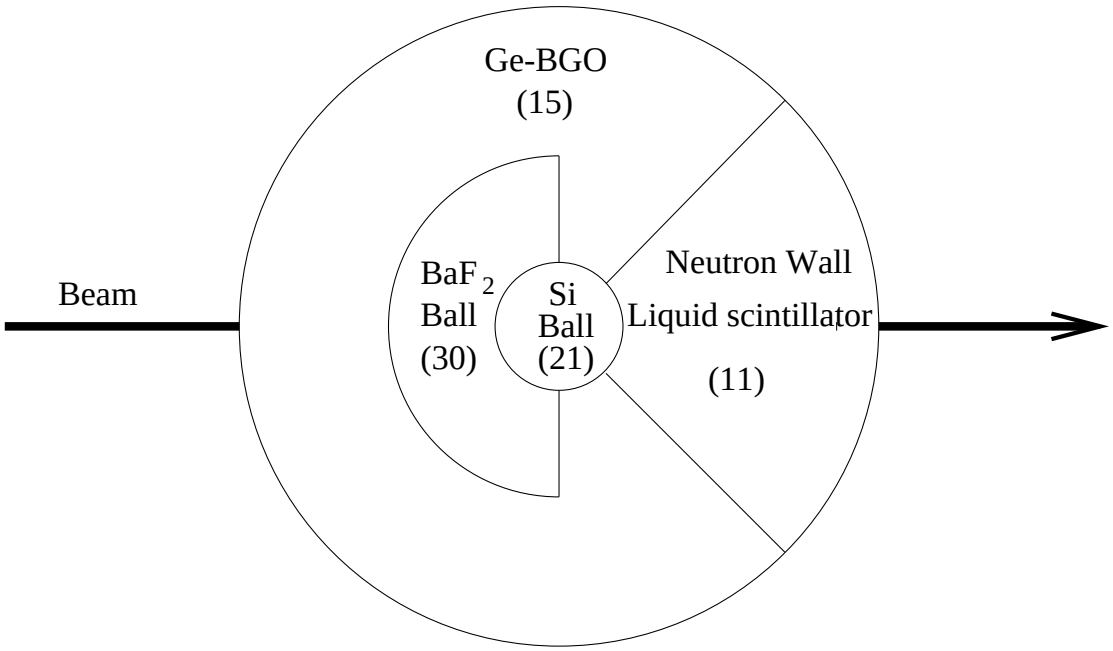

Figure 2.5: Schematic view of the NORDBALL experimental setup.

(HP) coaxial Ge detectors, placed symmetrically around the target in three rings of hexagons at angles 79°, 101° and 143° with respect to the beam direction. The angular positions of the Ge detectors are shown in Table 2.2.

Each ring contained five equidistantly placed detectors. The distance between the detectors and the target was about 18 cm. The energy resolution of the individual Ge detectors was between 1.8 and 3 keV at a γ-ray energy of 1.33 MeV. The relative efficiency of the detectors varied between 20% and 40%. Each Ge detector was surrounded by a Compton-suppression shield made of 12 bismuth germanate (BGO=$Bi_4Ge_3O_{12}$) scintillator crystals [31]. Thick metal absorbers were placed in front of the BGO shields to avoid these being directly hit by γ-rays.

Table 2.2: Angular positions of the Ge detectors with respect to the beam axis in our NORDBALL configuration.

Ring	θ	ϕ				
I	142.6°	54°,	126°,	198°,	270°,	342°
II	100.9°	54°,	126°,	198°,	270°,	342°
III	79.1°	18°,	90°,	162°,	234°,	306°

2.4.2 The ancillary detectors

The charged-particle detectors

In the studied fusion-evaporation reactions, due to the neutron deficient nature of the compound systems, the most probable decay channels favored charged-particle emission. Hence, the detection of charged particles was crucial for the assignment of γ-rays to a certain residual nucleus, based on its atomic number Z.

The identification of emitted protons and α-particles in NORDBALL was accomplished by an array of 21 ΔE-type Si detectors (Si ball) [32]. This array consisted of 12 pentagonal, 170 μm thick silicon wafers put together in a dodecahedron shape of 5cm diameter around the target and covering 90% of the 4π solid angle. Discrimination between protons and α-particles was possible based on the difference in the energy deposited in the Si detectors.

In a heavy-ion fusion-evaporation reaction, the evaporated particles are mainly emitted in the forward angles due to the kinematical effect, thus creating an increased multiple hit probability in that direction. In order to reduce this probability, a higher detector granularity was required in the forward hemisphere. This was achieved by electrically subdividing some of the pentagonal wafers into smaller parts. The very forward pentagon was divided into five triangular detectors, and each of the five pentagons adjacent to the very forward one was subdivided into two symmetrical parts. The remaining six backward pentagons were not divided. Schematically, this is illustrated in Fig. 2.6. The angular positions of the Si detectors with respect to the beam direction are given in Table 2.3.

Table 2.3: Angular positions of the Si detectors with respect to the beam direction in NORDBALL. The detector numbering corresponds to that of Fig. 2.6.

Ring	θ	Detector number				
I	23°	1,	2,	3,	4,	5
II	57°	6,	7,	8,	9,	10
III	78°	11,	12,	13,	14,	15
IV	114°	16,	17,	18,	19,	20
V	180°			21		

The target was placed in the geometrical center of the Si ball. The very backward and the very forward pentagons had holes through which the beam entered and

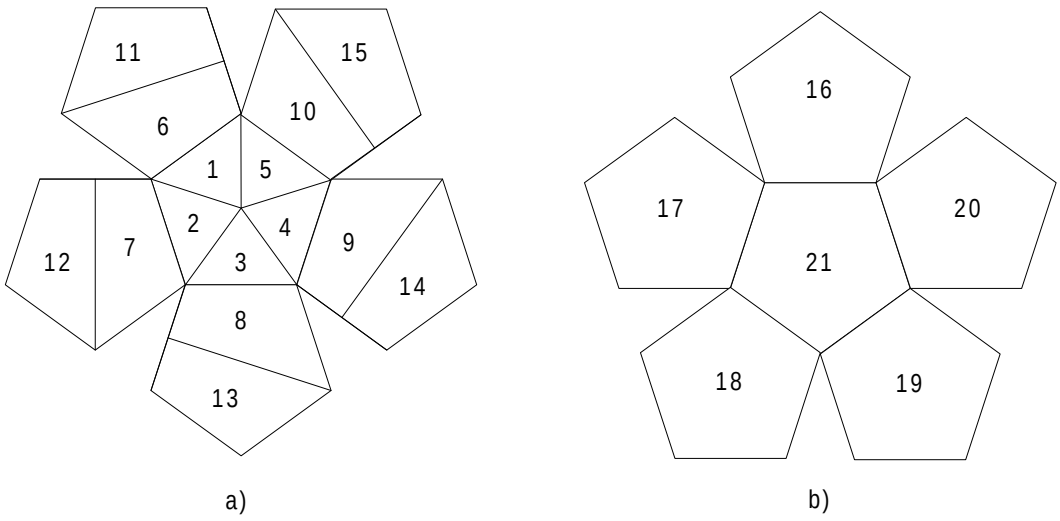

Figure 2.6: Schematic picture of the Si detector setup: a) forward detectors, b) backward detectors. The beam axis passed through holes in the central pentagons.

exited the target area. Since the beam was stopped inside the ball structure, the wafers were protected with aluminum and gold foils against radiation damage from the scattered beam particles. These foils were very carefully chosen for each reaction, so that no beam particles can enter the silicon detectors, but an optimum thickness for the penetration of protons and α particles was obtained. Due to the protective foils, the detection efficiency was strongly reduced to about 60% for protons and 40% for α-particles.

The neutron detectors

The number of neutrons emitted in coincidence with γ-rays in the Ge detectors, and protons or α-particles in the Si detectors, were measured by 11 liquid scintillators occupying five hexagonal and six pentagonal positions in the forward hemisphere of the NORDBALL frame [33]. This information was used to single out the exit channels associated with neutron emission from a certain charged-particle combination.

The thickness of the detectors was 15 cm and the distance between the target and the detector front face was 18 cm. The liquid scintillator containers were made of 2 mm stainless steel and were filled with BC501 organic liquid scintillator. The five pentagon-shaped neutron detectors had a volume of 2.57 l each, while the volume of the six hexagon shaped ones was 3.33 l each. The total efficiency of the neutron wall was $\sim$22%. Apart from the detection efficiency, another important parameter of the neutron detectors was the ability to discriminate between neutrons and γ-

rays. In our experiments efficient on-line separation of neutrons and γ-rays was achieved by means of neutron-γ pulse-shape discrimination using the zero-crossing technique [34]. The discrimination was further improved during the off-line data analysis (see Section 2.6).

The BaF_2 calorimeter

A calorimeter of BaF_2 scintillators (inner ball) [29] was used to enforce selection of specific reaction channels, by measuring the γ-ray sum-energy and multiplicity information. The calorimeter consisted of 30 identical BaF_2 crystals placed in the backward hemisphere of the NORDBALL frame, and forming a semiglobular shell around the target with a thickness of 8 cm and an inner diameter of 12 cm. The Ge spectrometers viewed the target through conically shaped, collimating holes in between the BaF_2 detectors.

The signal from the BaF_2 detectors was used as the time reference for the whole setup. The fast timing properties of BaF_2 provided a time resolution of 500 ps for a pair of detectors and about 1.5 ns for the whole calorimeter.

2.4.3 The data acquisition system

Standard CAMAC and NIM modules were used to process the signals from the detectors and to provide a trigger for the data acquisition system [35]. A schematic block diagram of the electronics is presented in Fig. 2.7. The ADC and FERA modules were read via the VME bus. The readout was performed when a valid trigger signal was generated, and was controlled by the so called Event Builder unit. Data were sent via an optical link to a VAX 4000 workstation. Data was monitored on-line on the workstation and, in parallel, written to EXABYTE magnetic tapes.

The full set of experimental parameters were written to magnetic tape for each valid event generated in the data acquisition system. The parameter list is shown in Table 2.4. A raw data event contained several headers and a label identifying the detector signal. The average length of an event was about 100 bytes.

Trigger conditions

In order to reduce the load on the electronics and the data acquisition system, and to select only 'interesting' events from the point of view of the experiment, a trigger condition was used. The trigger signal was generated by the Programmable Logic Unit (PLU), as a logical function of several input signals, coming from the

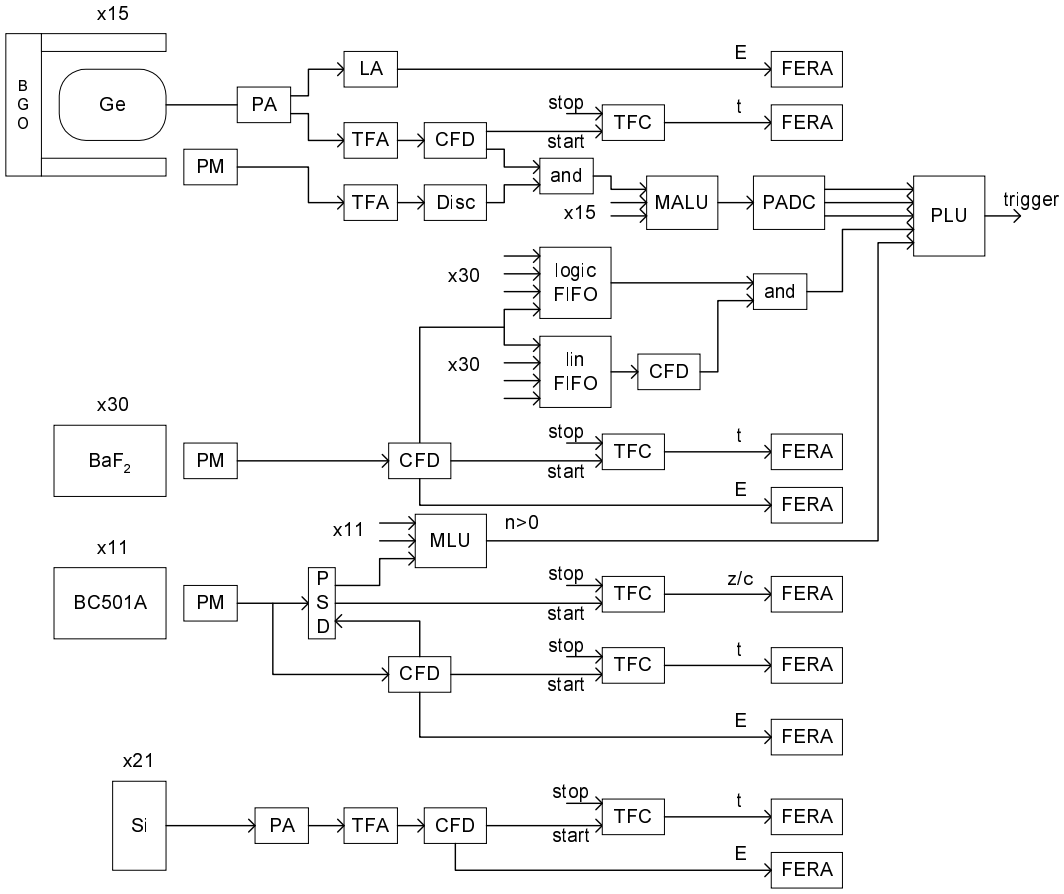

Figure 2.7: Block diagram of the NORDBALL electronic circuit.

Table 2.4: List of experimental parameters recorded on magnetic tape during the NORDBALL experiments.

Experimental Parameters	Number of detectors
Ge energy and time	15
Si ball energy and time	21
Neutron energy, time of flight and zero-cross-over	11
BaF_2 energy and time	30

different detector modules. The logical operations performed on input signals were fully programmable. The trigger conditions used in our NORDBALL experiments are listed in Table 2.5.

The requirement of observing at least one γ-ray in the BaF_2 calorimeter had

to be included in any NORDBALL trigger condition, due to the fact that the BaF_2 detectors provided the time reference signal for all the setup.

Table 2.5: Trigger conditions used in the NORDBALL experiments.

Experiment	Trigger condition
Te experiment	$(2Ge \bigwedge 2BaF_2)$
Pd experiment	$(2Ge \bigwedge 1BaF_2) \bigvee (1Ge \bigwedge 1BaF_2 \bigwedge 1n)$

Signal processing

The energy signals from the Ge detectors were pre-amplified, shaped, amplified and digitized in the 8k analog-to-digital converters (ADC). The energy range of the ADC modules corresponds to a maximum γ-ray energy of about 4 MeV. The readout of the Ge detectors was vetoed by the signals of the BGO Compton-suppression shields. A detailed description of the Ge signal processing is given in Ref. [36]. The energy signals from all the other detectors were amplified and fed into the Fast Encoding and Readout Charge ADC (FERA) modules, and further digitized, with 2k channel resolution.

Time signals from all detectors were digitized using Time-to-FERA Converters (TFC) and FERA modules. Individual signals were used as start signals for TFC, whereas the delayed logical OR signal from all the BaF_2 crystals was used as a common stop. The maximum time window allowed between the start and stop signals was 80 ns. Detailed TFC and FERA timing diagrams can be found in Ref. [37].

2.5 The EUROGAM II array

The EUROGAM II γ-detector array was built by a France-UK collaboration between IN2P3 in France and EPSRC in UK. Figure 2.8 shows a photography of the array. EUROGAM II is described, e.g. in Ref. [38]. Detailed technical documentation can also be found in the Internet at: `http://nnsa.dl.ac.uk/Eurogam/documents/`.

2.5.1 The detector arrangement

The EUROGAM II γ-ray spectrometer consisted of 30 Compton-supressed Ge spectrometers from EUROGAM I and 24 segmented, so-called clover detectors, for a total

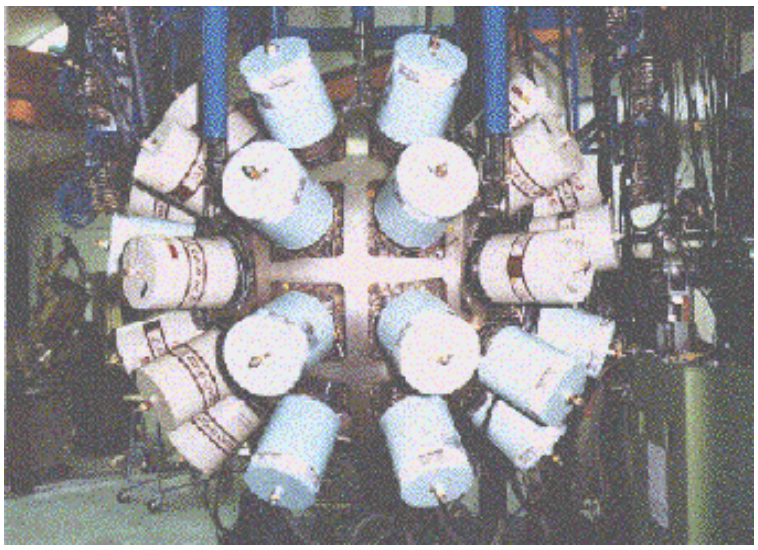

Figure 2.8: The EUROGAM II array.

of 126 Ge detector elements. The large, coaxial Ge detectors were made of hyper-pure n-type crystals ∼70 mm in diameter and ∼75 mm in length. To achieve better packing, the detectors were tapered over their front 3cm at an angle of 5.7°. The coaxial detectors were placed in rings of 5 and 10 detectors at the following angles with respect to the beam direction: 5 detectors at 158°, 10 at 134°, 10 at 46° and 5 at 22°.

The twenty-four clover type detectors were mounted in two rings near 90° with respect to the beam direction. Each clover detector consisted of four coaxial n-type Germanium crystals (Fig. 2.9) packed together in a four-leaf clover arrangement and housed in the same cryostat. The individual Ge detectors had 50 mm in diameter and 70 mm in length. The distance between opposite sides at the front face was 41 mm. Due to the segmentation of the clover detector, the opening angle of each segment is reduced compared to that of the full detector, which has a positive effect by reducing the Doppler broadening of the γ-ray lines in the observed spectra. The four germanium crystals were operated in 'add-back' mode, when the signals corresponding to events, where a γ-ray has been scattered between adjacent crystals were summed together, giving a single signal from the whole clover detector. The forward and backward detectors were 205 mm from the target, and the clover detectors were 230 mm from the target. The total Ge coverage of the solid angle is 40%, giving a total photopeak efficiency of ∼8% for the array.

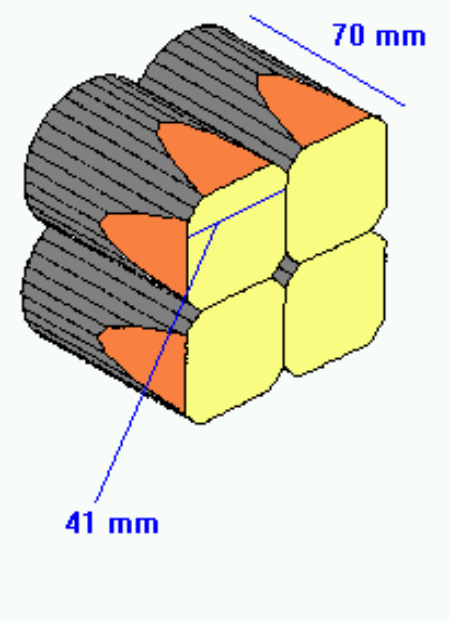

Figure 2.9: Schematic view of the EUROGAM II clover detector.

The EUROGAM II array could also be equipped with ancillary detectors, for example the 54-element Cesium Iodide inner ball particle detector (Diamant), but this device was not used in the experiment discussed here.

2.5.2 Electronics and data acquisition

The EUROGAM II electronics and data acquisition system was based on the VXI (VMEbus eXtensions for Instrumentation) standard. The general architecture of the EUROGAM system is shown in Fig. 2.10 for the sake of completeness.

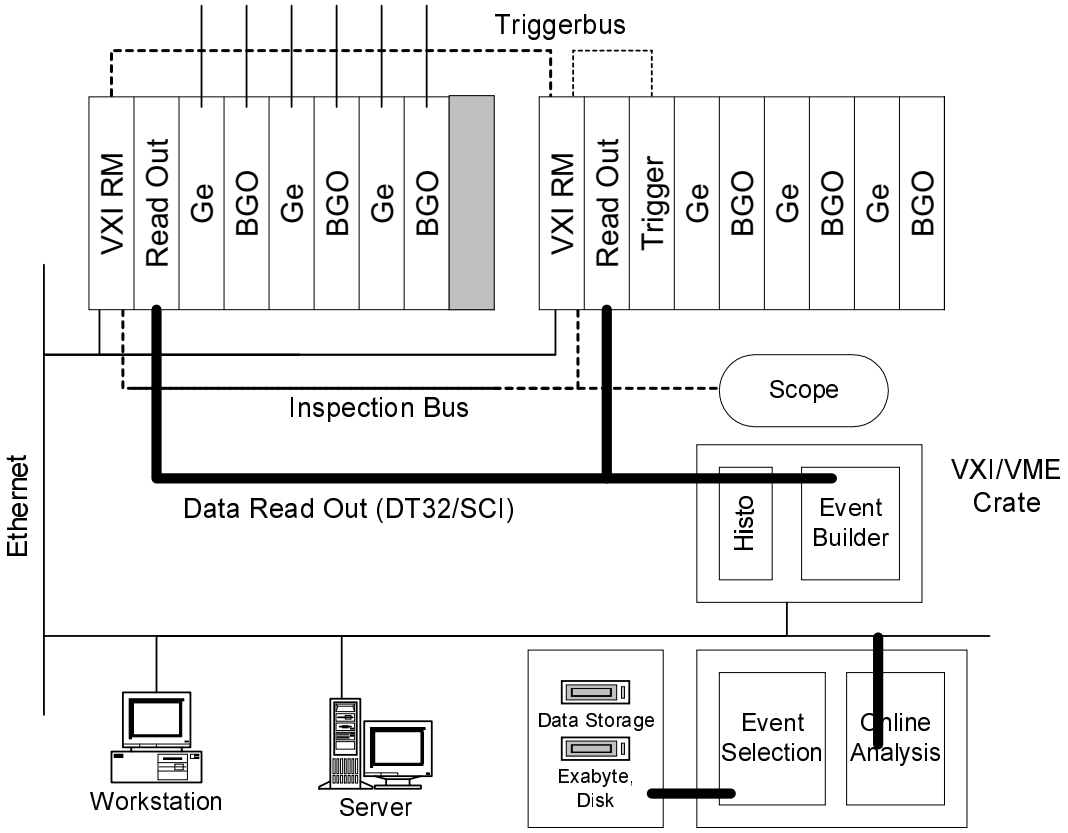

Figure 2.10: The architecture of the EUROGAM electronics and data acquisition system. (taken from Ref. [38].)

The VXI crates hosted the front-end electronics with highly integrated electronic cards for the different detectors. The VME crates were used for the histogrammers, the event builder and the data-storage interface system. Experimental control, real-time monitoring of data quality and event construction were performed using processors within VME. Interfaces for the FERA bus and NIM ADC readout were also available to incorporate data from ancillary detectors. System operation was controlled by a master trigger, that validated the operation of the VXI cards. The master trigger for an event was typically related to the Ge multiplicity (in the Pd experiment coincidence events were stored if at least four suppressed Ge detectors fired), but it could depend on some other signal and, e.g. be validated by the ancillary detectors.

The entire system was connected by an optical-fiber link to workstations in the control room, where all the electronic parameters were set and monitored and where the data were recorded on EXABYTE tapes. All comunications between applications within the data acquisition system were based on the client/server model using remote procedure calls (RPC). A small number of server programs provided access to all the data acquisition resources. These server programs were used to setup and control the parameters of the array elements, e.g. detector specifications and calibrations. Other servers were devoted to on-line data control and analysis, e.g. display and analysis of histograms, and data sorting.

2.6 Data analysis

This section describes different aspects of the data analysis procedures, such as gain matching and sorting, energy and efficiency calibration of the Ge detectors, identification of reaction-channels, analysis of γ-γ and γ-γ-γ coincidences, and γ-γ directional correlations. The description given is based largely on the NORDBALL experiment, although techniques applied only to data from EUROGAM II (e.g. linear polarisation analysis) are also discussed.

The aim of the data analysis procedures was to convert the raw data collected during the experiments into information having physical meaning, which normally ended in a proposed level scheme for the studied nucleus. This usually included: determining the γ-rays energy and relative intensity, identifying the final nucleus, to which they belong, and calculating the energy of the nuclear levels, as well as assigning spin an parity to them. It was also possible to determine other nuclear properties during the analysis of the experimental data, such as half-lives of states, transition probabilities and mixing ratios. Typical physical information that were extracted from the experimental data during the analysis, along with the related techniques are listed in Table 2.6.

Before starting the construction of any level scheme, data needed to be prepared by a series of 'cleaning' procedures, common to most nuclear structure experiments. These procedures involved the calibration of the Ge and ancillary detectors, gain matching of the Ge and ancillary detectors energy and time spectra, and sorting of coincidence data into single γ-ray spectra, γ-γ matrices and γ-γ-γ cubes, according to various 'gating' conditions.

Table 2.6: Physical quantities extracted from experimental data and the related data analysis techniques used in this work. See the text for a more detailed description of the specific methods and techniques.

Physical information	Data analysis technique
γ-ray energy and intensity	single γ-ray spectra
	γ-γ and γ-γ-γ coincidences
reaction channel	γ-ray and particle coincidences
	γ-ray intensity ratio
level energy	γ-γ and γ-γ-γ coincidences
	energy and intensity balance
level spin and parity	angular and directional correlation
	linear polarisation

2.6.1 Preparation of data

Ge energy and efficiency calibration

Energy and efficiency calibrations of the Ge detectors were done using standard radioactive sources ^{56}Co, ^{133}Ba and ^{152}Eu. The calibration data were collected during a few calibration runs and then analysed off-line.

In NORDBALL the energy response of the ADC modules was found to be highly non-linear. For the energy calibration of the Ge detectors the following, empirically chosen function was used

$$E_\gamma(x) = a_0 + a_1 x + a_2 x^2 + a_3 x^3 + a_4 \sqrt{x}, \tag{2.1}$$

where E_γ is the γ-ray energy, x is the channel number and the a parameters are determined from the measurements with sources. In EUROGAM II the Ge energy calibration curve was of a linear character.

In the analysis the efficiency of γ-ray detection as a function of the γ-ray energy was also determined. The relative efficiency curves for the sum of all Ge detectors in NORDBALL and EUROGAM II are shown in Fig. 2.11.

Gain matching

Instabilities in the electronics used to collect and store the experimental data results in shift and gain changes, which have to be corrected for before useful spectra can

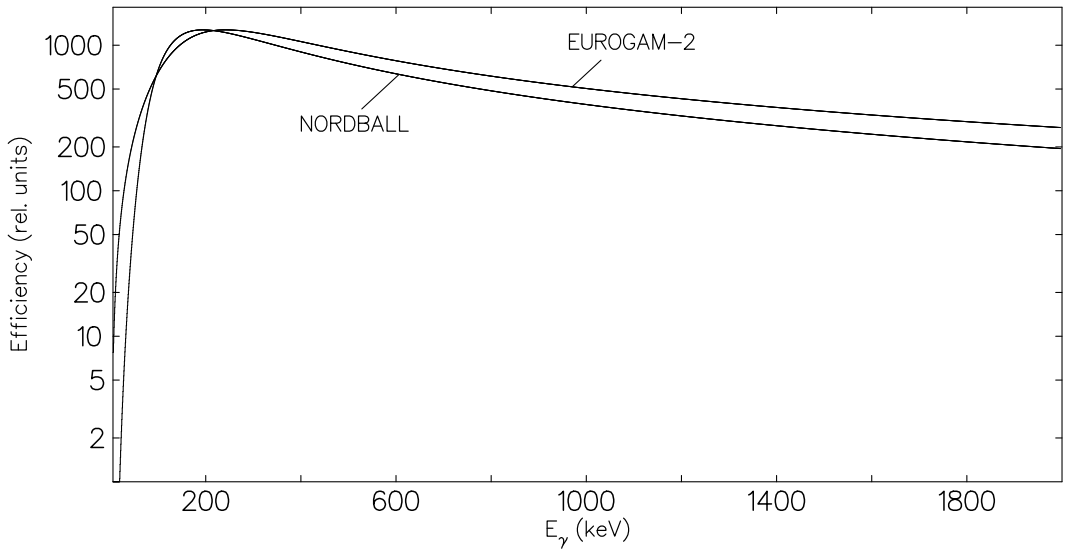

Figure 2.11: The relative efficiency of the Ge detectors in NORDBALL and EUROGAM II arrays. The EUROGAM II array has a larger relative detection efficiency for high energy γ-rays.

be created. The aim of the gain matching procedure was to check the data against these instabilities and to calculate the appropiate correction coefficients, if needed.

NORDBALL procedures

During the NORDBALL data analysis, the gain matching coefficients were calculated for groups of detectors of the same kind using a new, automatic method of shift and gain correction [39]. Various presorting procedures were then applied to the raw data, resulting in a very compact data format, suitable for fast sorting of γ-γ coincidence matrices, and with all possible faulty events being rejected. Each event contained the following information: Ge γ-ray energies, the multiplicity of registered protons, α-particles and neutrons, and flags indicating whether the Ge time signal was considered to be prompt or delayed with respect to a two-dimensional, banana-shaped time gate. Some details of the procedures applied to various types of detectors are given below following Ref. [37].

A high precision gain-matching was done for the energy signals from the Ge detectors. The energy response of the detectors was linearised using a function, consisting of a third-order polynomial and a square root term (see Eq. 2.1). A FWHM of about 3 keV was obtained at a γ-ray energy of 1.3 MeV in the Ge sum spectrum.

Charged particle spectra were gain-matched for Si detectors placed in equivalent

positions with respect to the beam axis (the same ring). The discrimination between protons and α-particles was based on the difference in the energy deposited in the Si detectors. Experimentally, it was done by setting gates or limits in the Si energy spectra. Energy spectra from different Si detectors are shown in Fig. 2.12. For the detectors placed at forward angles the proton peak situated at lower energies is well separated from the broad high-energy bump corresponding to the α particles. At larger detector angles the α bump moves towards the proton peak and almost disappears under the proton peak in the most backward detector.

The neutron energy, time-of-flight (TOF) and zero-cross-over (ZC) signals were gain matched using a linear transformation for the energy signal, whereas a shift correction was used for the time signals. During the off-line analysis, the discrimination between neutrons and γ-rays was significantly improved by using a two-dimensional gate on the ZC time versus TOF plane (see Fig. 2.13) [40, 41]. With the help of this method misassignments of γ-rays for neutrons were reduced to $\sim$0.5%.

EUROGAM II procedures

A presorting procedure was also applied to the raw data from the EUROGAM II experiment, after which gain-matched and compressed data, containing only 'good' events was obtained. During this presort, the Ge energy was also calibrated, and set to a standard value of 0.5 keV/channel for all detectors. For the gain matching and calibration of the Ge detectors a ^{152}Eu source was used.

Sorting of E_γ-E_γ matrices and E_γ-E_γ-E_γ cubes

In the final step of the NORDBALL data preparation, the gain-matched and compressed data were used to create a set of two-dimensional, symmetric E_γ-E_γ particle-gated matrices in the following way: a given γ-γ matrix contained only those γ-γ events that were measured in coincidence with a selected combination of the number of detected neutrons, protons and α-particles. The matrix, sorted by requiring x α-particles, y protons, and z neutrons is shortly referred to as the $x\alpha y\mathrm{p}z\mathrm{n}$-gated matrix or simply the $x\alpha y\mathrm{p}z\mathrm{n}$ matrix. One-dimensional γ-ray energy spectra were also created for each possible combination of the measured neutron and charged-particle multiplicities.

The higher γ-coincidence fold of the data collected during the EUROGAM II experiment, made it possible to construct a E_γ-E_γ-E_γ cube for the analysis of the coincidence data. This cube was sorted by demanding that at least one of the γ-rays

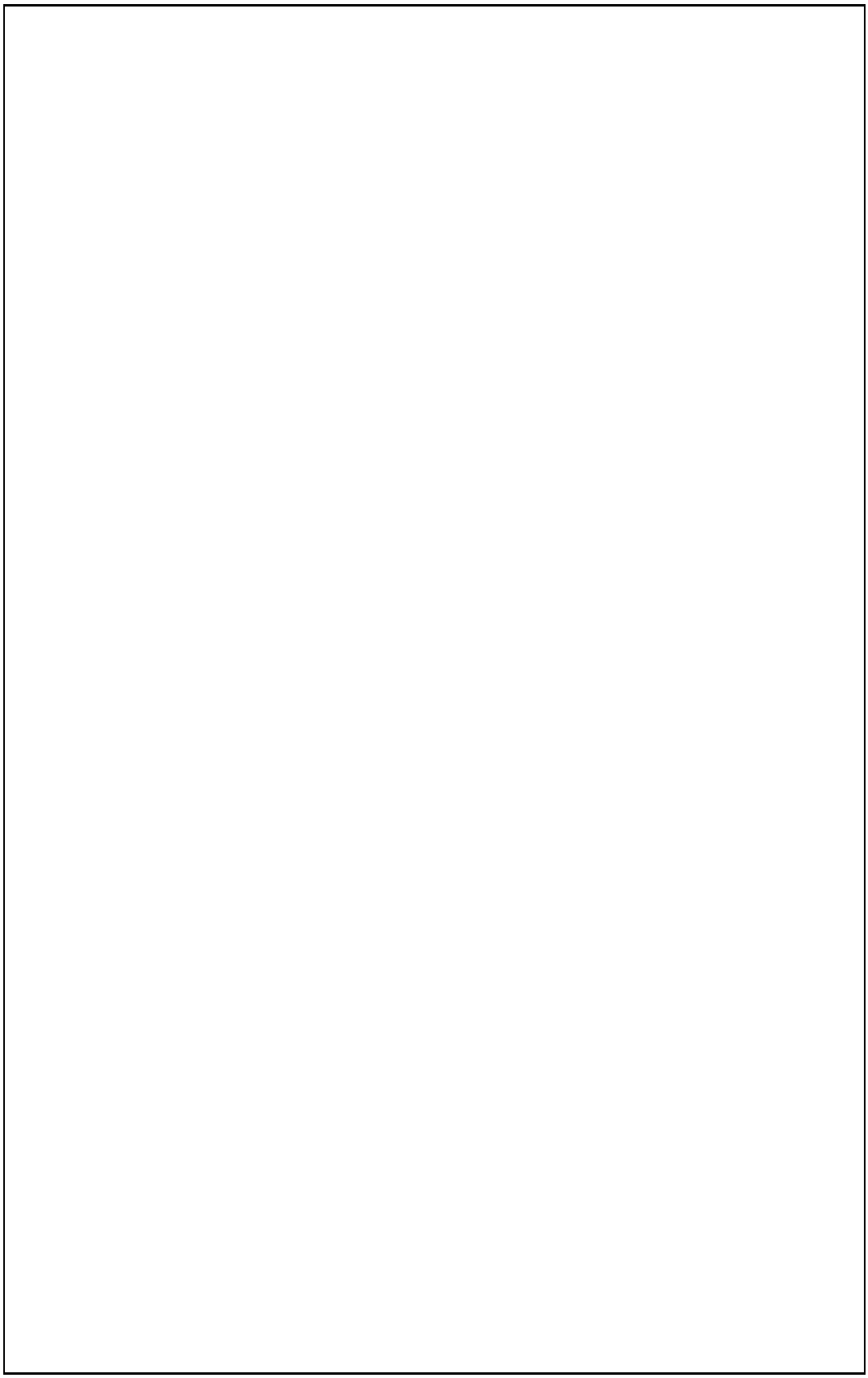

Figure 2.12: Si ball energy spectra for different detector positions (rings).

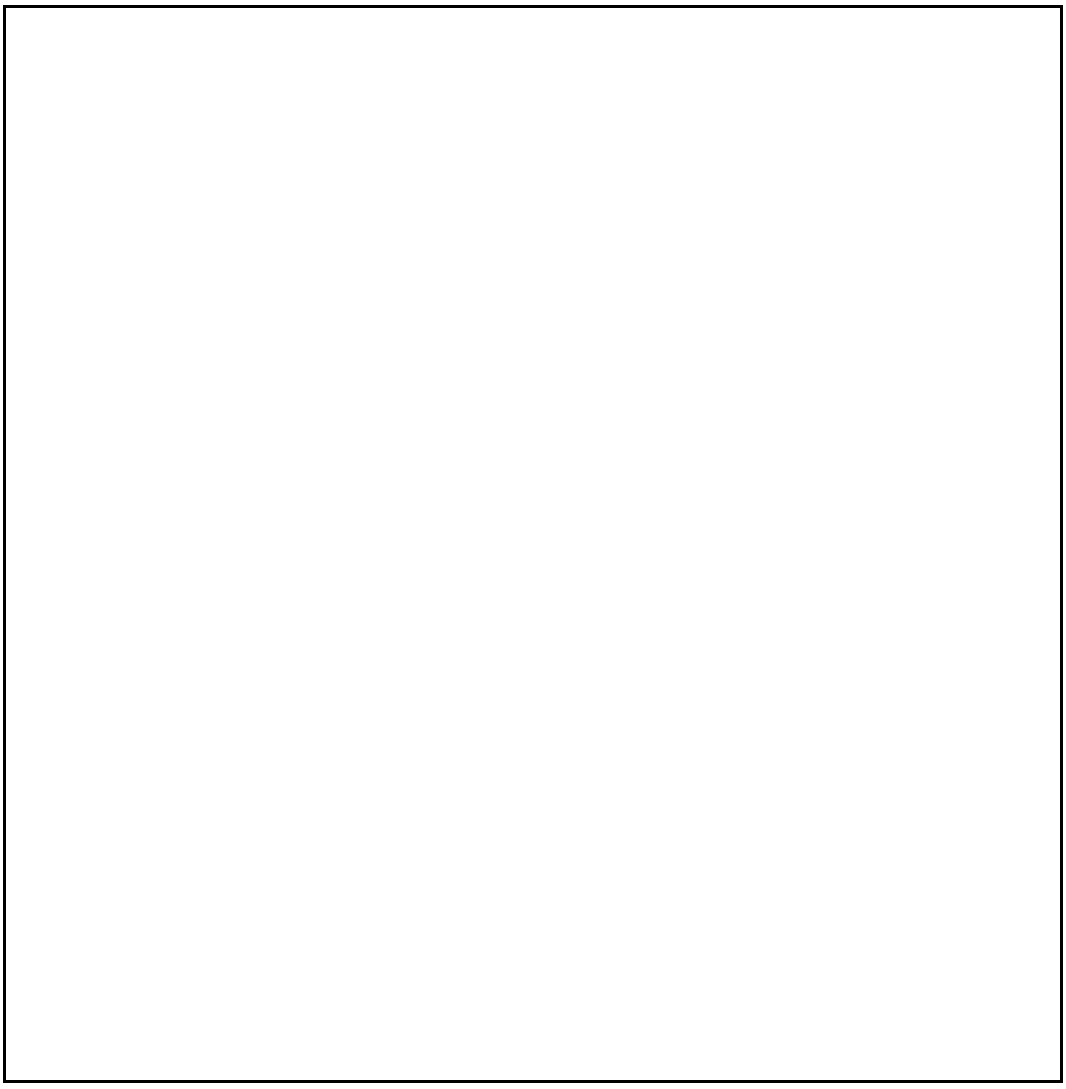

Figure 2.13: Neutron ZC vs. TOF matrix used for off-line neutron-γ separation.

in an event was within a selected set of known strong transitions from the given final nucleus (gated cube).

2.6.2 Construction of the level schemes

Software tools

The construction of the experimental level schemes was performed with the help of the RADWARE software package written by D. C. Radford [42]. The package consisted of two major programs ESCL8R and LEVIT8R for interactive graphical analysis of two-dimensional and three-dimensional coincidence data, respectively.

The main input data to ESCL8R were the symmetrised γ-γ coincidence matrix, and the Ge efficiency and energy calibration curves. The program allowed for fast

and easy inspection of the γ-γ matrix, to set 'gates', i.e. specify an energy window for one of the axes and inspecting the projection onto the remaining axis. The main advantage of the program was that it provided the user not only with the observed coincidence results, but also with expectations, calculated on the basis of the proposed level scheme. The level scheme was displayed on the screen and could be easily modified using the graphical interface to account for the observed discrepances. The optimum energy and intensities for the transitions in the level scheme were extracted by performing least-squares fits to the two-dimensional matrix.

The analysis of triple γ-γ-γ coincidence data was done in a similar manner, with the aid of the program LEVIT8R.

Identification of reaction channels

A major problem when looking for γ-transitions in nuclei for which no excited states are known is the assignment of the γ-ray transitions to a final nucleus. In principle, knowing the number and type of evaporated particles (neutrons, protons, α-particles) emitted from the compound nucleus in coincidence with a γ-ray, one might be able to unambiguously assign that γ-ray to a specific exit channel. However, due to imperfect detection conditions, the efficiency of the particle detection falls below 100%. In addition, several other phenomena make the accurate treatment of neutron and charged-particle detection even more complicated. Among these effects, the following are the most frequent:

- a neutron, a proton or an α-particle is undetected due to imperfect particle detection efficiency,
- two protons, one proton and one α-particle, or two α-particles hitting the same detector element are interpreted as one α-particle,
- a proton is taken as an α-particle, and vice versa due to imperfect proton-α particle discrimination,
- a γ-ray is taken as a neutron due to imperfect neutron-γ ray discrimination,
- one neutron is detected as two, due to multiple scattering of neutrons between the detectors,
- an extra proton or α-particle is 'detected', due to cross-talking between the detectors and/or in the electronics,

- random γ-ray and particle coincidences, uncorrelated events.

All these unwanted effects cause that γ-rays emitted from a certain residual nucleus can be found in spectra corresponding to reaction channels produced by different number of evaporated particles. Nevertheless it is still possible to make unambiguous assignment of γ-rays to a final nucleus.

A method used during the NORDBALL data analysis to assign particle multiplicities to an unknown γ-ray transition was to analyse the intensity distribution of the unknown transition in spectra gated with different combinations of detected particles. It can be shown under certain assumptions that for a given particle type, let's say protons p, the intensity ratio

$$\frac{I_{\gamma\gamma xp}}{I_{\gamma\gamma yp}} \sim M_p$$

in spectra gated with x and y number of detected protons, respectively, is proportional to the number of emitted protons. This ratio can thus be used to distinguish between different proton multiplicities. The same method can be applied to α-particles and neutrons. In practice, the intensity ratio of the unknown transition is compared to the intensity ratio of γ-rays of known particle multiplicity in γ-ray energy gated spectra, and the corresponding particle multiciplities are deduced. An illustration of this method can be found in the discussion of the experimental results of the Te experiment, Chapter 4, Fig. 4.2.

Analysis of γ-γ and γ-γ-γ coincidences

To aid in the construction of the level schemes of the studied nuclei the particle-gated γ-ray spectra and two-dimensional γ-γ matrices sorted from the NORDBALL data, as well as the γ-γ-γ gated cube sorted from the EUROGAM II data, were used. In various cases, since the events of interest were spread over several particle-gated channels, several γ-γ matrices were summed up to increase the available statistics.

The level schemes were built mainly on the basis of the γ-γ coincidence relations, but also the energy and intensity balance was taken into account. The RADWARE spectrum analysis package, described elsewhere in this section, was used to extract the γ-ray energies and intensities from the coincidence data.

Matrix subtraction method

In certain cases during the coincidence analysis, it was necessary to clean the γ-γ matrices from contaminating γ-rays belonging to other residual nuclei, by applying

a matrix subtraction procedure [43]. The method is based on the fact that, due to particle misdetection γ-rays belonging to a nucleus formed with certain number of evaporated particles, can also be found in the γ-ray spectra or γ-γ matrices gated with a lower number of the same type of detected particles. This technique allowed to generate 'clean' matrices by appropriately subtracting from a γ-γ matrix gated with a certain particle multiplicity those gated with a higher particle multiplicity, using experimentally determined subtraction coefficients. The subtraction coefficients were obtained from the intensity ratios of known γ-rays in the contaminating and contaminated matrices.

Below we illustrate the method through an example. We are interested in the nucleus formed by the evaporation of two protons (2p channel). One expects to find most γ-rays belonging to this nucleus in the 2p-gated matrix. However, due to detection problems one will also find γ-rays corresponding to higher (>2p) multiplicity channels in the 2p-gated matrix. To 'clean' this matrix one would proceed as follows (assuming the maximum observed proton multiplicity is 6p): first we subtract the 'normalized' 6p-gated matrix from the 5p-gated one. Then the 'subtracted' 5p matrix is subtracted from the 4p matrix with the corresponding normalisation and so on, up to the 2p-matrix. This method was successfully applied during the analysis of the γ-γ coincidence data from the Te experiment. The results obtained for the ^{110}Te nucleus are shown in Fig. 2.14.

The advantage of this method is that no explicit identification of the contaminating nuclei is needed. It can be done very fast if, instead of the γ-γ matrices, the total projection spectra are used during the subtraction. However, care must be taken when making linear combinations of matrices with low statistics.

Analysis of γ-γ directional correlations

The γ-γ coincidence data collected with the applied detector systems can also be used to investigate directional correlations between the emitted γ-rays [44], and make assumptions on the multipolarity of γ-ray transitions.

In the NORDBALL data analysis a simplified angular correlation method was applied for spin assignments. Two particle-gated $E_{\gamma 1}$-$E_{\gamma 2}$ matrices were created for this purpose. The first $E_{\gamma 1}$-$E_{\gamma 2}$ matrix was sorted for coincidence events in which the γ_1 transition was detected by a Ge detectors in the ring at 143°, and the γ_2 transition was observed at any angle. For the second matrix, γ_1 was required to be detected by a Ge detector in rings at 79° or 101°, since these two angles are geometrically equivalent.

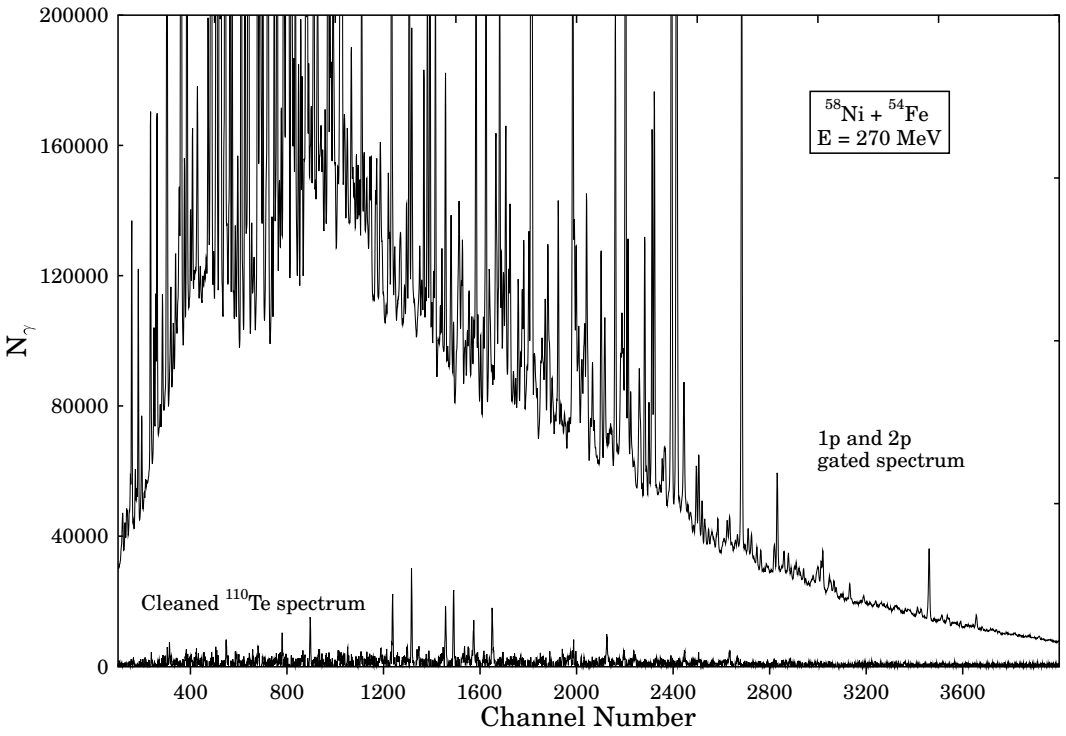

Figure 2.14: Experimental spectrum obtained in the ^{54}Fe(^{28}Ni,2p) reaction channel and the cleaned spectrum for ^{110}Te, after the subtraction. A background supression of ∼3 orders of magnitude was achieved [43].

The experimental information on the γ_1 transition multipolarity can be extracted from the the angular correlation ratio

$$R_{ang} = \frac{I_{\gamma 1}(\theta = 143^\circ)}{I_{\gamma 1}(\theta = 79^\circ, 101^\circ)},$$

where $I_{\gamma 1}(\theta = 143^\circ)$ and $I_{\gamma 1}(\theta = 79^\circ, 101^\circ)$ are the intensities of the γ_1 transition detected at $\theta = 143^\circ$, and $\theta = 79^\circ$ or $\theta = 101^\circ$, respectively. Spectra used to determine the $I_{\gamma 1}$ intensities are gated by the same coincident γ_2 transition, observed at any angle, using the two matrices mentioned above.

According to theoretical estimates for the NORDBALL geometry $R_{ang} \sim 1.5$ corresponded to stretched quadrupole (assuming complete spin alignment of the initial state), ΔI=0 dipole or $\Delta I = 1$ mixed $M1/E2$ transitions, while the R∼0.8 value to stretched dipole or ΔI=0 highly mixed $M1/E2$ transitions [45]. R∼1.2-1.3 values were reasonable for ΔI=0,1 mixed $M1/E2$ transitions, R∼0.4-0.6 corresponded to ΔI=1 mixed $M1/E2$ transitions. These R values were in agreement with the angular distribution ratios obtained for transitions with known multipolarity from different nuclei populated in the present reaction. The dependence of R_{ang} on the gating transition was weak, the variations of its value being smaller that the typi-

cal uncertainty in the determination of R_{ang}, thus it could be neglected [37]. This fact was used to increase statistics by gating on several transitions and summing up projected spectra.

The determination of spin values by this method requires less statistics than a full directional correlation analysis (DCO), but, as shown by the above listed possibilities for R_{ang}, in some cases it may lead to ambiguous results. For instance, it is not possible to ditinguish between a stretched quadrupole and a non-stretched dipole transition. However, in cases, where the same state decays via several branches, it gave the most probable spin assignment. In our analysis we only considered magnetic dipole and electric dipole and quadrupole transitions.

To determine the multipolarities of the transitions using the EUROGAM II data, an analysis of directional correlations from oriented states (DCO) was carried out. For the DCO analysis the coaxial detectors in the ring at 22° and the clover detectors at about 90° were used. A non-symmetric E_γ-E_γ coincidence matrix was created for the above pair of angles, and the DCO ratios:

$$R_{DCO} = \frac{I_{\gamma\gamma}(22°, 90°[gate])}{I_{\gamma\gamma}(90°, 22°[gate])}$$

were extracted for the transitions of interest. The R_{DCO} values were also calculated for such a geometry with help of the GCORR program [47]. According to the formalism of Ref, [46], stretched quadrupoles are characterized by R_{DCO} values of 1.00 and stretched dipoles by values of 0.70, when gated by a stretched $E2$ transition. Pure non-stretched dipoles (ΔI=0) were expected to have R_{DCO} ratios of 1.14.

Linear polarisation analysis

The EUROGAM II segmented clover detectors were used as Compton polarimeters to measure the linear polarisation of the γ-radiation. By combining this information with angular distribution measurements, spin and parity assignments to nuclear states could be determined.

The general principle of the Compton polarimeter is that the probability of Compton scattering of incident γ-radiation through an angle ψ depends upon the angle between the scattering plane containing ψ and the plane perpendicular to the electric vector E of the radiation. The clover detector acting as a Compton polarimeter utilises the Compton scattering between adjacent segments (Fig. 2.15). These events can be separated according to whether the 'line' through the adjacent segments is either parallel to the reaction plane ($N_\parallel$) or perpendicular to it ($N_\perp$).

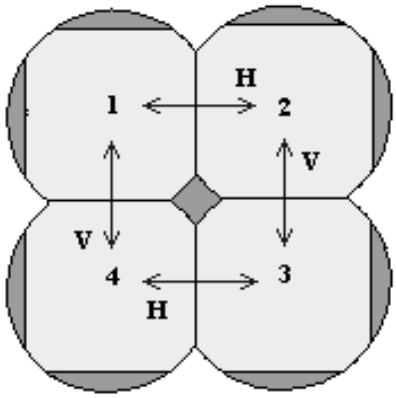

Figure 2.15: Schematics of Compton scattering between the segments of the clover detector.

Assuming that each germanium crystal has equal efficiency, the experimental linear polarization P for the clover detector, is determined by:

$$P = \frac{1}{Q}\frac{N_\perp - N_\parallel}{N_\perp + N_\parallel}, \tag{2.2}$$

where Q is the polarisation sensitivity of the clover detector. The dependence of Q, as a function of the γ-ray energy was taken from Ref. [48].

Two γ-γ matrices were constructed from the coincidence data collecting single hits in any detectors of the clovers on one axis against added-back double-hit scattering events on the other axis. In the first matrix those scattering events are collected, which took place perpendicular to the reaction plane, while in the second matrix those, which took place parallel to the reaction plane. The number of perpendicular ($N_\perp$) and parallel ($N_\parallel$) scatters for a given γ-ray were obtained from spectra gated on the single-hit axis of the respective matrix by transitions in coincidence with the analised γ-ray.

As an example, for pure $\Delta I = 2$ electric quadrupole and $\Delta I = 1$ electric dipole transitions the expected linear polarisation value $P > 0$, whereas for pure $\Delta I = 1$ magnetic dipole transitions this value $P < 0$. For mixed ($M1/E2$) multipolarity transitions the value $P \sim 0$, but may reach higher values as well. More details on the formalism can be found, e.g. in Ref. [49].

Chapter 3

Nuclear models

This chapter is devoted to those nuclear models and their theoretical formalism, which were used to understand the nuclear phenomena taking place behind the experimental results presented in this thesis. Only the basic ideas of each model are presented, along with a compilation of the most important formulae and expressions, but without attempting to go into the details of the mathematical formalism.

The nuclear shell model is one the most important tools aiming at describing the atomic nuclei. It correlates a vast amount of experimental data near magic nuclei such as nuclear binding energies, ground state spins and parities, properties of excited states, static nuclear moments and transition probabilities. The nuclear shell model is best suited to describe nuclei with few valence nucleons outside the close shells. Far from closed shells, however, the numerical treatment of the model becomes cumbersome. In this thesis the structure of ^{108}Te and ^{98}Pd are qualitatively discussed in terms of the quasiparticle shell model.

To describe the collective features of atomic nuclei a number of geometrical and algebraic models have been developed. Among the algebraic models, the interacting boson-fermion model has been particularly succesfull to the description of the structure of odd-A nuclei. This model has been used here to describe high-spin states in the odd ^{109}Te nucleus using the particle-vibration coupling limit.

The geometry based cranking model aims at describing high spin states in nuclei. It combines in the same formalism the description of collective and single-particle configurations, which are the two kinds of structure that are most important in the vicinity of the yrast line at high spin. The cranking approach has been used in this thesis to describe high-spin excitations and band terminating configurations in ^{110}Te and ^{100}Pd.

3.1 The shell model

A detailed discussion of the shell model and its applications can be found in numerous textbooks, such as Ref. [50, 51, 52]. Below we just briefly present the main ideas of the model.

The basic assumption of the shell model is that each nucleon inside the nucleus moves in a potential that represents the average interaction with the other nucleons in the nucleus. The Hamiltonian of such nuclear system of A nucleons is given by:

$$H = \sum_{i=1}^{A} H_i = \sum_{i=1}^{A} \left[T_i + U(r_i) \right], \tag{3.1}$$

where T_i denotes the kinetic energy operator of the i-th nucleon and $U(r)$ is usually a spherically symmetric potential. The single-particle wave functions are the solutions of the single-particle Schrödinger equation

$$\left[T_i + U(r_i) \right] \phi_{\alpha_i}(\vec{r_i}) = e_{\alpha_i} \phi_{\alpha_i}(\vec{r_i}), \tag{3.2}$$

where α_i stands for the quantum numbers of the state occupied by the i-th nucleon and e_{α_i} its single-particle energy.

One of the commonly used potentials (besides the isotropic harmonic-oscillator potential, Fig. 3.1a) is the Woods-Saxon potential

$$U(r) = \frac{U_o}{1 + \exp^{\frac{r - R_o}{a}}}. \tag{3.3}$$

where U_o denotes the depth of the potential well, R_o stands for the radius of the nucleus and a is the diffuseness of the nuclear surface. Typical values of the parameters are: $U_o = -50$ MeV, $R_o = r_o A^{-1/3}$, with $r_o = 1.2$ fm and $a = 0.7$ fm. The single-particle energies obtained for the Woods-Saxon potential are shown in Fig. 3.1b. Energy levels separated by a larger gap form a major shell. However, the number of nucleons at the major shell closures do not agree with the experimentally observed magic numbers: 2, 8, 20, 28, 50, 82 and 126. This problem was overcome by Mayer [53], and Haxel, Jensen and Suess [54], who added a strong spin-orbit term to the nuclear Hamiltonian of the form

$$U_{so} = f(r) \vec{l} \cdot \vec{s}, \tag{3.4}$$

where $f(r)$ is a function related to the potential $U(r)$, s is the nucleon spin and l is the orbital angular momentum. Their sum gives the nucleon total angular momentum $\vec{j} = \vec{l} + \vec{s}$. The spin-orbit term modifies the energy of the orbitals by

Figure 3.1: Single-particle levels in the shell model: a) harmonic-oscillator potential, b) Woods-Saxon potential, c) inclusion of the spin-orbit term, d) number of nucleons in each orbital, e) its symbols and f) parity, g) number of nucleons at shell closures. (Figure is taken from Ref. [51].)

$$< \phi_{lj}|U_{so}(r)|\phi_{lj} >= \begin{cases} -\frac{1}{2}(l+1) < f(r) >_l, & j = l - \frac{1}{2}, \\ \frac{1}{2}l < f(r) >_l, & j = l + \frac{1}{2} \end{cases} \tag{3.5}$$

It was empirically found that $< f(r) >_l \approx -20 \cdot A^{-2/3}$ MeV , implying that the $j = l + \frac{1}{2}$ level is lowered in energy with respect to the $j = l - \frac{1}{2}$ orbital (Fig. 3.1c). The magic numbers of nucleons, corresponding to the completely filled shells are shown in Fig. 3.1g. They agree very well with the experiment. However, the ordering of the levels within the major shells might change with the mass of the nucleus. The

ordering will also differ between neutrons and protons, especially in heavy nuclei, due to the Coulomb interaction.

3.2 The interacting boson-fermion model

The IBFM is a generalisation of the Interacting Boson Model (IBM) of Arima and Iachello [55] to odd-A nuclei, where an additional single-particle degree of freedom (a fermion with angular momentum j) is introduced and coupled to the system of s (L=0) and d (L=2) bosons, describing the even-even core. A boson is regarded as a collective superposition of two fermion states, with the restriction that only the valence nucleons can contribute to the creation of the boson. Thus, the number of bosons in the core is equal to the number of particle pairs outside the closed shell. In our IBFM description, it is required that the number of bosons and fermions are both separately conserved. A detailed description of the model can be found, e.g. in Ref. [56].

The Hamiltonian

The Hamiltonian of the IBFM is taken as [57]:

$$H = H_B + H_F + V_{BF}, \tag{3.6}$$

where

$$\begin{aligned} H_B = {} & \epsilon_s \hat{n}_s + \epsilon_d \hat{n}_d + \sum_{L=0,2,4} \frac{1}{2}\sqrt{2L+1}\; c_L \left[(d^+ \times d^+)^{(L)} \times (\tilde{d} \times \tilde{d})^{(L)} \right]^{(0)} \\ & + \frac{1}{\sqrt{2}}\; \tilde{v}_2 \left[(d^+ \times d^+)^{(2)} \times (\tilde{d} \times \tilde{s})^{(2)} + h.c. \right]^{(0)} \\ & + \frac{1}{2}\; \tilde{v}_0 \left[(d^+ \times d^+)^{(0)} \times (\tilde{s} \times \tilde{s})^{(0)} + h.c. \right]^{(0)} \\ & + u_2 \left[(d^+ \times s^+)^{(2)} \times (\tilde{d} \times \tilde{s})^{(2)} \right]^{(0)} \\ & + \frac{1}{2}\; u_0 \left[(s^+ \times s^+)^{(0)} \times (\tilde{s} \times \tilde{s})^{(0)} \right]^{(0)} \end{aligned} \tag{3.7}$$

is the Hamiltonian of the boson core [55] and

$$H_F = \sum_{j,m}\; \tilde{\epsilon}_j\; (c^+_{jm} \tilde{c}_{jm}), \tag{3.8}$$

is the quasiparticle Hamiltonian of the odd nucleon.

The V_{BF} term contains the boson-fermion interaction, consisting of an effective monopole and quadrupole interaction, and an exchange force [57]:

$$\begin{aligned} V_{BF} = & \sum_{j} A_j \left[(d^+ \times \tilde{d})^{(0)} \times (c_j^+ \times \tilde{c}_j)^{(0)} \right]^{(0)} \\ & + \sum_{jj'} \Gamma_{jj'} \left[Q_B^{(2)} \times (c_j^+ \times \tilde{c}_{j'})^{(2)} \right]^{(0)} \\ & + \sum_{jj'j''} \Lambda_{jj'}^{j''} : \left[(c_j^+ \times \tilde{d})^{(j'')} \times (d^+ \times \tilde{c}_{j'})^{(j'')} \right]^{(0)} : \end{aligned} \tag{3.9}$$

with

$$Q_B^{(2)} = (s^+ \times \tilde{d} + d^+ \times \tilde{s})^{(2)} + \chi (d^+ \times \tilde{d})^{(2)} \tag{3.10}$$

In Eqs. (3.7-3.10), $\hat{n}_s = (s^+ \tilde{s})$ and $\hat{n}_d = (d^+ \tilde{d})$ are the s and d boson number operators, $(s^+, \tilde{s})$ and $(d^+, \tilde{d})$ are the s and d bosons creation and anihilation operators, $(c_j^+, \tilde{c}_j)$ are the quasiparticle creation and anihilation operators, and the symbol (:) denotes normal product.

The coefficients A_j, $\Gamma_{jj'}$ and $\Lambda_{jj'}^{j''}$ depend on the labels j, j', j'' of the single-particle orbits which can be occupied by the odd fermion. The j-dependence of the coefficients was estimated with the expressions:

$$\begin{aligned} A_j &= A_0 \sqrt{5} \sqrt{2j+1}, \\ \Gamma_{jj'} &= \Gamma_0 \sqrt{5} \, (u_j u_{j'} - v_j v_{j'}) < j \parallel Y_2 \parallel j' >, \\ \Lambda_{jj'}^{j''} &= -2\Lambda_0 \frac{\sqrt{5}}{\sqrt{2j''+1}} \, (u_j v_{j''} + v_j u_{j''})(u_{j''} v_{j'} + v_{j''} u_{j'}) \cdot \\ &\quad \cdot < j'' \parallel Y_2 \parallel j >< j'' \parallel Y_2 \parallel j' > . \end{aligned} \tag{3.11}$$

where v_j^2 is the occupation probability of the j orbit and $u_j^2 = 1 - v_j^2$.

Limiting cases

The treatment of the odd nuclei in the framework of the interacting boson fermion model is particularly interesting when the Hamiltonian of the boson core, H_B, has one of its three dynamical symmetries, SU(5), SU(3) and SO(6). In those cases the IBFM leads to results very similar to those obtained in the following special cases:

3.3 The cranked shell model

The main constituents of the model are outlined below.

Table 3.1: Limiting cases in the IBFM.

	H_B symmetry	Limiting case
I.	SU(5)	Particle plus vibration model
II.	SU(3)	Particle plus rotor model
III.	SO(6)	Particle plus γ-unstable rotor

The single-particle potential

In our cranked calculations it is assumed that the nuclear mean-field is described by the deformed Woods-Saxon potential, and the same set of 'universal' parameters is used for a set of nuclei [58]. The nuclear surface is described by a non-axially symmetric shape with coefficients up to α_{4k} and even multipoles. In the multipole expansion of the nuclear radius R, the coefficients α_{ik} are transformed into the usual β_2, β_4 and γ degrees of freedom in the following way:

$$\begin{aligned}
\alpha_{20} &= \beta_2 \cos\gamma, \\
\alpha_{22} &= -\sqrt{\frac{1}{2}}\beta_2 \sin\gamma = \alpha_{2-2}, \\
\alpha_{40} &= \frac{1}{6}\beta_4(5\cos^2\gamma + 1), \\
\alpha_{42} &= -\frac{1}{12}\beta_4\sqrt{30}\sin 2\gamma = \alpha_{4-2}, \\
\alpha_{44} &= \frac{1}{12}\beta_4\sqrt{70}\sin^2\gamma = \alpha_{4-4}.
\end{aligned} \tag{3.12}$$

The central part of the potential is defined as

$$V(r,\hat{\beta}) = \frac{V_o}{1+e^{\frac{r-R}{a}}}, \quad V_o = -V_{oo}\left[1 \pm \kappa\frac{N-Z}{N+Z}\right] \tag{3.13}$$

where V_{oo}=49.6 MeV, κ=0.86 (the plus sign refers to protons and the minus sign to neutrons) and a=0.7 fm are the universal parameters. The general deformation parameter $\hat{\beta}$ stands for the β_2, β_4 and γ parameters defining the nuclear shape.
The spin-orbit potential has the form

$$V_{so}(r,\hat{\beta}) = \lambda\left(\frac{\hbar}{2Mc}\right)^2\left[\nabla V'(r,\hat{\beta})\times\vec{p}\right]\cdot\sigma \tag{3.14}$$

where the spin-orbit strength λ_p=λ_n=36.0 MeV, $\vec{p}$ is the linear momentum operator and σ are the Pauli spin matrices.
The Coulomb term for protons has the form $\frac{1}{2}(1+\tau_3)V_c$, and is determined by a charge $(Z-1)e$ distributed uniformly inside the nuclear surface.

The parameter $R_o = r_o A^{\frac{1}{3}}$ of the shape parametrisation is different for protons and neutrons and for the central and spin-orbit part of the potential:

$$\begin{aligned} r_{o,n} &= 1.347 \text{ fm}, \quad r^{so}_{o,n} = 1.32 \text{ fm} \\ r_{o,p} &= 1.275 \text{ fm}, \quad r^{so}_{o,p} = 1.32 \text{ fm} \end{aligned} \tag{3.15}$$

The cranking Hamiltonian

The basic idea of the cranking model is to use a body-fixed coordinate system with respect to the nuclear potential and to force it to rotate, or in other words to "crank" it [59].

The Hamiltonian of the system in the body-fixed coordinates, rotating around the x-axis with a fixed frequency ω (the *cranking* Hamiltonian) has the form

$$H^{\omega} = H_0 - \hbar\omega I_x, \tag{3.16}$$

where I_x is the angular momentum projection onto the x-axis, and H_0 is the quasi-particle Hamiltonian in the laboratory system at ω=0.

The energy of the single-particle state i in the rotating frame is called the Routhian and is given by the expression

$$e^{\omega}_i = e_i - \omega i_x, \tag{3.17}$$

where e_i is the single-particle energy in the laboratory system and i_x is the contribution of the state i to the total spin projection I_x.

Pairing correlations are taken into account by adding a two-body operator H_{pair} to the Hamiltonian, with a strength G:

$$H_{pair} = -G \sum_{i,i'>0} (a^+_i a^+_{\bar{i}} a_{i'} a_{\bar{i}'}), \tag{3.18}$$

where a^+_i are the fermion creation operators acting on state i (and its time reversal state $\bar{i}$).

Total Routhian Surfaces

The total Routhian of a nucleus rotating at a frequency ω as a function of deformation $\hat{\beta}$ is obtained as the sum of the macroscopic liquid drop energy, the Strutinsky shell correction energy [60], and the pairing energy:

$$E^{\omega}(\hat{\beta}) = E^{\omega}_{macro}(\hat{\beta}) + \delta E^{\omega}_{shell}(\hat{\beta}) + \delta E^{\omega}_{pair}(\hat{\beta}). \tag{3.19}$$

Eq. (3.19) can be rewritten in the following way:

$$E^{\omega}(\hat{\beta}) = E^{\omega=0}(\hat{\beta}) + \left[< \Psi^{\omega} \mid \hat{H}^{\omega}(\hat{\beta} \mid \Psi^{\omega} > - < H^{\omega=0}(\hat{\beta}) >_{BCS} \right]. \tag{3.20}$$

In Eq. (3.20), $E^{\omega=0}(\hat{\beta})$ represents the total energy at zero frequency, while the term in brackets corresponds to the energy gain due to rotation.
In the calculations, the total Routhian is minimised with respect to the quadrupole shape parameters β_2 and γ, which are transformed into cartesian coordinates $X = \beta_2 \cos(\gamma + 30°)$ and $Y = \beta_2 \sin(\gamma + 30°)$. The minimisation procedure is then performed for different values of the hexadecupole deformation parameter β_4. In this thesis the unified code for calculations of Total Routhian Surfaces (TRS), developed by Nazarewicz *et al* was used.

Experimental Routhians and alignment

In this part expressions will be provided for various experimental quantities, which are often used to compare experimental results with the cranked Woods-Saxon calculations.

For a transition from an initial state of energy and angular momentum, E_i and I_i, to a final state of E_f and I_f, the total Routhian E^{ω} in the rotating system is constructed from experimental quantities as

$$E^{\omega}(I_a) = \frac{E_i - E_f}{2} - \hbar\omega(I_a) \cdot I_x(I_a), \tag{3.21}$$

where I_a is the average of I_i and I_f. The quantity I_x is the projection of the total angular momentum onto the rotational axis, defined as function of the measured angular momentum I and its projection on the nuclear symmetry axis, K,

$$I_x(I) = \sqrt{(I + 1/2)^2 - K^2}. \tag{3.22}$$

The experimental frequencies (defined through the relation $\frac{dE}{dI} = \hbar\omega$) can also be calculated for each transition as

$$\hbar\omega(I_a) = \frac{E_i - E_f}{I_x(I_i) - I_x(I_f)}. \tag{3.23}$$

The total Routhian E^{ω} and the spin projection I_x are built up of both collective and single-particle contributions. The single particle alignment i and excitation

energy e' in the rotating frame are calculated with the help of the Harris formula for the moments of inertia of the ground-state band:

$$J = J_o + \omega^2 J_1. \tag{3.24}$$

A reference energy E'_g and spin projection I_{xg} are then constructed:

$$E'_g(\omega) = -\frac{\omega^2}{2} J_o - \frac{\omega^4}{4} J_1 + \frac{1}{8 J_o}, \tag{3.25}$$

$$I_{xg}(\omega) = \omega J_o + \omega^3 J_1. \tag{3.26}$$

The rotating-frame excitation energy e', associated with the excited quasiparticles, and their aligned angular momentum i are thus given by

$$e'(\omega) = E^{\omega} - E'_g(\omega), \tag{3.27}$$

$$i(\omega) = I_x(\omega) - I_{xg}(\omega). \tag{3.28}$$

Terminating states

A terminating (aligned) state represents the end of a collective (rotational) band, when the highest possible angular momentum for a specific configuration is reached. For valence particles in a j-shell, it is trivial to calculate the maximal spin, I_{max}; one particle will contribute with $j\hbar$, the next with j-1 due to the Pauli principle, and so on.

In the cranking model single particle excitations are described on the same footing that collective behaviour. By chosing the cranking axis.as the symmetry axis one can actually calculate the energy, i.e. the frequency neccesary to make particle-hole excitations. Each crossing in the quasiparticle diagrams will then correspond to the neccesary amount of energy (frequency) needed to make a new quasiparticle excitation. This way favored states can be calculated and one can obtain the crossing point of non-collectiv excitations versus collective ones.

Chapter 4

Spectroscopy of ^{108,109,110}Te nuclei

4.1 Earlier studies

The heavier Tellurium isotopes are spectroscopically well known, but for the neutron deficient isotopes the experimental data were very scarce prior to our work.

The low-spin structure of the ground-state band in ^{114}Te and ^{116}Te up to spin 10^+ and 8^+, respectively, was established in Ref. [61]. Their level schemes have been later extended to higher spins (see e.g., Refs. [62, 63, 64]). The most recent spectroscopic information on the ^{114,116}Te nuclei come from Refs. [65, 66], where rotational bands up to $I^\pi=40^+$ were observed in a heavy-ion γ-spectroscopy experiment. Their structure has been interpreted in terms of 'intruder' bands built on proton particle-hole excitations across the Z=50 shell gap. Evidence for rotational behaviour at high spin has also been recently observed in ^{112}Te [67], where the yrast states has been populated up to $I^\pi=22^+$, following heavy-ion reactions.

In contrast, none of the ^{108,109,110}Te nuclei had been studied in-beam before this work. Only half-lives of the ground states were previously known [68, 69, 70]. These data were obtained mainly from α-decay studies [71, 72] and from β-delayed proton and α-particle radioactivity work [73]. The proton radioctivity of ^{108}Te using a more precise, electrostatic separation method was also studied in Ref. [74]. In the case of the ^{110}Te isotope, the energy of its first excited state had been determined from the α-decay of ^{114}Xe by Tidemand-Petersson *et al* [73].

Thus, the aim of our work was to get information on the excited states of ^{108,109,110}Te using in-beam spectroscopic methods, and to investigate whether their structure follow the systematics of heavier Te isotopes, or there is any structural changes when approaching the proton drip-line.

4.2 Experimental results

In this section new experimental results obtained in this work for ^{108,109,110}Te nuclei are presented. The detailed description of the experiment is given in Section 2.3.1 of this thesis.

4.2.1 The ^{108}Te nucleus

Excited states of ^{108}Te were attained for the first time in our experiment. The ^{108}Te nuclei were produced by the evaporation of 2 protons and 2 neutrons, or 1 α-particle, from the compound nucleus ^{112}Xe. In the 1α-gated matrix only the strongest 664 keV γ-ray, assigned to ^{108}Te, was seen. Based on that, the relative intensity of this channel was estimated to be less than 1% of that of the 2p2n channel. The 2p2n channel itself represented a weak reaction channel with $\sim$0.1% contribution to the total yield (see Fig. 2.2). In addition, the detection efficiency for two neutrons was only $\sim$5%. As a result, the decay of only a few hundred ^{108}Te nuclei was detected. The strongest contamination came from the 1n channels, due to double detection of neutrons scattered from one detector to another.

In order to select and enhance γ-rays belonging to ^{108}Te the matrix subtraction method described in Section 2.6.2 was applied. The projected spectrum of the matrix cleaned for ^{108}Te is shown in Fig. 4.1.

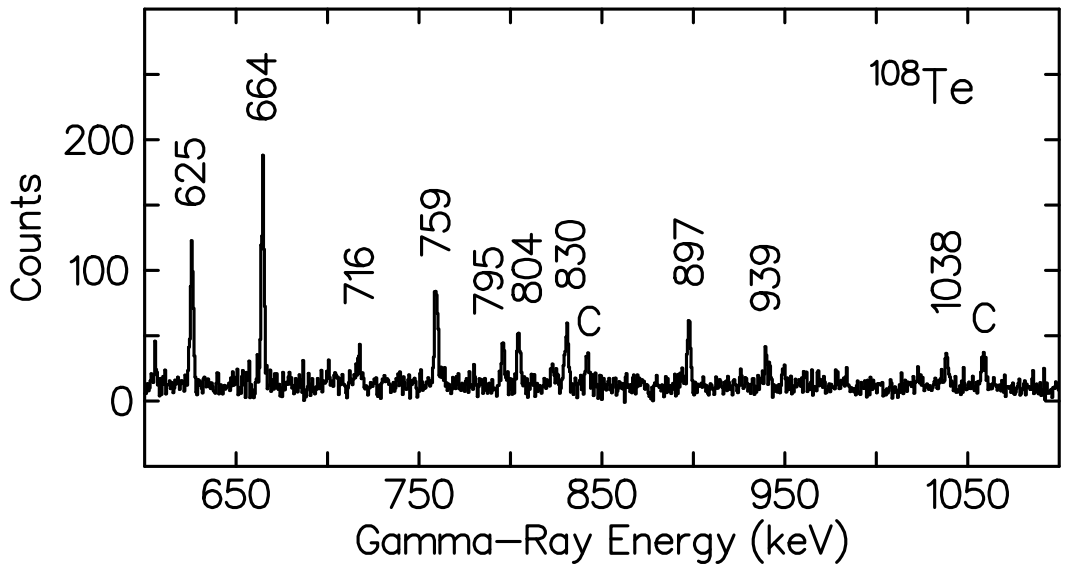

Figure 4.1: Total projection spectrum of ^{108}Te obtained from the cleaned 2p2n-gated matrix. Transitions labelled by C are known contaminants.

To confirm the assignment of γ-rays seen in Fig. 4.1 to the ^{108}Te nucleus we

measured the intensity ratios of these γ-rays in the projection spectra of the uncleaned matrices, gated with different numbers of detected neutrons and protons, and compared them with the average values obtained for γ-ray transitions of known nuclei (see Section 2.6.2 for an explanation of the method). The intensity ratios of the three strongest γ-rays, the 625, 664 and 759 keV lines are shown in Fig. 4.2.

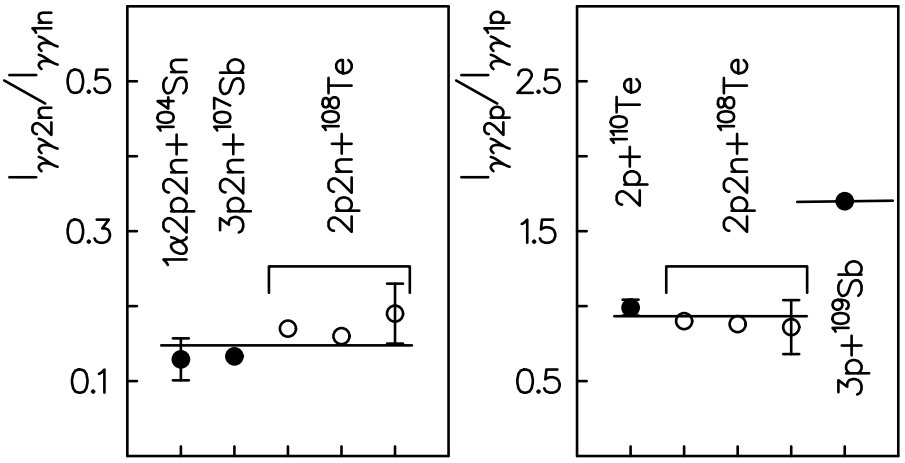

Figure 4.2: Assignment of γ-rays to the 2p2n+^{108}Te reaction channel (open circles) based on the comparison of their intensity ratios for different neutron and proton multiplicity with those of known γ-ray lines (filled circles).

From the obtained $I_{\gamma\gamma 2n}/I_{\gamma\gamma 1n}$ and $I_{\gamma\gamma 2p}/I_{\gamma\gamma 1p}$ ratios we determined the number of emitted neutrons and protons to be equal to 2 in both cases. Because no α-particles were seen in coincidence with the three strongest transitions, except from the very weak contribution mentioned above, one could unambiguously assign the transitions to the 2p2n+^{108}Te reaction channel. All other γ-rays shown in Fig. 4.1 were in coincidence with these three transitions, and therefore were also assigned to the ^{108}Te nucleus. Energies, relative intensities and proposed multipolarites for γ-rays assigned to ^{108}Te are listed in Table 4.1.

The sum of the 2p2n- and 2p1n-gated E_γ-E_γ matrices cleaned for ^{108}Te, was used to analyse the coincidence data. Besides the coincidence relations, the intensity balance deduced from γ-ray intensities in the total projection spectrum and in the gated spectra were considered. The level scheme of the ^{108}Te nucleus deduced in this work is shown in Fig.4.3.

First of all, the analysis showed that the strongest line in the projection spectrum (664 keV) is a doublet. Furthermore, the three strongest γ-rays of 625, 664 and 759 keV, having equal intensities within their uncertainties, were in coincidence with each other, and with all the other transitions labelled in Fig. 4.1. Their ordering

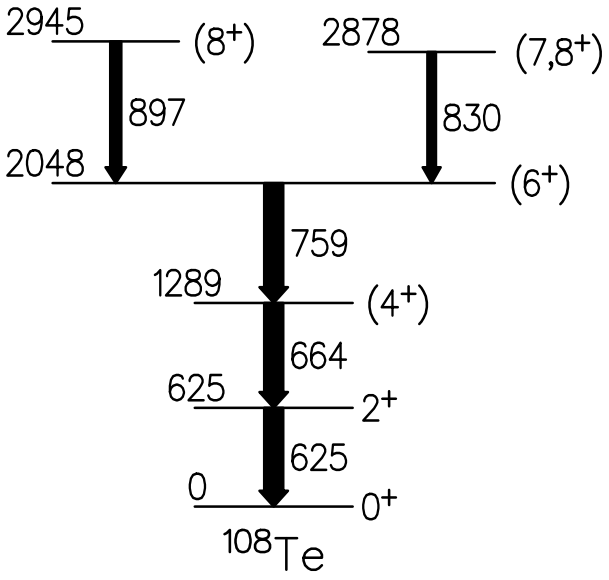

Figure 4.3: The experimental level scheme of ^{108}Te obtained in our work. Only those transitions are shown in the level scheme the placement of which could be firmly establish from the coincidence analysis.

was determined from the intensities in the spectra gated by higher lying transitions, which is in agreement with the systematics of higher Te isotopes (see e.g., Fig. 4.11). The 897 and 830 keV γ-rays were in coincidence with the three strongest ones, but not with each other, so they formed parallel branches. Their placement feeding the 2048 keV was supported by the fact that the sum of their intensities accounted for the intensity of the 759 keV line. From the gated spectra obtained for the rest of the observed γ-rays only their coincidence relations with the three strongest transitions could be established due to the very low statistics.

For spin assignments the angular correlation ratios $R_{ang} = I_\gamma(143°)/I_\gamma(79°, 101°)$ were extracted. The R_{ang} values for the 625 keV and 759 keV transitions (see Table 4.1), suggested that they are stretched E2 transitions. For the remaining three transitions placed in the level scheme the uncertainties in the R_{ang} ratios were too large to unambiguously determine their multipolarity. Thus, the 2^+ value for the 625 keV state is well established, but the (4^+) and (6^+) values were only tentatively assigned.

Very recently, after the work presented in this thesis was published, new and higher quality data for ^{108}Te have been obtained in Ref. [76, 77] using the newest generation of detector arrays EUROBALL and GAMMASPHERE, respectively. Their findings have confirmed most of the results presented in this work obtained with our

Table 4.1: Energies, relative intensities, angular correlation ratios R_{ang} and proposed multipolarities of γ-rays assigned to ^{108}Te.

E_γ [1] (keV)	I_γ (rel.)	R_{ang}	$I_i^\pi \rightarrow I_f^\pi$
625.1	100	1.62(28)	$2^+ \rightarrow 0^+$
664.1[2]	100		$(4^+) \rightarrow 2^+$
716.2	27(5)		
758.8	100	1.98(60)	$(6^+) \rightarrow (4^+)$
795.5	38(3)		
804.0	38(3)		
830.2	45(3)		$(7, 8^+) \rightarrow (6^+)$
897.1	58(2)		$(8^+) \rightarrow (6^+)$
938.9	49(3)		
1038.4	41(3)		

[1] Errors ranged between 0.1-0.5 keV.

[2] Doublet

limited statistics. In Ref. [77] a negative-parity band connected by $E1$ transitions to the ground-state band has also been measured.

4.2.2 The ^{109}Te nucleus

The nucleus ^{109}Te was identified for the first time in-beam in our experiment. The ^{109}Te nuclei were produced following the evaporation of two protons and one neutron from the compound nucleus ^{112}Xe. The γ-rays assigned to ^{109}Te appeared, however, not only in the 2p1n-gated γ-γ matrix, but also in the 1p- and 2p-, and in the 1n-, 1p1n- and 2p1n-gated γ-γ matrices. The number of ^{109}Te γ rays collected into the 1p- and 2p-gated matrices was about a factor of 3 larger than in the 1n-gated matrices. However, the spectra obtained from these matrices were of lower quality, because the high background originating from γ-rays of nuclei produced without the emission of neutrons obscured the weak transitions of ^{109}Te. Thus in the data analysis the sum of the 1n-, 1p1n- and 2p1n-gated matrices were used. The contaminating γ-ray lines of the other nuclei present in this matrices due to undetected protons, neutrons or α-particles from reaction channels with higher particle multiplicities were eliminated by using the matrix subtraction technique. Finally, some small corrections were made to remove contaminating transitions present because of misidentifying α-particles

as protons, and arising from target and projectile excitations. The total projection spectrum of the cleaned γ-γ matrix obtained this way is shown in Fig. 4.4, where all labelled γ-rays belong to ^{109}Te.

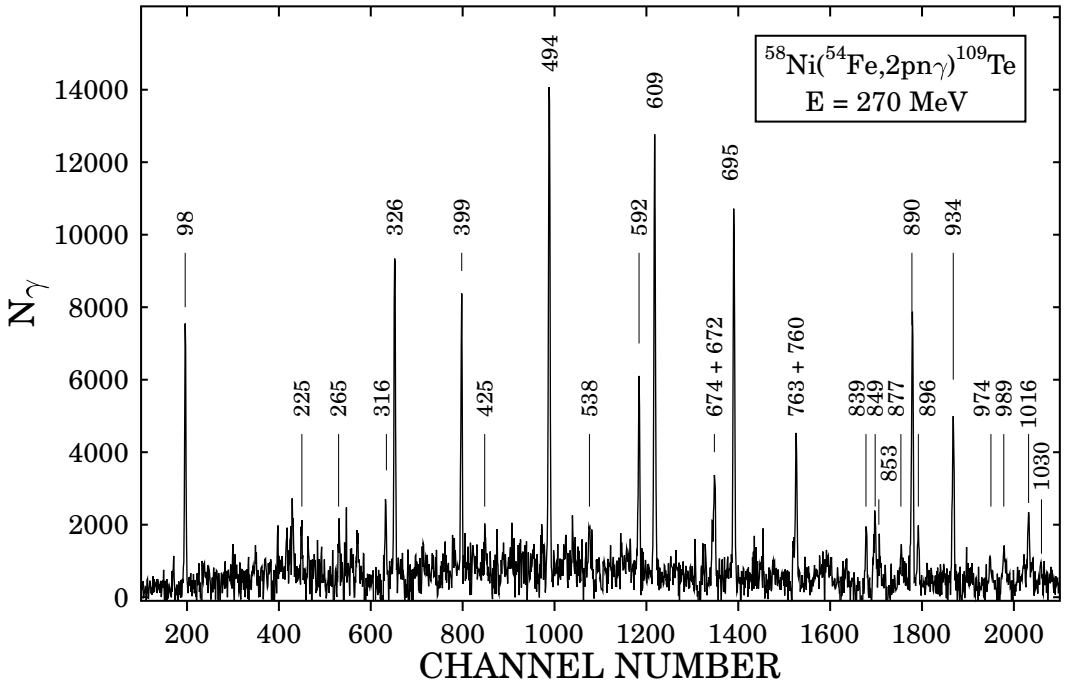

Figure 4.4: Total projection spectrum of ^{109}Te obtained from the sum of the 1n-, 1p1n-, and 2p1n-gated γ-γ matrices, after subtracting the contaminating channels.

To confirm the assignment of the γ rays to ^{109}Te the raW γ-γ matrices were used. From the measured intensity ratios, the strongest γ-rays in Fig. 4.4 were assigned to the reaction channel with the emission of two protons and one neutron, leading to the nucleus ^{109}Te.

The coincidence analysis was performed mainly on the cleaned, summed matrix, but all the coincidence relations were also checked in the original, 2p1n-gated γ-γ matrix. The energies and intensities of the γ-rays assigned to ^{109}Te are summarized in Table 4.2. They were deduced from the total projection spectrum and from γ-gated spectra. The relatively large errors of the intensities were due to the estimated systematic uncertainty caused by the matrix subtraction. Typical γ-gated spectra for ^{109}Te are shown in Fig. 4.5.

For the majority of the transitions γ-γ angular correlation ratios R_{ang} (see Section 2.6) were extracted from the experimental data, using the strong 494 and 98 keV γ-rays as gating transitions. The values of R_{ang} shown in Table 4.2.2 were used to determine the angular momentum transferred by the γ-rays. In the case of weak transitions the ratios R had too large errors to draw definite conclusions. Also, in

Table 4.2: Energies, relative intensities, angular correlation ratios R_{ang}, and angular momentum ΔI transferred by the γ-ray transitions assigned to ^{109}Te. Suggested spins and parities of the initial and final states of the transitions are given in the last column.

E_γ (keV)	I_γ (relative)	R_{ang}	ΔI ($\hbar$)	$I_i^\pi \rightarrow I_f^\pi$
98.1(1)	46(15)	0.99(13)	1	$(7/2_1^+) \rightarrow (5/2_1^+)$
224.6(5)	5(2)			$(9/2_2^+) \rightarrow (7/2_2^+)$
265.2(5)	5(2)			$(5/2_2^+) \rightarrow (5/2_1^+)$
316.2(2)	11(2)	1.65(67)		$(11/2_1^-) \rightarrow (11/2_1^+)$
326.1(1)	51(5)	0.75(10)	1	$(11/2_1^-) \rightarrow (9/2_2^+)$
398.7(1)	41(4)	0.80(12)	1	$(11/2_1^-) \rightarrow (9/2_1^+)$
424.5(5)	6(3)			$(9/2_1^+) \rightarrow (5/2_2^+)$
494.3(1)	100	1.47(22)	2	$(15/2_1^-) \rightarrow (11/2_1^-)$
537.6(5)	5(2)			$(7/2_2^+) \rightarrow (5/2_1^+)$
591.9(1)	40(4)	0.94(17)	1	$(9/2_1^+) \rightarrow (7/2_1^+)$
609.0(1)	99(9)	1.57(19)	2	$(19/2_1^-) \rightarrow (15/2_1^-)$
672.0(4)	13(2)	1.22(51)		$(37/2_1^-) \rightarrow (35/2_2^-)$
674.2(2)	28(5)	1.61(29)	2	$(11/2_1^+) \rightarrow (7/2_1^+)$
695.2(1)	96(9)	1.57(20)	2	$(23/2_1^-) \rightarrow (19/2_1^-)$
760.1(3)	15(4)	1.43(40)	(2)	$(15/2_1^+) \rightarrow (11/2_1^+)$
763.0(2)	44(6)	1.51(25)	2	$(9/2_2^+) \rightarrow (5/2_1^+)$
839.3(3)	15(5)	0.84(23)	1	$(37/2_1^-) \rightarrow (35/2_1^-)$
848.7(2)	17(5)	1.46(39)	(2)	$(35/2_1^-) \rightarrow (31/2_1^-)$
853.3(5)	9(2)	1.48(48)		
877.0(4)	14(4)	1.63(47)	(2)	$(33/2_1^-) \rightarrow (29/2_1^-)$
889.5(1)	88(8)	1.47(19)	2	$(27/2_1^-) \rightarrow (23/2_1^-)$
895.9(1)	20(4)	1.00(39)	(1)	$(29/2_1^-) \rightarrow (27/2_1^-)$
933.9(1)	61(6)	1.60(24)	2	$(31/2_1^-) \rightarrow (27/2_1^-)$
974.2(3)	7(3)	0.95(35)	(1)	
989.0(3)	16(3)	1.21(35)		
1015.9(2)	28(5)	1.88(41)	2	$(35/2_1^-) \rightarrow (31/2_1^-)$
1029.5(5)	6(3)	0.98(37)	(1)	

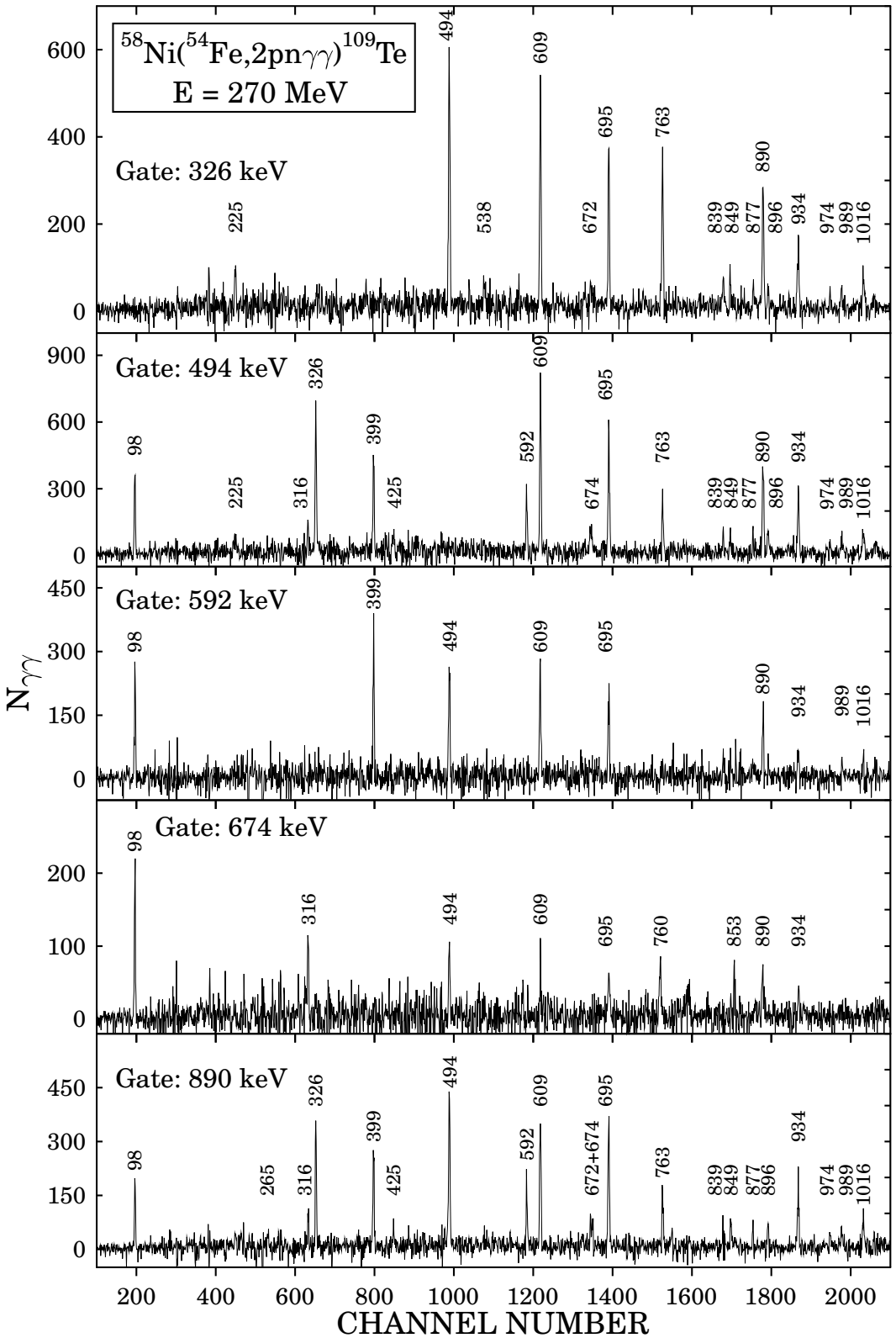

Figure 4.5: Typical γ-γ coincidence spectra of ^{109}Te obtained from the cleaned 2p1n-gated matrix. Transitions are labelled by their energy, in keV.

the analysis it was assumed that $\Delta I > 0$.

The experimental level scheme of ^{109}Te is shown in Fig. 4.6. The γ-ray lines from the four lowest-lying states of the negative-parity band have nearly equal intensities. Their ordering was based on the assumption that they form a quasi-rotational band. The order of the higher-lying transitions was well established on the basis of the coincidence and intensity relations. For the positive-parity band, the order of the γ-rays was determined by the intensity relations. The order of the 326 and 763 keV and the 399 and 592 keV γ lines, having nearly the same intensities, is also supported by the presence of the weak branches (225, 538 keV and 425, 265 keV γ-rays). In these two weak branches the more intense γ-rays in the gates, corresponding to higher-lying transitions, were placed at higher energy. The sum of the intensities of the 316, 326 and 399 keV γ-rays equals to the intensity of the 494 keV transition, so it seems that there is very little side feeding into the 1089 keV $(11/2^-)$ state.

The ground state of ^{109}Te was assigned $I^\pi = 5/2^+$ based on the systematics of light N=57 nuclei [82, 83]. The spin values assigned to the excited states were mainly obtained from the measured angular correlation ratios. The 98 keV ground state transition and the 592 keV transition had $\Delta I = 1$ character and thus the suggested spin values were 7/2 and 9/2, respectively, for their initial states. Positive parity was proposed on the basis of expectations from the above mentioned systematics. Similarly, the 763 keV ground state transition is most likely a stretched E2, which suggested spin 9/2 and positive parity for its initial state. Both the 326 and the 399 keV transitions had angular correlation ratios $R_{ang}\sim$0.8, consistent with stretched dipoles, indicating that the 1089 keV state had spin 11/2. We have tentatively assigned negative parity to this state on the basis of the systematics of heavier Te nuclei.

The spin values of the negative parity band were well established up to spin 35/2, since its states were connected by stretched E2 transitions. The large error in the angular correlation ratios of the weaker transitions did not allow for precise spin assignments for the higher lying states. The spin values in the side-band above 4673 keV came from the dipole nature of the inter-band and the quadrupole character of the intra-band transitions.

The two lowest-lying transitions of the positive parity side band had stretched quadrupole character, suggesting 11/2 and 15/2 spin to their initial states. The 11/2 spin assignment to the 772 keV level was in agreement also with the angular correlation ratios for the 316 keV and 674 keV transitions. The spin assignment of the states at 538 and 265 keV were proposed on the basis of theoretical considerations.

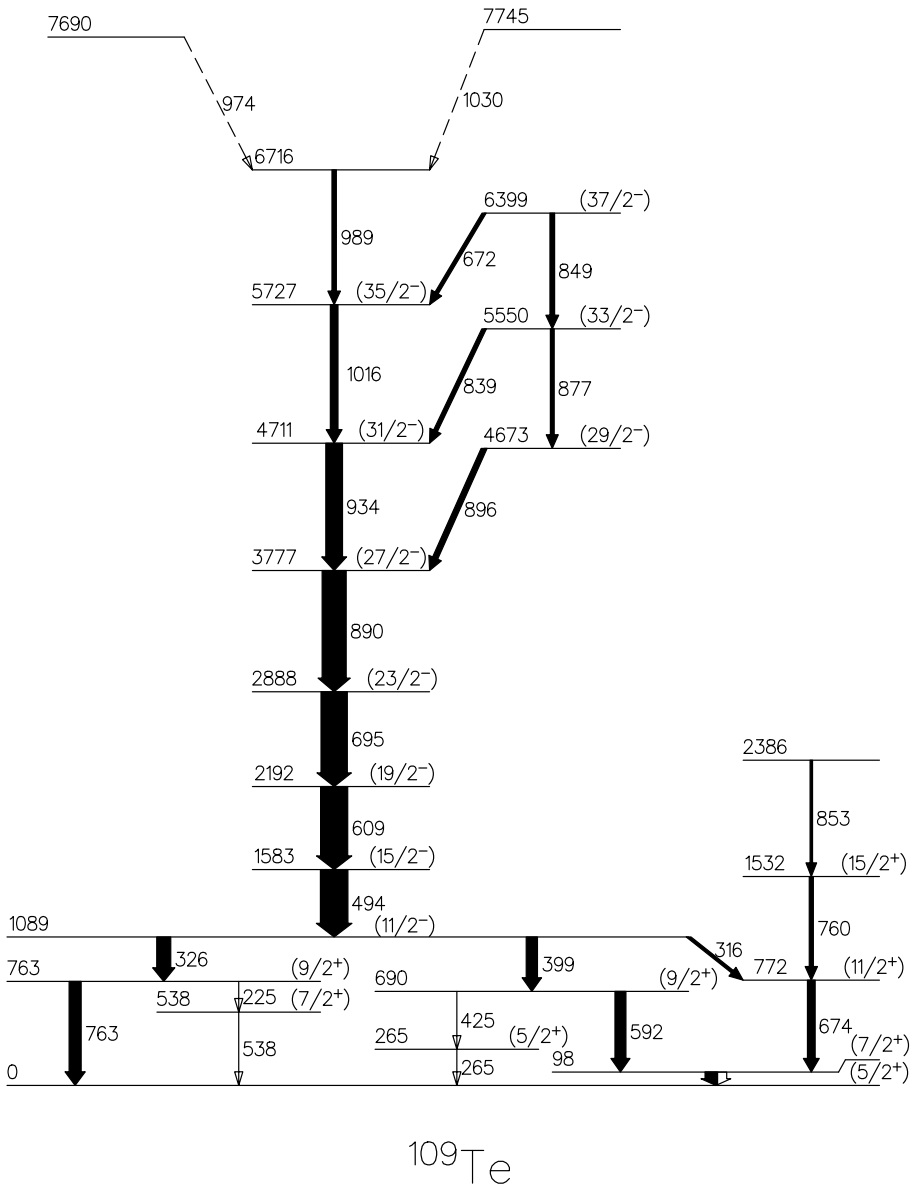

Figure 4.6: Proposed level scheme of ^{109}Te as obtained from the ^{54}Fe(^{58}Ni,2pnγ)^{109}Te reaction. All the spin values are tentative, and are given relative to the assumed ground state $I^{\pi} = 5/2^{+}$. The unfilled part of the 98 keV arrow reperesent the intensity of the conversion electrons, assuming pure M1 multipolarity.

The weakly populated positive-parity band was found to be yrast up to spin 15/2. The reason why it was not highly excited in the studied reaction might be because most of the feeding was gathered above spin 23/2 by the negative-parity band, and there was no mixing between the two bands due to their different parities.

4.2.3 The ^{110}Te nucleus

The ^{110}Te nuclei were produced by the evaporation of two protons from the compound nucleus ^{112}Xe. Due to imperfect proton detection, γ-rays from ^{110}Te were expected to appear in the 0p-, 1p- and 2p-gated γ-γ matrices, although not in the matrices gated with any number of α-particles or neutrons. The one- and two-proton gated matrices contain about the same amount of ^{110}Te events, which was consistent with an efficiency of about 65% for detecting protons in the Silicon detectors. The observed relative yield of ^{110}Te was only 0.8% of the total yield in the reaction. The strongest γ-rays in the 0p-, 1p- and 2p-gated matrices arise from nuclei produced in reaction channels of higher proton multiplicity. To select only γ-rays belonging to ^{110}Te the matrix subtraction procedure was applied (see 2.6). The strongest γ-rays which remained in this matrix originated from nuclei created by the evaporation of α-particles in addition to protons. The α channels were subtracted in a similar way. Contamination from neutron evaporation channels were also subtracted. Although not all contaminating γ-rays could be removed, the spectrum became significantly cleaner as it is shown in the projection spectrum of Fig. 4.7.

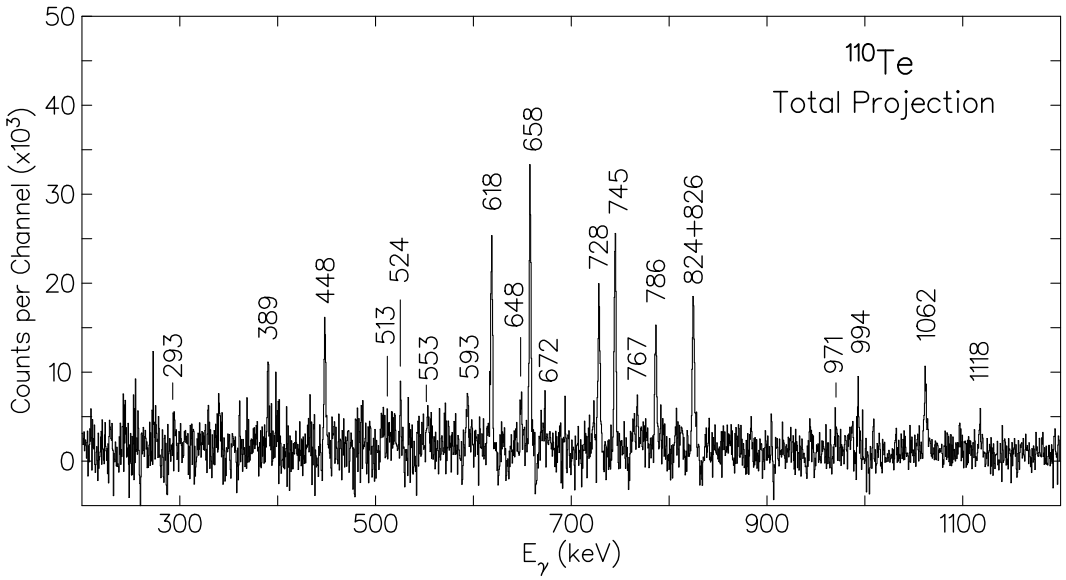

Figure 4.7: Projection spectrum of ^{110}Te obtained from the sum of the 1p- and 2p-gated γ-γ matrices, after subtracting the contaminating channels.

The strongest peaks in the subtracted spectrum were the 658 and 745 keV lines. In the original spectrum they were only about 3% of the strongest peaks, while in the cleaned spectrum the intensity of the strongest contamination was of that order. Previously a 656 keV line was assigned as the $2^+ \rightarrow 0^+$ transition in ^{110}Te [73].

The intensity ratio of the 658 keV γ ray in the 0p- and 1p-gated spectra, shown in Fig. 4.8, and the same intensity ratio of the 745 and 824 keV γ-rays, are found to be consistent with similar ratios for other known channels where two protons were emitted, e.g. the 1α2p channel, leading to ^{106}Sn. Since these transitions are not in coincidence with neutrons or α-particles, they are unambigously assigned to ^{110}Te.

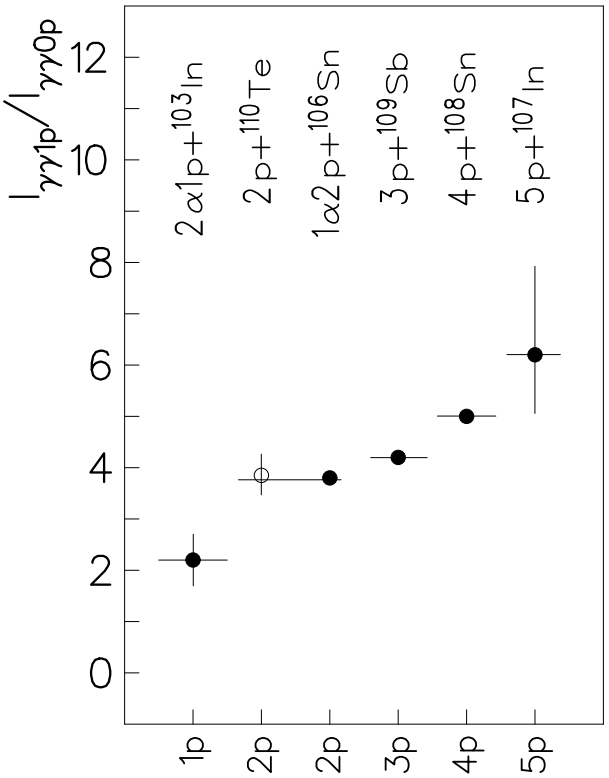

Figure 4.8: Experimental intensity ratios for different proton multiplicities. Comparisons with results obtained for known γ-rays (filled symbols) confirm the assignment of the 658 keV transition to ^{110}Te (open symbol).

Typical γ-γ coincidence spectra obtained from the sum of the 1p- and 2p-gated matrices are shown in Fig. 4.9. The proposed level scheme of ^{110}Te is shown in Fig. 4.10. It was constructed on the basis of the coincidence relations, and on conclusions drawn from energy and intensity balances. The energies and intensities of the γ-rays are given in Table 4.3.

The 658, 745 and 824 keV γ rays were found to be in coincidence with each other, and were suggested to be the lowest-lying transitions of the ground-state band in ^{110}Te. Their ordering was established by the small intensity differences, as well as by the coincidence relations of the weak side-feeding transitions. The ordering of the 813 and 767 keV transitions in band 2 could not be firmly established, and it may

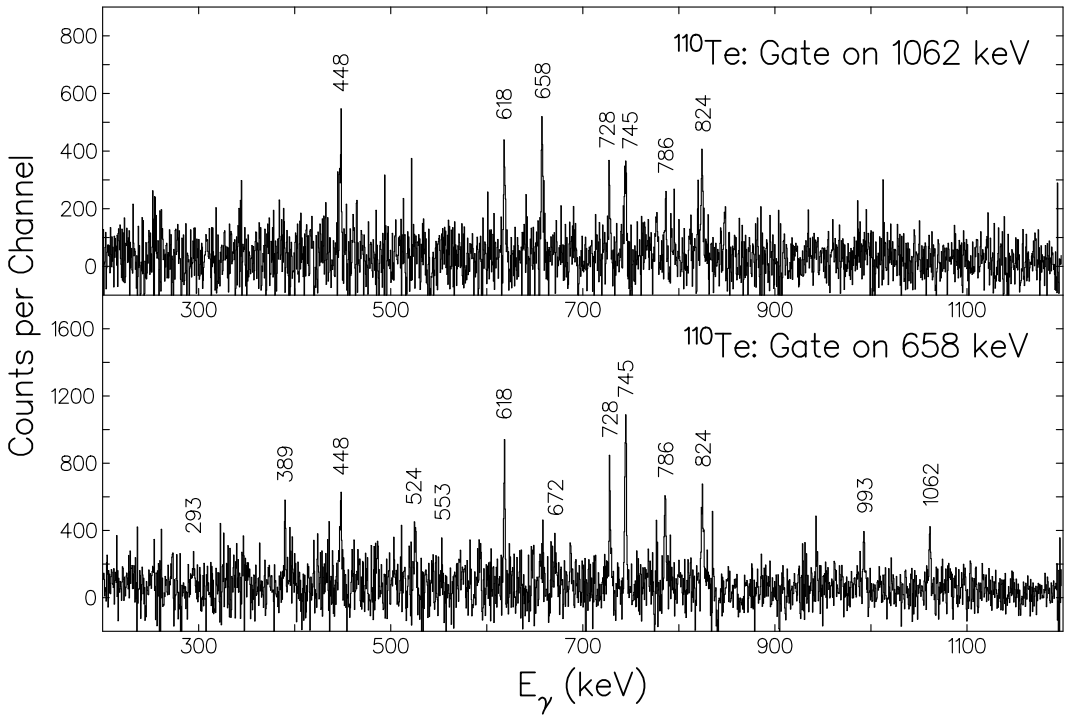

Figure 4.9: Typical γ-γ coincidence spectrum obtained from the sum of the 1p- and 2p- gated matrices.

be reversed. The main cascade of γ-rays (band 2) proceeded down to the 3737 keV state, where the γ-ray intensity was distributed into three branches. Three low-lying side-band structures were observed. In band 5 the 648 keV γ ray was found to be a doublet. Also a 555 and a 714 keV transition were present in the 648 keV γ gate, but they were too weak to be placed unambigously in the level scheme. The 994 keV transition was placed on top of the 6^+ state at 2227 keV. It was in coincidence with the lines above the 8^+ state at 3289 keV, but its coincidence relation with the higher-lying 1062 keV γ-ray line could not be firmly established, because the gated coincidence spectra were strongly contaminated. Several weak γ-ray lines, with energies of 260, 574, 688, 762 and 1035 keV were observed to feed into the lower part of the level scheme, but it was not possible to place them unambigously.

The spin values assigned to the levels were determined from the γ-γ angular correlation ratios They were determined for the majority of the transitions and are shown in Table 4.3. The 0^+, 2^+, 4^+, 6^+ and 8^+ values of the ground state band (band 3) were well established. The 448 keV line is clearly a stretched dipole, as is the 389 keV line. This suggested that the 3737 keV state has spin 9, on top of which an E2 cascade is observed. We have tentatively proposed that the spin 9 state has negative parity, based on the systematics of heavier even-A Te isotopes

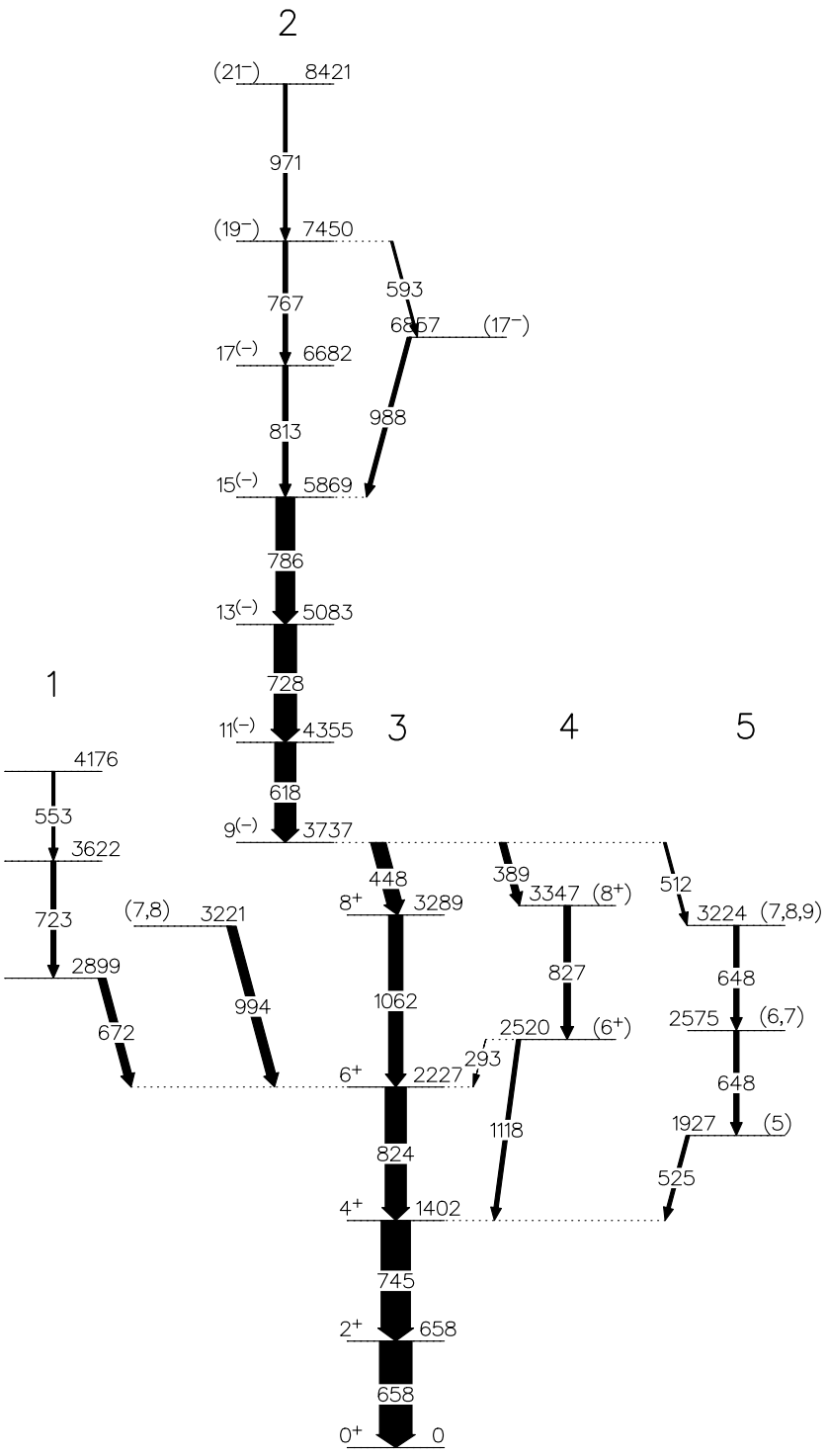

Figure 4.10: Experimental level scheme of ^{110}Te deduced from this work. The width of the arrows are proprotional to the relative intensity of the transition.

(see e.g. Fig. 4.11). The ratios R_{ang} had in many cases large errors making the spin assignments of the side-band structures difficult. No spin assignments were made to the states in band 1. Also the spin assignments of band 5 are tentative. Its 1927

Table 4.3: Energies, relative intensities, γ-γ angular correlation ratios, and spin assignments of γ-rays assigned to ^{110}Te.

E_γ [a] (keV)	I_γ	$R_{ang} = \frac{I_\gamma(\theta=143°)}{I_\gamma(\theta=79°,101°)}$	$I_i^\pi \rightarrow I_f^\pi$
293.4	12(2)		$(6^+)\rightarrow 6^+$
389.4	21(2)	0.96(20)	$9^-\rightarrow(8^+)$
447.6	46(2)	0.78(10)	$9^{(-)}\rightarrow 8^+$
513.1	8(2)		$9^-\rightarrow$(7,8,9)
524.5	11(2)		$(5)\rightarrow 4^+$
553.4	9(2)		4176$\rightarrow$3622
593.4	7(3)		$(19^-)\rightarrow(17^-)$
618.2	65(4)	1.51(17)	$11^{(-)}\rightarrow 9^{(-)}$
648.2	16(2)		(7,8,9)$\rightarrow$(6,7)
648.4	16(2)		(6,7)$\rightarrow$(5)
657.7	100	1.50(21)	$2^+\rightarrow 0^+$
672.1	24(4)		2899$\rightarrow 6^+$
723.3	15(2)		3622$\rightarrow$2899
728.1	69(4)	1.70(21)	$13^{(-)}\rightarrow 11^{(-)}$
744.7	91(5)	1.54(12)	$4^+\rightarrow 2^+$
767.3	14(3)		$(19^-)\rightarrow 17^{(-)}$
786.3	58(4)	1.57(22)	$15^{(-)}\rightarrow 13^{(-)}$
813.1	16(3)		$17^{(-)}\rightarrow 15^{(-)}$
824.4	65(4)	1.35(22)	$6^+\rightarrow 4^+$
826.7	20(3)		$(8^+)\rightarrow(6^+)$
971.2	11(3)		$(21^-)\rightarrow(19^-)$
987.1	13(2)		$(17^-)\rightarrow 15^{(-)}$
993.8	28(3)	1.12(24)	(7,8)$\rightarrow 6^+$
1062.2	44(2)	1.31(23)	$8^+\rightarrow 6^+$
1117.9	13(2)	1.24(56)	$(6^+)\rightarrow 4^+$

[a] The errors range from about 0.1 keV for the strongest lines to about 0.5 keV for the weaker ones.

keV state can have spin 4, 5 or 6. Spin 4 is less likely, since then one would expect an E2 transition to the 658 keV 2^+ state. Spin 6 is also unlikely, since then the 1927 keV state would be yrast, and it would be strongly populated. We therefore proposed spin 5 for this state. However, the assignments of the 2520 and 3347 keV states in band 4 are fairly well founded. The R_{ang} value for the 994 keV transition is 1.12(24), but since it is a complex line it was difficult to draw any conclusions concerning its multipolarity. We tentatively proposed spin 7 or 8 for the 3221 keV state.

In a recent experiment of Paul *et al* [79] performed in parallel to our work, the better quality of the data allowed to further extend the level scheme of ^{110}Te. The results of that work confirmed most of the results presented in this thesis, although a few discrepancies could be found, specially at highest spins, regarding the placement of certain levels and transitions. A new negative-parity even-spin band extending possibly up to $I^\pi = 20^-$ was also observed in that work.

4.3 Discussion

4.3.1 The ^{108}Te and ^{110}Te nuclei

The ^{108}Te nucleus have one proton pair and three neutron pairs outside the ^{100}Sn core, whereas ^{110}Te has one more valence neutron pair in addition to ^{108}Te. Hence, the low-lying states of these nuclei are expected to show vibrational behavior. Our discussion of the low-energy levels in the neutron deficient ^{108}Te and ^{110}Te will be based on the systematics of heavier Te nuclei. Fig. 4.11 shows the lowest-lying positive parity states and the first 9^- excited state in the even-even Te isotopes as a function of neutron number from $N = 56$ to $N = 82$. In the picture the latest spectroscopic data for ^{108}Te [76, 77] and ^{110}Te [79] are also shown.

To aid in the analysis the neutron single-particle levels of ^{110}Te were calculated using a deformed Woods-Saxon potential, and are shown in Fig. 4.12 as a function of the quadrupole deformation β_2. For qualitative arguments the diagrams can be used also for protons, keeping in mind that with 82 neutrons the $\pi g_{7/2}$ orbital lies lowest in the shell, whereas with 50 neutrons the $\pi d_{5/2}$ orbital lies lowest.

At the magic number N=82 the 2^+, 4^+ and 6^+ sequence of states has the typical characteristics of the $\pi(g_{7/2})^2$ multiplet. With decreasing neutron number the 2^+ and 4^+ states are lowered in energy, with a minimum around N=68, and in the middle of the shell the spectrum resembles that of a spherical quadrupole vibrator.

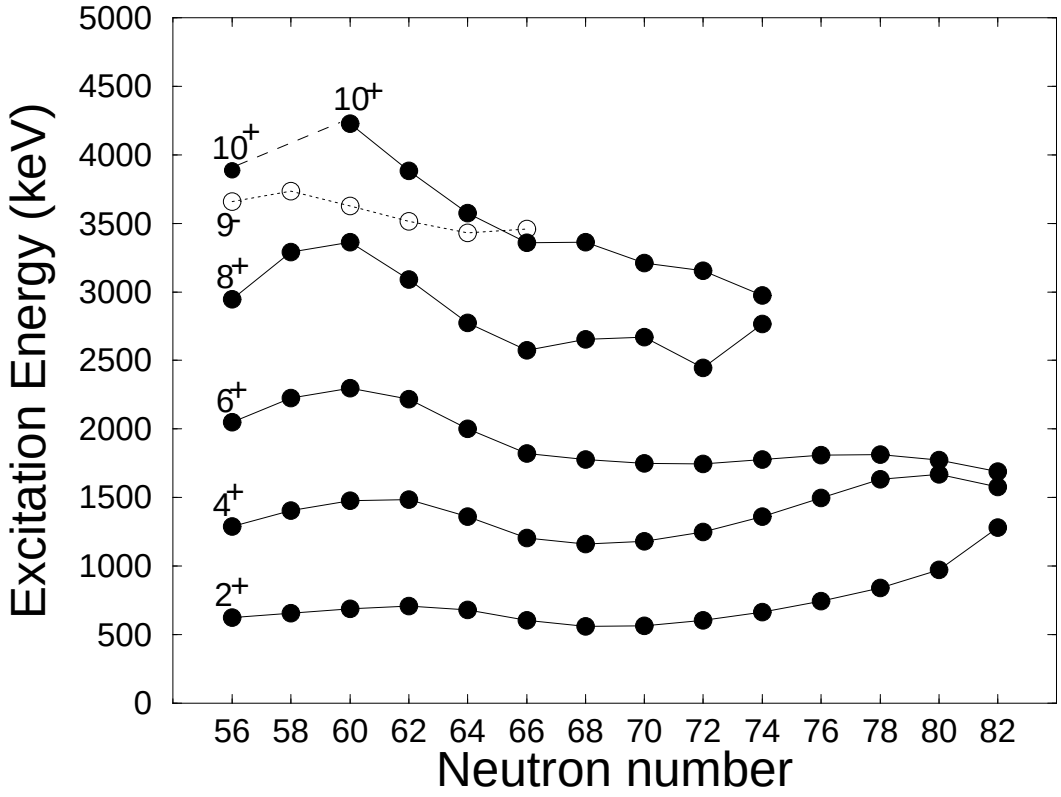

Figure 4.11: Systematics of yrast states in the even-even Te isotopes as a function of the neutron number.

This vibrational character appears to persist when going to the lighter Te isotopes, at least up to the 6^+ state, but we expect single-particle configurations to start mixing in the wave functions of higher-lying states.

Within this picture, the 2^+ and 4^+ states of ^{108,110}Te are interpreted as mainly 1- and 2-phonon excitations, respectively, built on the $[\nu d^2_{5/2}]_{2^+,4^+}$ configuration. The (6^+) state has probably both proton $[\pi g^2_{9/2}]_{6^+}$ and neutron $[\nu d_{5/2} g_{7/2}]_{6^+}$ contribution. The energy gap between the (6^+) three-phonon state and the (8^+) state is in agreement with the systematics, but the (8^+) state lies higher than expected for the four-phonon 8^+ state. If we follow the 2^+ – 8^+ sequence, it first increases in energy with decreasing neutron number due to the decrease in collectivity, and finally the sequence shows a very striking feature in the pronounced lowering of these states for N<60.(Fig 4.11). The change is most dramatic for the 8^+ state.

At magic number N=50 we expect a $\pi(d_{5/2})^2$ 0^+, 2^+, 4^+ multiplet, similar to the $\pi(g_{7/2})^2$ multiplet at N=82. At N=52 the neutrons and protons occupy the same kind of orbitals, forming isospin multiplets, with the well-known lowering of the T=0 singlet state, which may cause dramatic changes in the low-spin states. Thus, the lowering of the 2^+ – 8^+ sequence might be an effect caused by this proton-

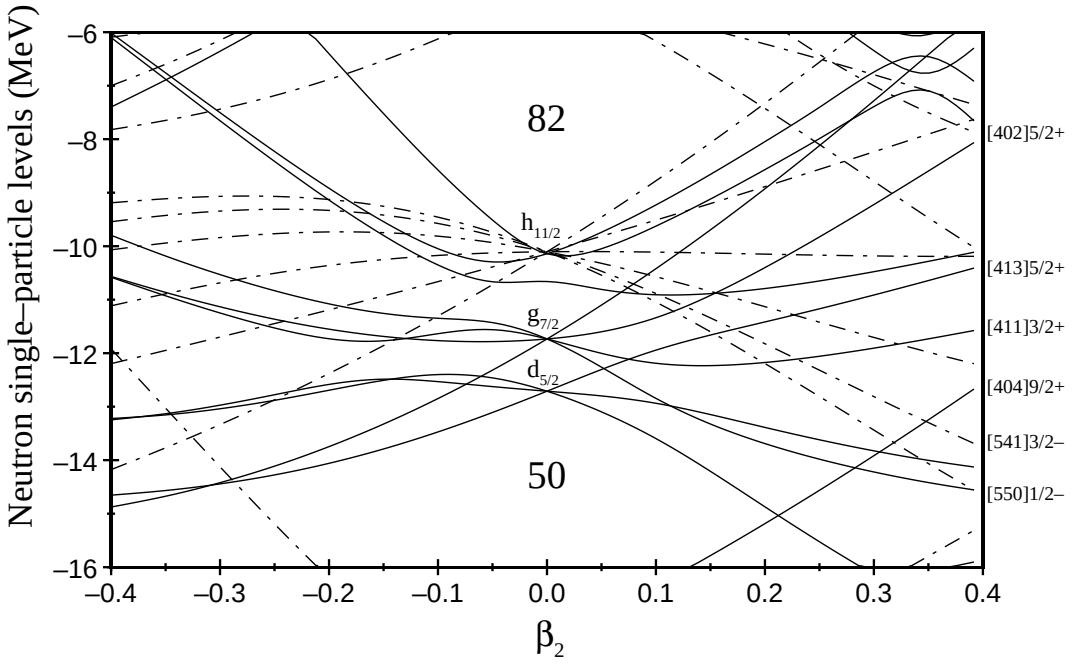

Figure 4.12: Neutron single-particle levels for ^{110}Te. The levels are labeled by their Nilsson quantum numbers $[Nn_z\Lambda]\Omega^\pi$.

neutron interaction. The 10^+ state is expected to have a strong component of the $\nu(h_{11/2})^2$ configuration. The energy of the 10^+ state decreases with increasing neutron number, which in the spherical approximation simply may be understood as the neutron Fermi surface moving closer to the $\nu h_{11/2}$ orbital (Fig. 4.12).

To further investigate the structure of the high-spin states in ^{110}Te, the Total Routhian Surface (TRS) of the lowest lying positive-parity configuration is shown in Fig. 4.13 at a rotational frequency of $\hbar\omega \approx 0.31$ MeV. In the calculations the deformed Woods-Saxon potential including the monopole pairing interaction was used, as described in Ref. [75]. Two minima are observed, one along the prolate collective axis and the other along the prolate non-collective axis. The calculated ground state deformation has $\beta_2 \approx 0.15$ and $\gamma \approx 1°$. With such a relatively large deformation the neutron Fermi surface lies close to the low-Ω $h_{11/2}$ orbitals (see Fig. 4.12), and one would expect to see a low-lying 9^- state, involving the $\nu h_{11/2}$ orbital, predominantly coupled to a $g_{7/2}$ neutron, but also a low-lying aligned $\nu(h_{11/2})^2$ 10^+ state. Only a $9^{(-)}$ state at 3737 keV was observed in our experiment, which is consistent with the systematics of the 9^- states in heavier Te isotopes. The 10^+ state has not been observed either in Ref. [79]. Interestingly, however, the observation of the 9^- and a 10^+ states in ^{108}Te has been reported very recently by Lane *et al* [77]. This may be related to the fact that in ^{110}Te the yrast line changes parity at the 9^- level.

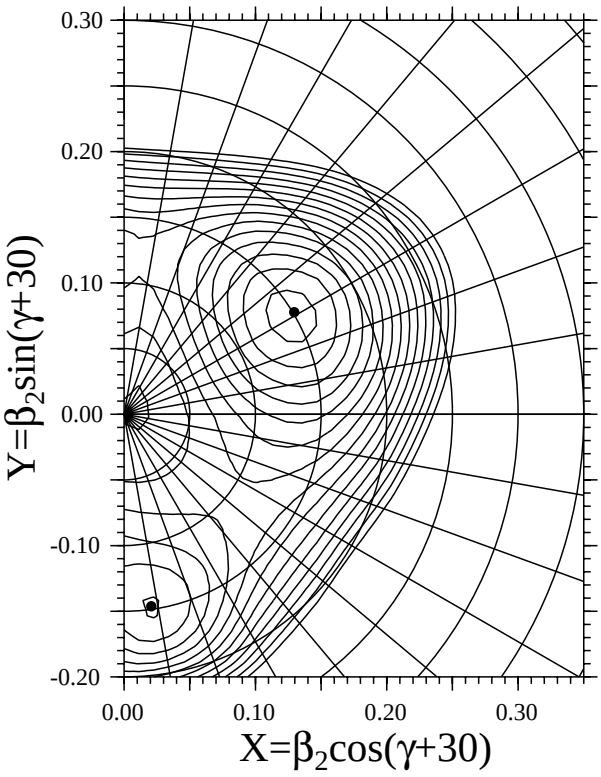

Figure 4.13: Total Routhian Surface calculation for the lowest lying (π, α)=(+,0), vacuum configuration at $\hbar\omega = 0.31$ MeV; two minima are seen: $\beta_2 \approx 0.15$, $\gamma \approx 1°$ and $\beta_2 \approx 0.15$, $\gamma \approx 111°$.

If we crank the Woods-Saxon potential at $\beta_2 = 0.15$ the quasi-neutron Routhians of Fig. 4.14 are obtained. The lowest quasi-neutron orbitals are the negative-parity states E and F with signature quantum numbers $\alpha = -1/2$ and $\alpha = +1/2$, respectively. They correspond to the $\nu[550]1/2^-$ orbital (see Fig. 4.12). The lowest positive-parity orbitals are B, A, C and D with signature quantum numbers –1/2, +1/2, +1/2 and –1/2, respectively. They correspond to the $\nu[411]3/2^+$ and $\nu[413]5/2^+$ orbitals or rather to a mixture of them. The lowest negative-parity two-quasiparticle state is thus obtained by the BE configuration. This gives rise to an odd spin-sequence consistent with the experimental observation. The unfavoured even-spin sequence from the signature partner AE lies at a higher excitation energy than the BE configuration as indicated by the calculated large signature splitting between them. It has not been observed in our experiment. However, in the paralell study of Ref. [79] a negative-parity even-spin sequence has indeed been observed up to high spins, which may be interpreted in terms of the AE configuration.

The aligned angular momentum i_x and the experimental Routhians e' of the

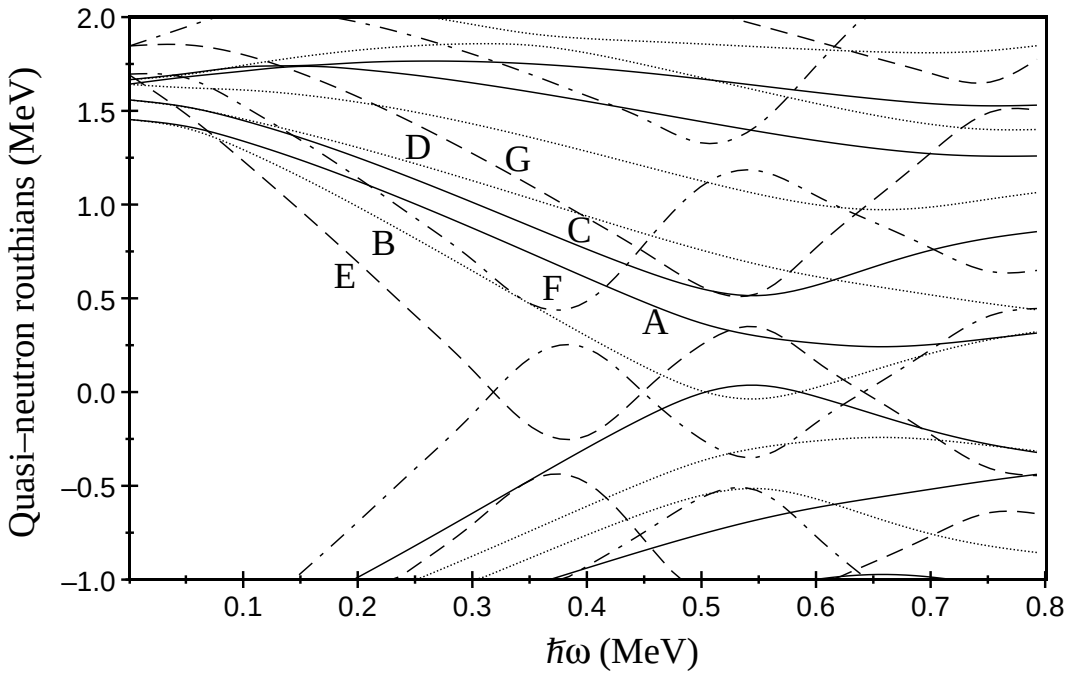

Figure 4.14: Quasi-neutron Routhians for β_2=0.15, β_4=0.0 and γ=0°.

yrast band has been plotted in Fig. 4.15 as a function of the rotational frequency $\hbar\omega$ using the prescription of Bengtsson and Frauendorf [78].

The $9^{(-)}$ band has an initial alignment of about 7.5 $\hbar$, which increases to about 14.5 $\hbar$ at $I^{\pi} = (21^{-})$, gaining 7 units of aligned angular momentum. The theoretical alignments of the bands can be estimated from the slope of the quasiparticle orbitals (Fig. 4.14). For the BE configuration $i_x \approx 7.5$ $\hbar$ and the four-quasiparticle neutron configuration BEFG is estimated to have $i_x \approx 15$ $\hbar$, which are very close to the experimentally measured alignments. On the other hand, the blocked FG crossing is calculated at $\hbar\omega_c \approx 0.60$ MeV, which is much higher than the experimentally observed frequency of $\hbar\omega_c \approx 0.39$ MeV (Fig. 4.15). However, the crossing frequency depends on the deformation. An increased deformation moves the neutron Fermi surface closer to the low-Ω $\nu h_{11/2}$ orbitals, which decreases $\hbar\omega_c$. Nevertheless, this deformation effect is calculated to be rather small, and cannot account for the large discrepancy between the calculated and experimental frequencies. Furthermore, it cannot be the ab proton crossing, since it is calculated both at a much higher frequency and with a much smaller alignment gain. One possibility is that the $9^{(-)}$ state is the $\pi(h_{11/2}g_{7/2})$ configuration in which case the observed band crossing could be the unblocked EF neutron crossing, which is calculated to $\hbar\omega_c \approx 0.40$ MeV. This is, however, unlikely since the $\pi(h_{11/2}g_{7/2})9^{-}$ state is expected at a higher excitation

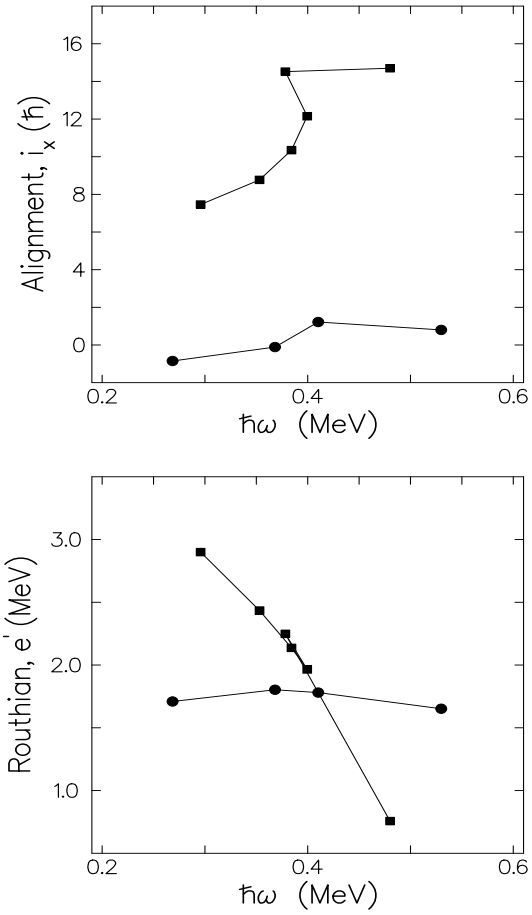

Figure 4.15: Experimental spin alignments i_x and experimental Routhians $e^{'}$ for the bands 2 and 3 of ^{110}Te plotted as a function of $\hbar\omega$ (circles=band 3; squares=band 2). The Harris parameters used for the reference configuration are J_0=7$\hbar^2$MeV^{-1} and J_1=20$\hbar^4$MeV^{-3}, and the value of the quantum number K used in the calculations are 0 for band 3 and 3 for band 2.

energy than the corresponding neutron configuration. The explanation must be sought elsewhere.

It was some time ago predicted that octupole degrees of freedom are important in the understanding of the structure of the light Te isotopes with N$\leq$60 [3].We have the situation that strong octupole correlations are expected for neutrons across the $d_{5/2}$-$h_{11/2}$ gap ($\Delta l = \Delta j = 3$). However, with the onset of quadrupole deformation and increasing spin the $h_{11/2}$ proton orbital is approching the Fermi surface, and one thus obtains a combined proton and neutron contribution to the octupole phonon. One might therefore speak in terms of deformation- and rotation-induced octupole effects, which might even lead to the onset of stable octupole deformation at high spin. Unfortunately, the ^{110}Te channel was too weak in our experiment to exploit this

interesting possibility in more detail. However, the $9^{(-)}$ state might correspond to an admixture of a two-quasiparticle configuration with the octupole phonon coupled to the 6^+ quadrupole vibrational state, bringing the $9^{(-)}$ state down in energy. The fact that the $9^{(-)}$ state decreases rather smoothly with neutron number, in contrast to the 10^+ state (see Fig. 4.11), also suggests that other than pure two-quasiparticle configurations may be involved. We therefore propose that band 2 is predominantly the BE configuration, with a possible admixture of an octupole phonon coupled to the 6^+ quadrupole vibrational state, and that the observed crossing is due to the alignment of the F and G neutrons, despite the inconsistency of the crossing frequency with the cranking model. In support of our arguments, strong E1 transitions were recently observed at high spins in ^{112}Te [67], in ^{110}Te [79], and in ^{108}Te [77] confirming the importance of octupole correlations in light Te isotopes.

The $9^{(-)}$ state decays strongly to the (8^+) state of band 4 via the 448 keV transition. Its B(E1) value is about 30% larger than the B(E1) value for the transition to the 8^+ state of band 3. It indicates that band 4 may have strong components of the $\nu g_{7/2}$ or $\nu h_{11/2}$ orbitals in its wave function, and its 6^+ and 8^+ state may be e.g. members of the non-aligned $\nu(h_{11/2})^2$ multiplet. This resembles the situation in ^{108}Cd and ^{110}Cd, where the aligned $\nu(h_{11/2})^2$ 10^+ state strongly decays into an 8^+ state, suggested to be a member of the non-aligned $\nu(h_{11/2})^2$ multiplet [80, 81].

As for band 1, band 5 and the state at 3221 keV there are several possibilities. The TRS calculation of Fig. 4.13 predicts a second minimum along the prolate non-collective axis, which originates from the K=8^+ $\pi(g_{9/2})^{-2}$ configuration. Other configurations expected to give rise to low-lying low-spin states in ^{110}Te are the neutron and proton $(d_{5/2})^2$, $(g_{7/2})^2$ and $(g_{7/2}, d_{5/2})$ configurations, and two broken pair configurations, such as the deformed proton four-particle two-hole intruder configuration.

4.3.2 The ^{109}Te nucleus

The ^{109}Te nucleus has one odd neutron in addition to the ^{108}Te core. On the basis of the systematics of light N=57 Cd and Sn nuclei [82, 83] low lying $d_{5/2}$, $g_{7/2}$ and $h_{11/2}$ quasi-neutron states and vibrational bands built on these states are expected to dominate the low-energy part of the spectrum. To make these expectations more quantitative we calculated the structure of ^{109}Te in the vibrational limit of the interacting boson-fermion model (IBFM).

The Hamiltonian of the interacting boson-fermion model was that of Eq. 3.6. The boson core was treated in the SU(5) limit of the IBM, adequate for vibrational nuclei.

The maximum number of bosons was 4, corresponding to the four valence nucleon pairs of the ^{108}Te core. The d-boson (phonon) energy E_d and the hexadecapole boson-boson interaction strength C_4, describing to what extent the 4_1^+ state is pushed up relative to the energy $2E_d$, were determined by adjusting them to the spectrum of ^{108}Te, resulting in $E_d = 0.62$ MeV and $C_4 = 0.15$ MeV. The parameter χ describing the static part of the quadrupole moment of the d-boson was deduced from the B(E2;$2_1^+ \rightarrow 0_1^+$) and $Q_{2_1^+}$ values of the ^{122,124}Te nuclei to be $\chi = -1.0$.

The shell model space consisted of the $s_{1/2}$, $d_{3/2}$, $d_{5/2}$, $g_{7/2}$, and $h_{11/2}$ subshells. The occupation probabilities were estimated in the BCS model using the Kisslinger-Sorensen parametrization [84]. The following values were adopted: $V^2(s_{1/2})$=0.17, $V^2(d_{3/2})$=0.05, $V^2(d_{5/2})$=0.59, $V^2(g_{7/2})$=0.28, and $V^2(h_{11/2})$=0.06. The relevant quasiparticle energies relative to the $d_{5/2}$ state were 0.11 MeV for the $g_{7/2}$ and 1.4 MeV for the $h_{11/2}$ orbital, obtained from the BCS calculations.

The boson-fermion coupling strengths were fitted to the energies of the positive parity states of ^{109}Te. The monopole interaction strength was 35 keV, which is a typical value in this mass region. The quadrupole-quadrupole interaction strength was 380 keV, corresponding to a weak particle-vibration coupling. The strength of the exchange interaction, which takes into account the microscopic structure of the phonon and in this way simulates the Pauli principle, was 800 keV.

The calculated and measured level energies are compared in Fig. 4.16, where also the main configurations of the calculated states are given. There is a good correspondence between the calculated and experimental energies. According to the calculations the ground state is the $d_{5/2}$ quasi-neutron state, and the first excited state is the $g_{7/2}$ neutron excitation. Its low energy is in agreement with the BCS calculations and also with the systematics in the sense that, in the N=59 nuclei, the $7/2^+$ state becomes the ground state. The two $9/2^+$ states are the 9/2 members of the $d_{5/2}\otimes 2_1^+$ and $g_{7/2}\otimes 2^+$ one-phonon multiplets, while higher spin positive parity states have mainly $g_{7/2}\otimes 2^+$, 4^+, 6^+ configurations. The negative parity states arise from the coupling of the $h_{11/2}$ neutron states to the yrast states of the ^{108}Te nucleus.

It is interesting to compare the vibrational bands built on the $7/2^+$ and $11/2^-$ states. The energy of the $\Delta I = 2$ γ-rays, taking away one phonon energy from the system, was consistently lower by about 160 keV in the negative parity band than in the positive parity one. As both sets of states were interpreted as a quasiparticle coupled to the yrast states of ^{108}Te, a possible explanation may be that the high-j intruder $h_{11/2}$ neutron increased the moment of inertia (the average deformation) of the soft Te core by polarization. On the other hand, the IBFM describes well

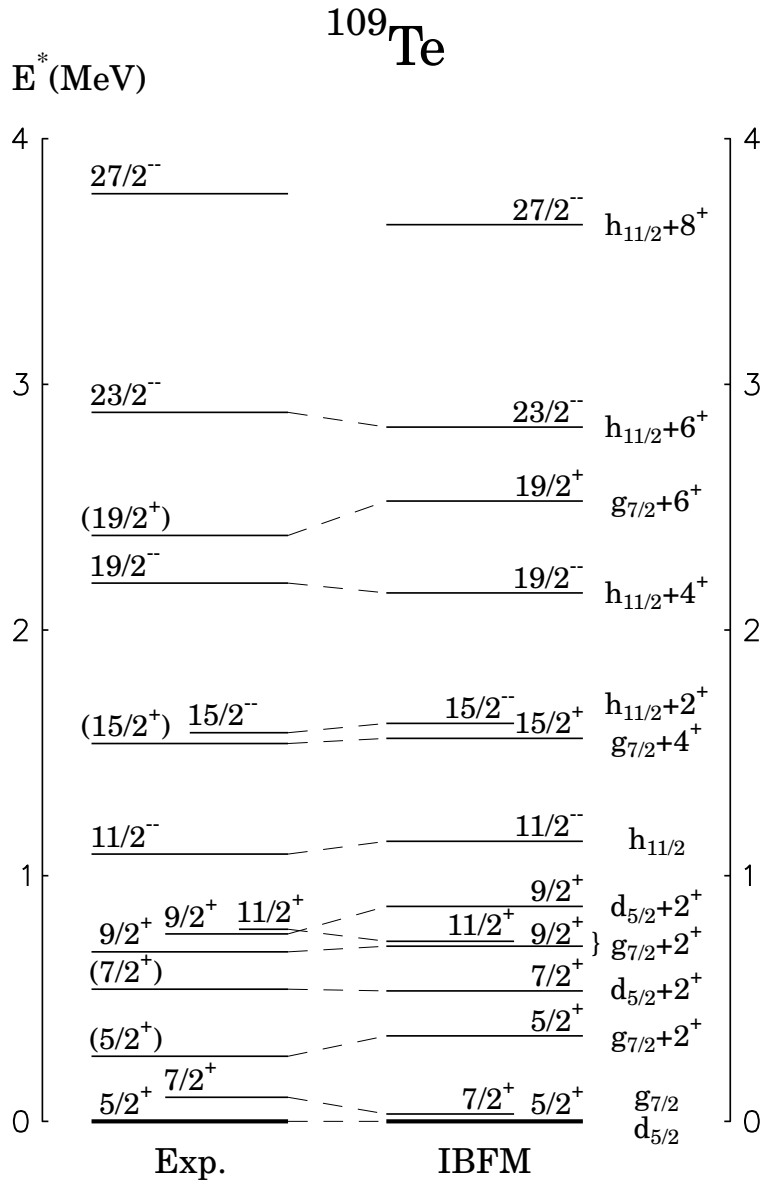

Figure 4.16: Comparison of the experimental levels with the theoretical calculations based on the interacting boson–fermion model. On the right hand side of the figure the main components of the calculated wave functions are also given.

this difference, but cannot account for polarization phenomena. According to these calculations, the way of particle–vibration coupling changed. In this model, as in all relevant particle–vibration coupling models, the particle is coupled to the core via the conventional quadrupole–quadrupole interaction, and via the exchange interaction, which is applied to describe the so called $j-1$ effect [85]. The effective strength of the quadrupole–quadrupole interaction is proportional to (U^2-V^2), while that for the exchange interaction is approximately proportional to UV. Thus, in the case

of the nearly empty $\nu h_{11/2}$ quasiparticle state the quadrupole-quadrupole coupling is dominant, while in the case of the much more filled $\nu g_{7/2}$ quasiparticle state the exchange force also plays a significant role. This may explain the above mentioned energy difference in the two bands.

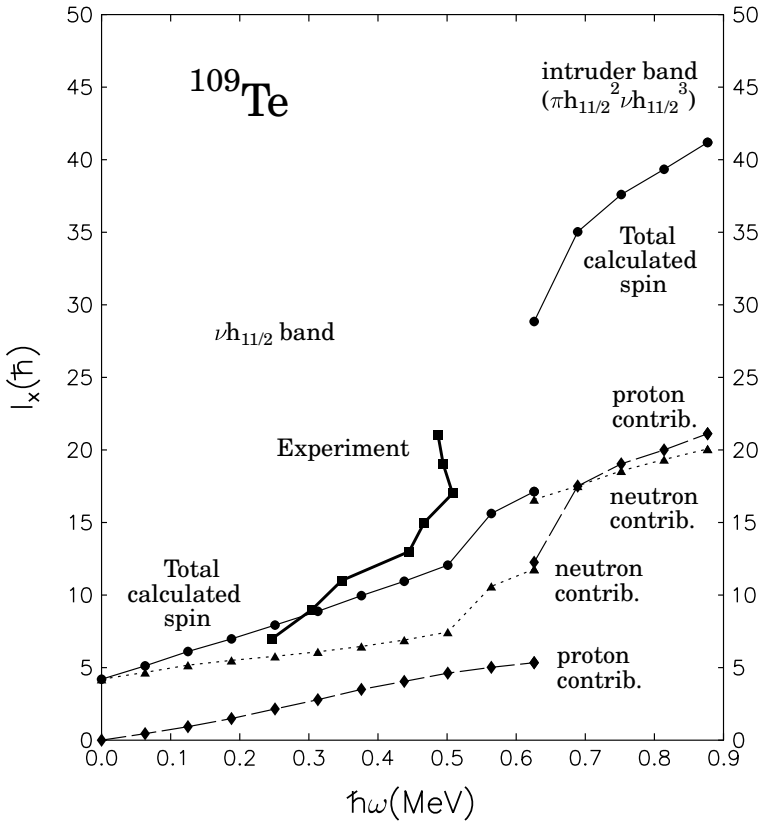

Figure 4.17: Comparison of experimental and calculated spin I_x for the observed negative-parity band in ^{109}Te.

The highest spin expected in IBFM is 27/2, as the core has eight valence particles, enough for four phonons. However, the negative parity band is not terminated at $27/2^-$. The classical way to investigate the nature of the high spin states is based on the analysis of the spin along the rotational axis, $I_x = \sqrt{(I+1/2)^2 - K^2}$ as a function of the rotational frequency $\hbar\omega(\approx E_\gamma/2)$. Such a plot is shown in Fig. 4.17. The experimentally extracted spin I_x was compared to cranked Strutinsky calculations, based on the deformed Woods-Saxon potential (see Section 3.3).

In the cranking model the first $\nu h_{11/2}$ crossing is blocked, due to the occupation of that orbital. The small increase in angular momentum at $\hbar\omega \approx 0.45$ MeV coincided with the calculated alignment of $g_{7/2}$ neutrons. In addition there was a smooth alignment due to $g_{7/2}$ protons, with a very large interaction (Fig. 4.17). However,

the total calculated angular momentum was smaller by $\sim 2\hbar$ than the experimental one. A possible mechanism for this discrepancy might be related to the vibration-rotation coupling, which is beyond the scope of the cranking model. The coupling to e.g. one aligned quadrupole phonon might thus be responsible for the above discrepancy.

At even higher frequency, $\hbar\omega \approx 0.5$ MeV, a pronounced angular momentum increase was present in the data (Fig. 4.17). In the even-even isotope ^{112}Te, a well developed rotational band has been observed, based upon the proton $h_{11/2}$ intruder orbital [67]. In our calculations, a crossing with the $\pi(h_{11/2})^2$ band was expected to occur around $\hbar\omega \sim 0.6$ MeV. At that frequency, one also expected the first unblocked $h_{11/2}$ neutron crossing.

Protons, as well as neutrons occupying the $h_{11/2}$ orbital strongly polarize the quadrupole deformation to larger values (from $\beta_2 = 0.14,\ \gamma = 15°$ to $\beta_2 = 0.22,\ \gamma = 10°$). The alignment gain at $\hbar\omega = 0.5$ MeV might thus be interpreted as a crossing with the more deformed $\pi(h_{11/2})^2\nu(h_{11/2})^3$ configuration. A comparison of that crossing with the one in the intruder band of the even-even Te-isotopes yields that it takes place later in the calculations than in the experiment. Since, however, the present data were not followed to higher spin values, one has to be careful with a definite assignment, and the discussion of the possible alignment at $\hbar\omega = 0.5$ MeV is therefore somewhat speculative.

Chapter 5

Structure of ^{98}Pd and ^{100}Pd nuclei

5.1 Previous studies

Prior to our work, low-spin states of ^{98}Pd had been investigated via EC-β^+ decay of ^{98}Ag [86], and in a two-proton transfer experiment with the reaction ^{96}Ru(^{16}O,^{14}C) [87]. Later on, high-spin states of ^{98}Pd were studied by Piel and Scharff-Goldhaber [88] using the ^{70}Ge(^{32}S,2p2nγ)^{98}Pd reaction. In that study positive-parity yrast states of ^{98}Pd were observed up to spin 14$\hbar$. A γ-ray transition of 720 keV tentatively extended the level scheme to angular momentum of 16$\hbar$. In the experiment, γ-ray excitation functions, the angular distribution of γ-rays, and γ-γ coincidences were measured. The obtained results were compared to shell model calculations [89], and to predictions from the variable model of inertia (VMI) model.

In the case of ^{100}Pd, a level scheme with a ground-state positive-parity band extending to I$^\pi$=14$^+$ and two negative-parity bands was published in Ref. [90]. Excitation functions, and γ-ray angular distribution and linear polarisation measurements were performed using the ^{91}Zr(^{12}C,3nγ)^{100}Pd reaction. The observed states were interpreted in the framework of the interacting boson model (IBM), and also the experimentally observed backbends for the neighbouring odd- and even-A Pd isotopes were compared to calculations from a 'rotor plus two quasiparticle' model. During the course of our work, new results somewhat contradictory to the previous ones have been published by Tandel *et al* as a short note [91]. The ^{66}Zn(^{37}Cl,p2n)^{100}Pd reaction was used in combination with an array of eight Compton-supressed Ge detectors. On the basis of γ-γ coincidence data the level ordering in the negative-parity band was rearranged and a modification of the corresponding spin values was proposed. These data were similar to the preliminary results from our NORDBALL experiment, which were presented in Ref. [92].

The heavier ^{102,104,106}Pd isotopes have been extensively studied in the past using (HI,xnγ) reactions (see, e.g. Ref. [90, 93]. Quasi-rotational behaviour has been observed at high spin in these nuclei in the form of collective bands of positive-parity as well as negative-parity (even- and odd-spin) states. These states were interpreted as rotations of the core built on two-quasiparticle excitations involving the $\nu d_{5/2}$, $\nu g_{7/2}$ and $\nu h_{11/2}$ configurations. Very recent studies [24] have identified terminating bands in ^{102}Pd, predicted in the cranking formalism [4].

5.2 Experimental results

In this section new experimental results obtained in our work for ^{98,100}Pd nuclei are presented. In the case of ^{100}Pd, the results are based from both the NORDBALL (Section 2.3.1) and the EUROGAM II (Section 2.3.2) experiments.

5.2.1 The level scheme of ^{98}Pd

The ^{98}Pd nuclei were produced in our experiment after the evaporation of two protons and two α-particles from the compound nucleus ^{108}Te, representing $\sim$1.9% of the total reaction yield. Thus, for the γ-ray coincidence analysis the 2p2α-gated E_γ-E_γ matrix was used. This matrix appeared to be relatively clean, and contained only small contaminations mainly from the 3p2α channel (^{97}Rh). Typical γ-ray gated spectra obtained for ^{98}Pd are shown in Fig. 5.1. Energies and relatives intensities of γ-rays, assigned to ^{98}Pd from our experiment, as well as angular correlation ratios R_{ang}, serving the basis for spin assignments, are listed in Table 5.1. We recall that for stretched quadrupole transitions R_{ang} $\sim$1.5, whereas for stretched dipole transtions R_{ang} $\sim$0.8.

In the analysis about 40 new γ-ray transitions were assigned to ^{98}Pd, considerably extending its previous level scheme. The new level scheme of ^{98}Pd, deduced from our experiment is shown in Fig. 5.2. Our analysis confirmed the previous results of Piel *et al* [88] for the positive-parity even-spin band up to spin 14$\hbar$. However, in our level scheme a hitherto unknown 926 keV γ line was observed feeding the 5071 keV 14^+ level, instead of the previously thought 721 keV γ-ray, which had to be moved on top of the 926 keV one. In addition, the $\sim$721 keV γ-ray transition was found to be self-coincident in our data set. The R_{ang} ratio for the 721 and 926 keV suggested these transitions were of dipole character, supporting the assignment of I^π=15^+ and 16^+ to the 6627 and 7349 keV levels, respectively. On top the 721 keV line we placed a 1160 keV γ-ray, possibly extending the sequence up to (18^+).

Paralell to the 1160 keV various branches were observed going to as high as 10.8 MeV in excitaion energy, but no firm multipolarity assignments could be inferred for these γ-ray transitions from our data. Our analysis corroborated also the placement of the 1079 keV γ-ray depopulating the 5^- level at 2620 keV. For the first time we have observed a cascade of stretched quadrupole transitions (the 759, 767 and 495 keV lines) feeding this level.The angular momentum taken away by the γ-rays was deduced from their angular correlation ratios R_{ang} (see Table 5.1).

The 11^- state at 4642 keV was in turn strongly fed via a cascade of three γ-ray transitions of 1342, 337 and 838 keV. Both the 337 keV and the 838 keV γ lines were assumed to be stretched dipoles. The character of the 1342 keV transition, based on

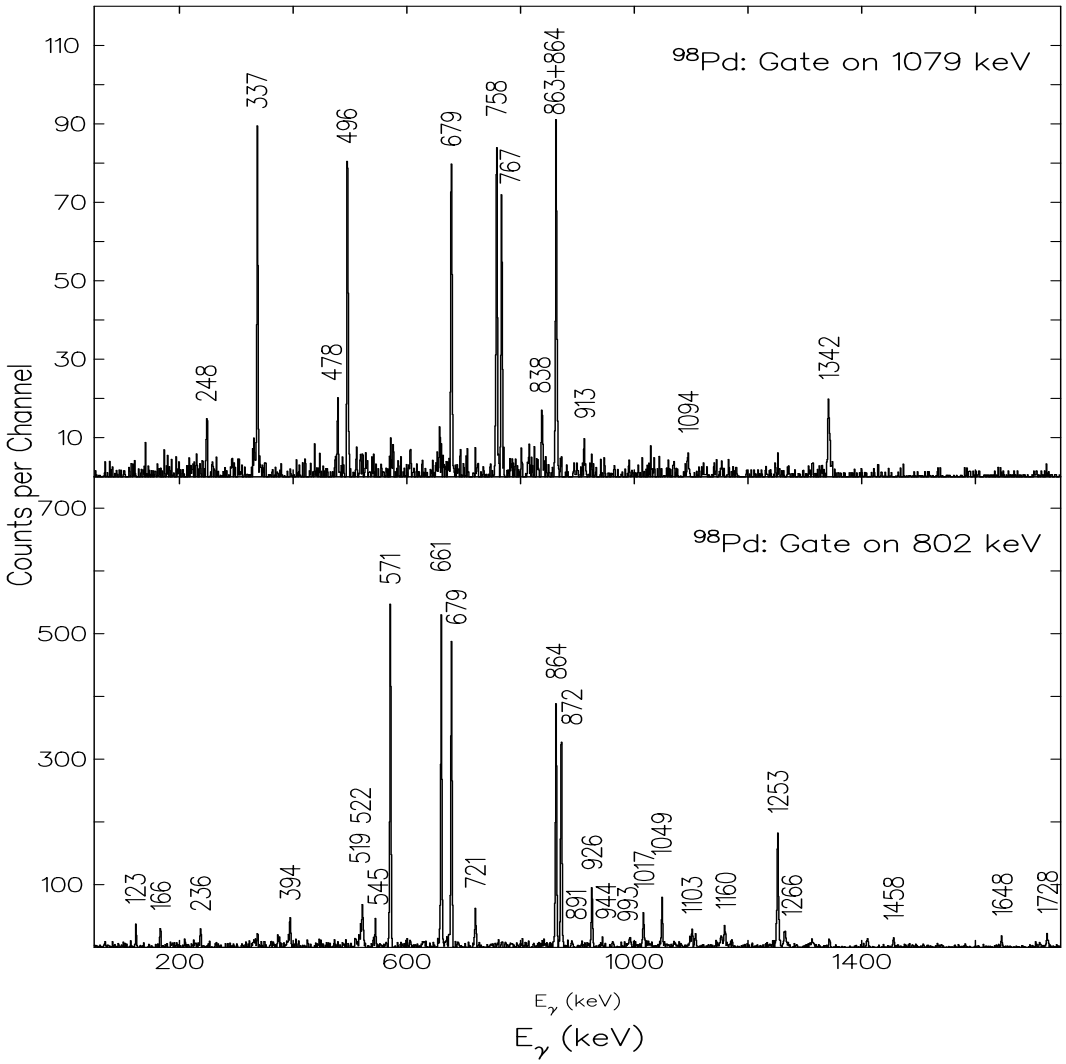

Figure 5.1: Gamma-ray gated spectra corresponding to ^{98}Pd obtained from the 2p2α-gated γ-γ matrix.

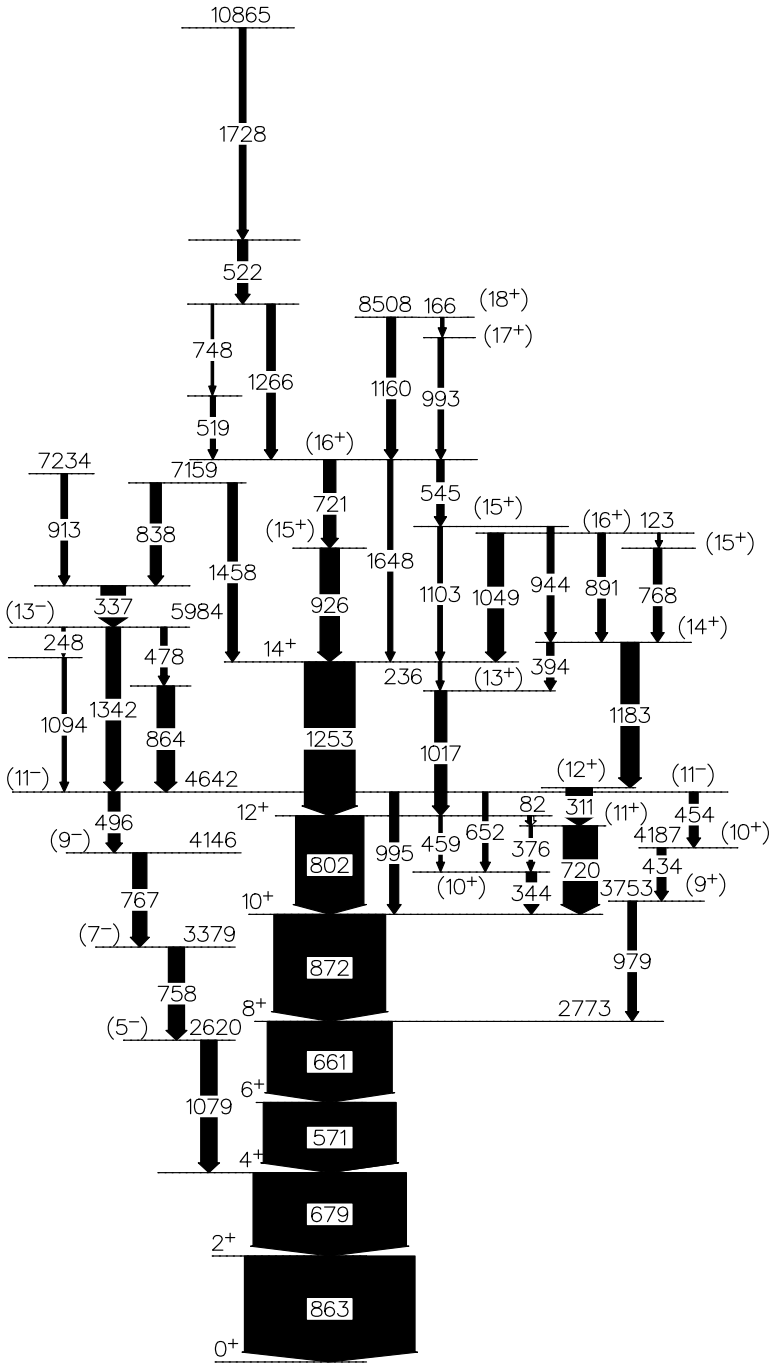

Figure 5.2: Proposed level scheme of ^{98}Pd. Tentative spin and parity assignments are shown in parentheses.

the measured angular correlation ratio, might be either of a stretched quadrupole or a non-stretched dipole transition. Since the 4642 keV level was reached from that at 5984 keV also by a pair of cascades of two γ-rays each, it is suggested that the spin difference between the two levels is $2\hbar$. The 1342 keV transition was therefore suggested to be a stretched $E2$, and the level at 5984 keV was assigned spin $13\hbar$.

The 11^- state was depopulated not only throughthe above mentioned $E2$ cascade to the 2620 keV level, but also via an alternative branch consisting of the 454 keV, the earlier observed 434 keV and the 979 keV γ-rays. The placement of the 434 keV transition is different in our proposed level scheme from that of Ref. [88] since it was observed in the $8^+ \rightarrow 6^+$ 661 keV gate. The character of the 434 keV and 454 keV transitions are those of a stretched dipole transition bringing the the total angular momentum down to $9\hbar$. This means that the 979 keV transition should be a dipole. Its intensity ratio was, however, closer to that of a stretched quadrupole. The observed intensity ratio could be understood if the 979 keV transition were a mixed M1/E2 transition going from 9^+ to 8^+.

The placement of the rest of the γ-rays shown in Fig. 5.2 was well established by the coincidence relations, and the suggested spin assignments were supported by the measured angular correlation ratios listed in Table 5.1.

Table 5.1: Energies, intensities, angular correlation ratios and spin assignments of γ-rays assigned to ^{98}Pd.

E_γ(keV)	I_γ	R_{ang}	I_i^π	I_f^π
82.2	25 (2)	0.79 (0.11)	12^+	(11^+)
123.0	25 (1)	0.75 (0.07)	(16^+)	(15^+)
165.9	26 (1)	0.60 (0.05)		
236.4	20 (1)	0.56 (0.07)		
247.8	29 (1)	0.76 (0.07)		
310.7	168 (2)	0.79 (0.02)	(12^+)	(11^+)
336.9	177 (2)	0.79 (0.02)		
343.8	64 (1)	1.33 (0.05)	(10^+)	(10^+)
376.4	26 (1)	0.38 (0.06)		
394.5	39 (2)	0.69 (0.06)	(14^+)	(13^+)
434.1	45 (2)	0.89 (0.07)	(10^+)	(9^+)
454.4	61 (2)	0.78 (0.06)	(11^-)	(10^+)
478.2	43 (2)	0.65 (0.07)		
495.6	84 (2)	1.49 (0.08)	(11^-)	(9^-)
518.9	47 (2)	0.88 (0.09)		
521.9	81 (2)	0.68 (0.04)		
544.8	53 (2)	0.56 (0.06)		
571.2	814 (7)	1.38 (0.02)		
652.4	18 (2)	0.81 (0.15)	(11^-)	(10^+)

Table 5.1: continued

E_γ(keV)	I_γ	R_{ang}	I_i^π	I_f^π
660.8	794 (7)	1.41 (0.02)		
678.6	902 (8)	1.45 (0.02)		
720.5[1]	269 (4)	0.86 (0.02)	(11^+)	10^+
			(16^+)	(15^+)
748.0	16 (2)	1.08 (0.27)		
758.5	90 (3)	1.49 (0.09)	(7^-)	(5^-)
767.0	87 (5)	1.50 (0.18)	(9^-)	(7^-)
768.7	43 (6)	0.85 (0.24)	(15^+)	(14^+)
802.5	396 (5)	1.37 (0.03)		
838.5	70 (3)	0.73 (0.06)		
862.9[1]	1000 (0)	1.38 (0.02)	2^+	0^+
872.1	701 (6)	1.46 (0.02)		
891.4	72 (3)	1.27 (0.09)	(16^+)	(14^+)
912.7	50 (2)	0.78 (0.08)		
925.9	138 (3)	0.89 (0.04)	(15^+)	14^+
944.1	61 (3)	0.86 (0.09)	(15^+)	(14^+)
979.2[2]	50 (3)	1.62 (0.16)	(9^+)	8^+
992.4	51 (3)	0.84 (0.09)		
995.2	49 (3)	0.73 (0.08)	(11^-)	10^+
1017.4	95 (3)	1.12 (0.07)	(13^+)	12^+
1049.2	106 (3)	1.38 (0.08)	(16^+)	14^+
1078.6	86 (3)	0.70 (0.05)	(5^-)	4^+
1094.5	37 (3)	0.75 (0.10)		
1103.1	27 (3)	0.98 (0.20)	(15^+)	14^+
1160.3	59 (3)	1.25 (0.11)	(18^+)	(16^+)
1182.9	126 (3)	1.43 (0.08)	(14^+)	(12^+)
1253.2	346 (5)	1.39 (0.05)		
1266.5	59 (3)	1.25 (0.11)		
1342.1	99 (4)	1.30 (0.09)	(13^-)	(11^-)
1456.9	26 (2)	0.98 (0.18)		
1647.5	30 (2)	1.28 (0.17)	(16^+)	14^+
1728.5	68 (3)	0.50 (0.05)		

[1] Doublet. [2] See text.

5.2.2 The level scheme of ^{100}Pd

The NORDBALL experiment

In this experiment, the ^{100}Pd nuclei were populated by the evaporation of 4 protons and 1 α-particle from the compound nucleus ^{108}Te. The relative yield of this channel was ~2.5% with respect to the total observed yield. Thanks to the high charged-particle multiplicity of the events leading to ^{100}Pd, leakages from higher multiplicity charged-particle channels represented only a few percents of the events in the corresponding E_γ-E_γ matrix. The main contaminant lines originated from the 4p1α1n reaction channel (one misdetected neutron), leading to ^{99}Pd, and from the 3p2α0n channel (one α-particle detected as a proton), leading to ^{97}Rh. These contaminants did not disturb the γ-γ coincidence analysis. Sample γ-ray coincidence spectra gated by the 876, 892 and 1089 keV transitions are shown in the upper part of Fig. 5.3.

The multipolarities of γ-rays were determined using the simplified γ-ray angular correlation analysis described in Section 2.6.2. The energies, intensities and angular correlation ratios of γ-rays assigned to ^{100}Pd are given in Table 5.2.

Table 5.2: Energies, relative intensities and angular correlation ratios for γ-ray transitions assigned to ^{100}Pd from the ^{50}Cr(^{58}Ni,4p1α)^{100}Pd reaction. The linear polarisation values P were determined from the ^{70}Zn(^{36}S,6n)^{100}Pd reaction. The proposed spin and parity for the levels is also listed.

E_γ(keV)	I_γ(rel.)	R_{ang}	P	E_i(keV)	$I^\pi \rightarrow I^f$
190.3(1)	16.1(7)	1.44(7)	1.37(99)	3178	$8^+ \rightarrow 8^+$
209.3(2)	1.3(1)	0.89(19)		3231	$7^- \rightarrow 6^{(-)}$
213.7(1)	0.5(1)			4093	$9^- \rightarrow (8^-)$
254.1(1)	0.3(1)			5707	$14^+ \rightarrow 13^{(+)}$
261.6(2)	1.4(1)			3440	$8^+ \rightarrow 8^+$
276.6(2)	3.2(2)	1.47(14)		4146	$10^+ \rightarrow 10^+$
280.4(2)	1.5(2)	1.43(20)		2470	$6^+ \rightarrow 6^+$
311.4(4)	0.3(1)			4946	$11^- \rightarrow 10^{(-)}$
374.6(2)	1.4(1)	0.78(17)		5453	$13^{(+)} \rightarrow (12)^+$
450.7(2)	0.7(1)	0.77(30)		2505	$5^- \rightarrow (4^-)$
465.9(1)	6.8(4)	0.68(6)	−0.30(34)	5918	$14^+ \rightarrow 13^+$
479.4(1)	5.8(2)	0.63(15)	−0.64(59)	6938	$16^+ \rightarrow 15^+$
516.3(1)	1.6(2)			3022	$6^{(-)} \rightarrow 5^-$

Table 5.2: continued

E_γ(keV)	I_γ(rel.)	R_{ang}	P	E_i(keV)	$I^\pi \rightarrow I^f$
526.5(1)	1.3(1)			5453	$13^+ \rightarrow 12^+$
540.5(1)	1.3(3)	0.85(27)		6459	$15^+ \rightarrow 14^+$
542.2(2)	0.6(1)	0.90(33)		4635	$(10^-) \rightarrow 9^-$
591.2(2)	0.1(1)			5669	$13^- \rightarrow (12)^+$
614.3(2)	1.7(2)	0.65(12)		4054	$9^- \rightarrow 8^+$
615.8(3)	0.4(1)			4761	$12^+ \rightarrow 10^+$
626.4(2)	1.0(3)			7085	$(16^+) \rightarrow 15^+$
626.9(3)	0.4(1)			5573	$\rightarrow (11)^-$
633.8(1)	1.3(3)			4781	$\rightarrow 10^+$
638.5(2)	0.9(3)			2055	$(4^-) \rightarrow 4^+$
647.8(1)	0.8(1)	0.78(35)		3879	$(8^-) \rightarrow 7^-$
665.5(1)	100.0(67)	1.48(8)	0.73(20)	666	$2^+ \rightarrow 0^+$
681.2(1)	3.3(1)			6135	$\rightarrow 13^{(+)}$
691.2(2)	8.7(5)	0.70(6)	−0.69(38)	5453	$13^+ \rightarrow 12^+$
706.4(2)	2.6(1)			7645	$17^- \rightarrow 16^+$
717.5(1)	2.3(1)			4863	$11^- \rightarrow (10^+)$
726.0(1)	8.7(8)	1.55(16)		3231	$7^- \rightarrow 5^-$
750.6(1)	85.5(60)	1.44(3)	0.61(19)	1416	$4^+ \rightarrow 2^+$
752.4(1)	8.7(7)			6459	$15^+ \rightarrow 14^+$
755.9(1)	0.2(1)			4635	$(10^-) \rightarrow (8^-)$
770.7(1)	1.0(1)	1.55(28)		4863	$11^- \rightarrow 9^-$
773.2(1)	66.1(46)	1.47(3)	0.56(27)	2189	$6^+ \rightarrow 4^+$
786.0(2)	1.9(1)			6704	$15^- \rightarrow 14^{(+)}$
798.6(1)	53.2(36)	1.45(6)	0.61(40)	2988	$8^+ \rightarrow 6^+$
805.8(1)	35.5(16)	1.41(5)	1.00(42)	5669	$13^- \rightarrow 11^-$
809.4(1)	33.9(16)	1.51(5)	0.59(31)	4863	$11^- \rightarrow 9^-$
822.8(2)	5.0(3)	1.64(15)		4054	$9^- \rightarrow 7^-$
853.7(2)	1.6(2)	1.66(27)		4946	$11^- \rightarrow 9^-$
857.4(1)	0.2(1)			3879	$(8^-) \rightarrow 6^{(-)}$
861.8(2)	4.6(4)	1.44(10)		4093	$9^- \rightarrow 7^-$
875.9(1)	27.4(13)	0.77(4)	0.96(19)	4054	$9^- \rightarrow 8^+$
881.1(1)	38.2(26)	1.43(9)	0.60(30)	3869	$10^+ \rightarrow 8^+$
892.4(1)	25.6(18)	1.44(12)	0.98(35)	4761	$12^+ \rightarrow 10^+$

Table 5.2: continued

E_γ(keV)	I_γ(rel.)	R_{ang}	P	E_i(keV)	$I^\pi \rightarrow I^f$
907.9(2)	1.4(2)	0.87(31)		5669	$13^- \rightarrow 12^+$
940.2(1)	36.8(15)	1.42(7)	1.01(33)	7645	$17^- \rightarrow 15^-$
945.0(2)	15.2(9)	1.47(11)	0.81(68)	5707	$14^+ \rightarrow 12^+$
967.0(1)	0.1(1)	1.58(44)		3022	$6^{(-)} \rightarrow (4^-)$
970.0(2)	1.1(1)	1.50(37)		3440	$8^+ \rightarrow 6^+$
988.9(1)	14.2(6)	1.48(12)	1.10(70)	3178	$8^+ \rightarrow 6^+$
992.4(1)	3.2(2)			5918	$14^+ \rightarrow 12^+$
994.3(1)	1.9(2)			4863	$11^- \rightarrow 10^+$
997.9(1)	0.6(1)			6704	$15^- \rightarrow 14^+$
1006.5(1)	1.3(1)			6459	$15^+ \rightarrow 13^+$
1032.0(1)	3.7(3)			7970	$\rightarrow 16^+$
1035.3(1)	35.5(15)	1.46(19)	0.81(35)	6704	$15^- \rightarrow 13^-$
1042.0(1)	1.4(2)			3231	$7^- \rightarrow 6^+$
1053.8(2)	2.0(3)			2470	$6^+ \rightarrow 4^+$
1057.0(2)	3.9(3)	1.42(16)		4926	$12^+ \rightarrow 10^+$
1065.5(2)	1.8(5)			4054	$9^- \rightarrow 8^+$
1071.2(1)	37.1(21)	1.28(7)	0.79(42)	8716	$19^- \rightarrow 17^-$
1089.3(1)	10.9(9)	0.77(9)	1.26(102)	2505	$5^- \rightarrow 4^+$
1156.7(3)	2.0(3)			5918	$14^+ \rightarrow 12^+$
1167.0(1)	2.6(3)			7085	$(16^+) \rightarrow 14^+$
1209.1(2)	4.2(2)	1.52(29)		5078	$(12^+) \rightarrow 10^+$
1231.8(1)	4.8(2)	1.47(36)	1.03(66)	6938	$16^+ \rightarrow 14^+$
1365.0(1)	2.9(1)			8303	$(18^+) \rightarrow 16^+$
1378.8(1)	2.8(3)	1.42(37)		7085	$(16^+) \rightarrow 14^+$
1421.8(3)	3.4(12)			7340	$\rightarrow 14^{(+)}$

The EUROGAM II experiment

Based on the results from the NORDBALL experiment, the level scheme of ^{100}Pd has been studied using the data from a EUROGAM II experiment. The main purpose was to further elaborate on the high-spin part of the level structure. For the analysis of high-spin states in ^{100}Pd a γ-γ-γ coincidence cube was created by demanding that at least one of the γ-rays in an event was in coincidence with any of the transitions with 665, 751, 773, 799, 876, 881, 892, 940, 989 and 1035 keV energies, representing

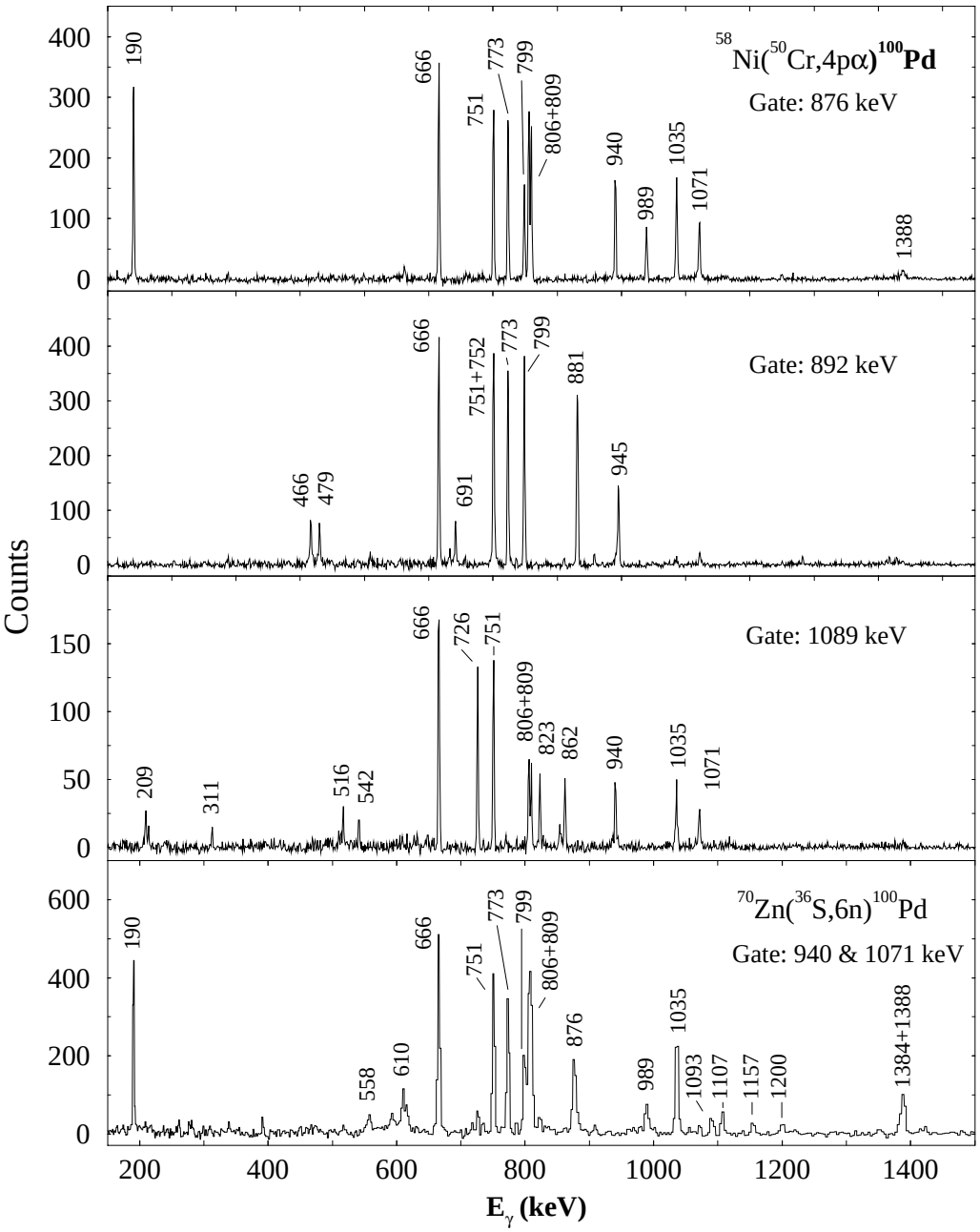

Figure 5.3: Selected γ-ray gated spectra of ^{100}Pd from the ^{58}Ni(^{50}Cr,4p1α) and the ^{70}Zn(^{36}S,6n) reactions.

the strongest pure ^{100}Pd γ-ray transitions. The 3D coincidence analysis was carried out with the help of the LEVIT8R program from the RADWARE package. A γ-ray spectrum obtained from the γ-γ-γ coincidence cube, and gated by the 940 and 1071 keV transitions is shown in the lower part of Fig. 5.3.

To determine the multipolarities of the γ transitions their DCO ratios and linear polarisations were extracted from the experimental data (see Section 2.6.2). The energies, relative intensities, DCO ratios and linear polarisations P for transitions above the 7645 keV level assigned to ^{100}Pd from the ^{70}Zn + ^{36}S reaction are listed in Table 5.3. Linear polarisation values for the stronger γ-rays lying at lower energies are included in Table 5.2.

Table 5.3: Energies, relative intensities, DCO ratios and linear polarisation P for γ-rays assigned to the decay of ^{100}Pd states lying above 9 MeV from the ^{70}Zn+^{36}S reaction. The intensity of the 1071.2 keV transition has been taken as reference.

E_γ(keV)	I_γ(rel.)	R_{DCO}	P	E_i(keV)	$I_i^\pi \rightarrow I_f^\pi$
558.1(1)	7.0(10)			13502	$(24^+)\rightarrow(23^+)$
584.7(2)	4.3(10)			13205	$25^- \rightarrow(24^-)$
609.9(1)	17.4(9)	0.52(6)		11821	$23^- \rightarrow 22^-$
799.3(4)	5.0(20)			12620	$(24^-)\rightarrow 23^-$
1071.2(1)	100.0(55)	1.01(5)	0.79(42)	8716	$19^- \rightarrow 17^-$
1093.0(3)	6.5(17)			16105	
1107.1(1)	26.1(9)	0.66(6)		11211	$22^- \rightarrow 21^-$
1155.6(4)	12.2(21)			9872	
1200.3(2)	15.7(21)	1.02(9)		11650	$22^+ \rightarrow 20^+$
1293.0(1)	8.7(9)			12943	$(23^+)\rightarrow 22^+$
1351.0(1)	6.1(9)			12877	
1384.0(1)	13.0(9)	1.06(19)		13205	$25^- \rightarrow 23^-$
1388.0(1)	65.2(40)	0.91(6)	1.24(48)	10104	$21^- \rightarrow 19^-$
1424.0(1)	7.8(9)			11528	
1511.0(1)	14.8(9)	0.53(16)		15012	$(25)\rightarrow(24^+)$
1581.9(3)	10.5(22)			11686	
1716.9(3)	13.0(22)			11821	$23^- \rightarrow 21^-$
1736.5(4)	17.6(19)	0.65(12)	1.19(115)	10451	$20^+ \rightarrow 19^-$
1752.6(5)	8.6(16)			13439	
1852.0(4)	7.8(10)			13502	$(24^+)\rightarrow 22^+$

Level scheme

The new level scheme of ^{100}Pd, considerably extending the previous ones, is proposed in this work, and is shown in Fig. 5.4. The placement of the levels and γ-ray transitions was strongly supported by the multitude of new γ-rays observed. The construction of the low-energy part of the level scheme was completed mainly on the the basis of the NORDBALL data, while for the higher-energy part data from the EUROGAM II experiment was primarily used. In spite of this, all the transitions placed in the level scheme were seen in both experiments. The spins of the states were deduced from the measured R_{ang} and R_{DCO} ratios. From the polarization analysis the sign of the linear polarisation could be determined for 23 transitions, making it possible to determine also the parity for most of the states. The differences found between our level scheme and previous ones, as well as the new results from this work are discussed below.

The ordering and multipolarities of γ-rays in the ground-state band, given in Refs. [90, 91] have been confirmed. This band has been extended up to an excitation energy of 8303 keV by adding a new, 1365 keV transition on top of the known levels. For this weak γ-ray, it was not possible to deduce any multipolarity, but as its energy corresponds to the continuation of a quasi-rotational sequence, we have tentatively assigned stretched $E2$ character to it.

Above the yrast 3869 keV 10^+ level a non-rotational, less regular level structure has also been observed, as it can be seen on the left hand side of Fig. 5.4. $I^\pi=10^+$ spin-parity value is proposed for its initial level at 4146 keV. The R_{ang}=1.47(14) ratio obtained for the 277 keV transition, allows both stretched quadrupole or non-stretched dipole character. An $E2$ assignment would make the 4146 keV state yrast, which should be much more strongly excited than it is, thus this option was rejected. We proposed spins 13, 14 and 15 for the previously reported [90, 91] levels at 5453, 5918 and 6459 keV, respectively, since the 466, 479, 541 and 691 keV transitions are stretched dipoles according to their R_{ang} ratios. Positive parities have been assigned to these states because of the magnetic characters of the 466, 479 and 691 keV γ-rays deduced from their linear polarisation values. The 5453 keV level decays to the yrast 10^+ state via two more parallel cascades of γ-rays with 375+1209 keV and 526+1057 keV, respectively. The R_{ang} values of the 1057 and 1209 keV transitions indicate stretched quadrupole characters for them, suggesting $I^\pi=12^+$ for the intermediate levels at 4926 and 5078 keV. The spin assignment to the 5453 keV state is also confirmed by the stretched dipole character of the 375 keV γ-ray, outdating the earlier [91] I=12 spin assignment for this level. The 7085 keV level

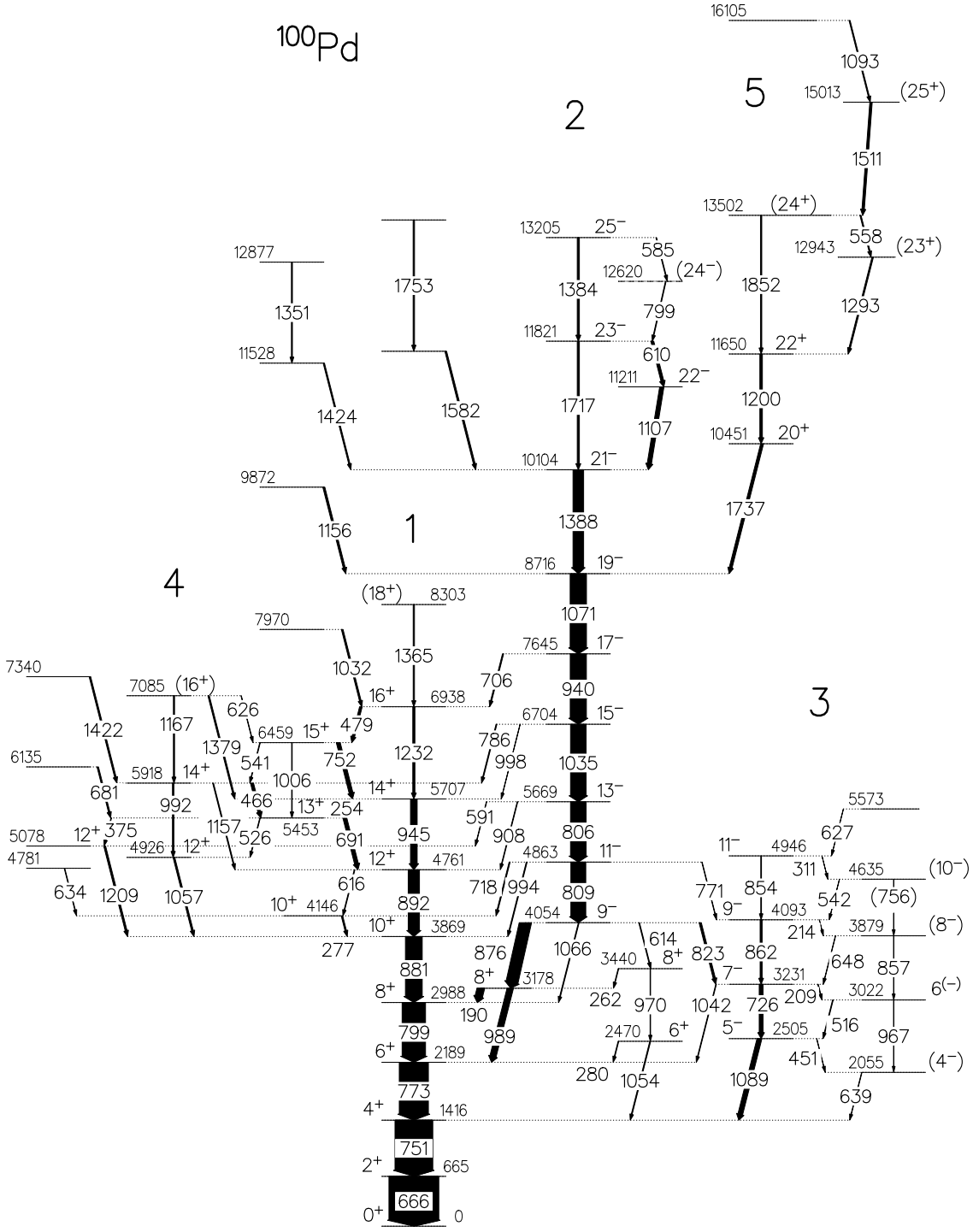

Figure 5.4: Proposed level scheme of ^{100}Pd. The widths of the arrows are proportional to the observed γ-ray intensities. Below the 8716 keV level the intensities have been taken from the NORDBALL experiment, above that they have been taken from the EUROGAM II experiment, normalized with respect to the intensity of the 1071 keV transition.

decays to the 5707 keV 14^+ state via the 1379 keV γ-ray for which R_{ang}=1.42(37) angular correlation ratio was deduced. Because of the large uncertainty of this value tentative (16^+) spin and parity values have been assigned to the 7085 keV state.

The second major band in the level scheme, expected to have negative parity, is linked to the ground state band at the 2189 keV 6^+ and 2988 keV 8^+ states mainly via the 876+989 and 876+190 keV cascades through an intermediate 3178 keV state. The R_{ang}=1.44(7), 1.48(12) and 0.77(4) angular distribution ratios obtained for the 190 keV, 989 keV, and 876 keV γ rays are consistent with the ΔI=0 dipole, stretched quadrupole and stretched dipole nature of these transitions, respectively, in agreement with the previous results. Earlier, on the basis of linear polarisation measurements the 989 keV γ ray was assigned M2 multipolarity [90]. According to our linear polarisation data, the P=1.10 value for the 989 keV transition means that it has $E2$ character. Similarily we obtained $M1$ multipolarity for the non-stretched 190 keV transition (P=1.37) and $E1$ for the 876 keV γ-ray (P=0.96). The multipolarities determined this way unambiguously indicate that the 3178 keV spin 8 state has positive parity, and the 4054 keV bandhead has 9^- spin and parity.

Another connection between the two bands could be established via the 2470 and 3440 keV states. The 614+970+1054 keV cascade connects the 9^- band head to the 1416 keV 4^+ state. The spin difference of 5 units can be overcome by combining two stretched quadrupoles with a ΔI=1 transition. Since the R_{ang}=0.65(12) ratio for the 614 keV transition excludes the ΔI=2 possibility, spin 6 was assigned to the 2470 keV level and spin 8 for the 3440 keV level.

The order of levels in the negative-parity band up to 8716 keV is based on the observation of several linking transitions between the levels of this and of the ground-state band, namely the 706, 998, 908 and 994 keV lines. Because of the known spins and parities of the initial and final states, all the above mentioned linking transitions are of stretched $E1$ character, as well as the 718, 591 and 786 keV transitions connecting the negative-parity band with other positive-parity states.

Above the 8716 keV level, we observed several branches of shorter or longer γ-ray cascades. Multipolarities of the most intense transitions could be determined on the basis of our DCO and linear polarisation results. $E2$ multipolarities were deduced for the 1384 and 1388 keV γ-rays, and stretched $M1$ multipolarities for the 610 and 1107 keV γ-rays. For the 1717 keV transition E2 multipolarity is assigned, since it connects states with ΔI=2 spin difference. Accordingly, I^π=21^-, 22^-, 23^- and 25^- spin-parity values were assigned to the states at 10104, 11211, 11821 and 13205 keV, respectively. A pair of transitions with 799 and 585 keV is placed between the 13205

keV 25^- and the 11821 keV 23^- states. Spin (24^-) was assigned to the intermediate state, the energy of which is uncertain, as the order of these transitions could not be determined.

The other longer branch is connected to the 8716 keV 19^- state via the 1737 keV transition to which stretched $E1$ multipolarity was assigned from its DCO and linear polarisation values. Consequently, a positive parity structure is expected to be built on the 10451 keV level having $I^\pi=20^+$ spin and parity. The R_{DCO}=1.02(9) ratio obtained for the 1200 keV γ-ray, suggests a stretched quadrupole character for it, resulting in $I^\pi=22^+$ spin and parity for the 11650 keV level. Since the 1852 keV transition is overcrossing the 1293+558 keV γ sequence, stretched E2 multipolarity is assumed for it and stretched M1 for the overcrossed transitions, leading to $I^\pi=(23^+)$ and (24^+) for the 12943 and 13502 keV states, respectively. Due to the dipole nature of the 1511 keV transition, (25^+) spin and parity was assigned to the 15013 keV state. The transitions of the two shorter branches feeding the 10104 keV level were too weak to determine their DCO ratios, thus no spins could be assigned to the corresponding new high-energy levels.

A well developed low-spin band structure connected to the previously known 5^- level at 2505 keV was revealed. The stretched quadrupole nature of the stronger 726, 862, 823 and 771 keV transitions confirm the 5, 7 and 9 spin assignments for the 2505 3231 and 4093 keV states, respectively. The spin 5 value and the negative parity of the bandhead is confirmed by the positive P value of the stretched dipole 1089 keV transition. The new 854 keV γ line on the top of this sequence is a stretched quadrupole transition on the basis of its R_{ang} ratio, therefore $I^\pi=11^-$ is proposed for the 4946 keV level. Each state of this short band is connected via a pair of presumably dipole transitions to the members of the neighbouring weakly excited structure. The dipole nature of the 209 keV transition was determined from its R_{ang} ratio, suggesting $6^{(-)}$ spin and parity for the 3022 keV state. The lowest four states of this new structure are connected through crossover probably E2 transitions, thus, (4^-), (8^-) and (10^-) spins and parities were assumed for the 2055, 3879 and 4635 keV states. These assignments are in agreement with the R_{ang} ratios obtained for some of the weak transitions within this structure, but they have too high uncertainty to deduce a clear conclusion.

5.3 Discussion

5.3.1 The ^{98}Pd nucleus

The structure of the positive-parity yrast states of ^{98}Pd has been theoretically interpreted by Sau *et al* [89] by considering the coupling of four proton holes below ^{100}Sn to two neutron particles above ^{100}Sn, in a highly-truncated shell model space. We shall base our discussion of the newly observed structures in ^{98}Pd (see Fig. 5.2, on the shell-model calculations of Ref. [89], on the systematics of heavier even-A Pd isotopes [88, 90, 93], and on qualitative arguments.

The low-lying positive-parity yrast states of ^{98}Pd up to 6^+ have been satisfactory described in terms of the $\nu d_{5/2}g_{7/2}$ and the $\nu g^2_{7/2}$ configurations. At and above the 8^+ state $g^{-4}_{9/2}$ proton excitations are predicted to have significant contribution. If we follow the evolution of the positive-parity ground-state band up to higher spins we may note that at the 8508 keV level with $I^\pi = (18^+)$ it has an abrupt end via the 1160 keV transition (although this band extends to higher excitation energies via other parallel branches). In ^{100}Pd (see next Section) we observe a similar behaviour for the ground-state band that also ends at spin 18^+. However, the proposed configuration of this highest energy state in ^{98}Pd must be different from that of ^{100}Pd, because there are only two valence neutrons in this nucleus. Now, note that 18^+ state is the maximally aligned state for the $[\nu(g_{7/2}, d_{5/2})^2\pi g^4_{9/2}]_{18^+}$ and $[\nu g^2_{7/2}\pi g^4_{9/2}]_{18^+}$ configurations. This qualitative reasoning just indicates that we may be in presence of band termination in ^{98}Pd. More precise answer could be given only on the basis of shell model calculations.

The observed negativ-parity cascade extending to a maximum spin of $11\hbar$ most likely corresponds to the sequence of the proton 4-quasiparticle states built on the $\pi g^{-3}_{9/2}\pi p^{-1}_{1/2}$ configuration. The same structure has been tentatively observed in ^{100}Pd in this work (see Fig. 5.4) and in heavier even Pd isotopes [93]. Since the energy of the 5^- state, serving as bandhead, shows very small variance with decreasing neutron number, it is reasonable to assume that there is no contribution from neutron excitations to this state. The model space for negative parity-states, using the $\pi g^{-3}_{9/2}\pi p^{-1}_{1/2}$ configuration is exhausted at 11^-, therefore a new negative parity state of the same or of higher spin must either involve the $\nu h_{11/2}$ orbital or be a 6-quasiparticle state corresponding to the first 2^+ state (neutron excitation) in ^{102}Sn coupled to the proton 4-quasiparticle 11^- state. The most plausible interpretation, considering the excitation energy, seems to be that of a 6-quasiparticle state involving the $\nu d_{5/2}$ configuration. The deduced energy gap of about 1300 keV between

the 4-quasiparticle and 6-quasiparticle states is also reasonable, taking into account that the 2^+ state in ^{102}Sn was recently measured to lie at an excitation energy of 1472 keV [94].

For the sequence of positive-parity states formed by the 979, 434 and 454 keV γ-ray transitions, we have not found any definitive interpretation. The experimental observation that the 979 keV transition is probably a mixed M1/E2 transtion would e.g. be possible if the configuration of the 9^+ state were the yrast 8^+ state coupled to a 2^+ excitation.

5.3.2 The ^{100}Pd nucleus

Collectivity, alignment and band termination

At a first glance, ^{100}Pd is quite similar to its heavier neighbours. Similarly to ^{102}Pd [24], at low spin the yrast states form a rotational-like band structure with positive parity and α=0 signature. This band extends over several transitions up to spin 18, while many other positive-parity states, linked with γ-transitions to each-other and to the yrast band evolve in the spin 10 - 16 region. Also in analogy with the level scheme of ^{102}Pd three negative-parity bands appear at low and intermediate spins. However, in contrast with the case of ^{102}Pd, only one of them is seen above spin 12. This band, which becomes yrast above spin 17, is strongly populated up to the 21^- state above which the population intensity spreads out on several decay-paths. The feeding of the two other negative parity bands are considerably weaker.

To gain a better understanding of the structure of ^{100}Pd, we have performed cranked Woods-Saxon Strutinsky calculations (see Section 3.3). The energy in the rotating frame of reference (the total Routhian) was minimized with respect to the quadrupole shape parameters γ and β_2 with hexadecapole (β_4) variation. Pairing correlations were treated by means of the Lipkin-Nogami method and contained both monopole and quadrupole components. More details on the method can be found, e.g. in Ref. [96]. To investigate the possibility of octupole correlations, we also minimized the Total Routhian Surface (TRS) with respect to β_3, β_2, with hexadecapole variation, but restricting to axial symmetric shapes.

To enable assignment of TRS configurations to the experimentally observed bands, the experimental excitation energies of the well developed bands relative to a rigid-rotor reference were compared with the relative energies calculated for the quasiparticle vacuum (vac) and for the lowest-energy two-quasiparticle configurations, as shown in Fig. 5.5. There is a good qualitative agreement between the

observed and calculated curves in their relative positions, in their slopes at high spins, and in the place of the crossing between bands 1 and 2. These agreements corroborate the assignment of the TRS configurations to the observed bands. To guide the eyes, we use the same symbols in Fig. 5.5 for the observed bands and for the TRS configurations assigned to them.

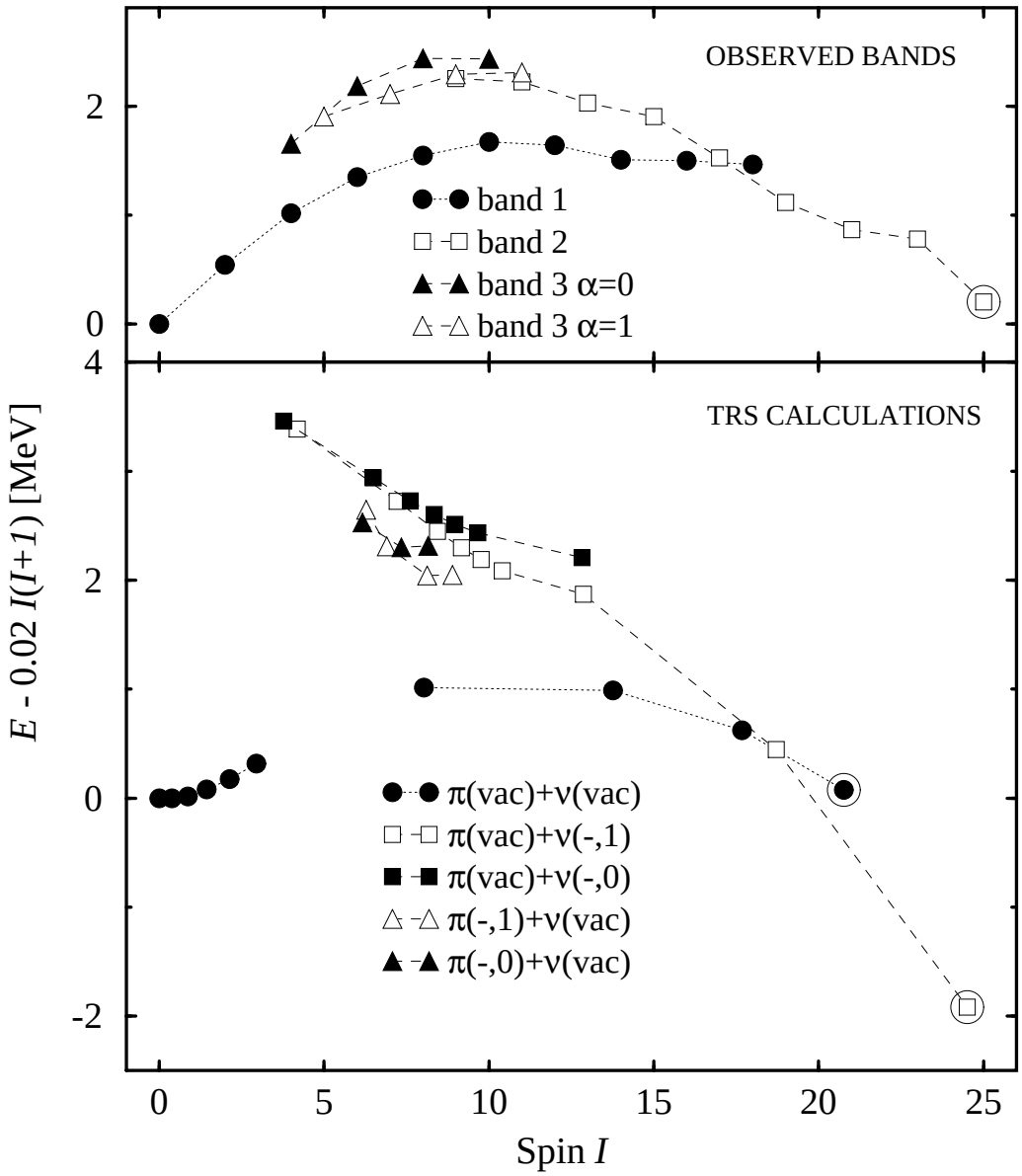

Figure 5.5: Comparison of the experimental (top) and theoretical (bottom) deviations of the band state energies from that predicted by the rotational model for a rigid body. Theoretical deviations are calculated for the region of band terminations.

In order to reveal the quasiparticle structure of the TRS configurations shown in Fig. 5.5 we have plotted the Woods-Saxon cranked shell model Routhians of the low-lying quasiparticle states as a function of the rotational frequency $\hbar\omega$ (see Fig. 5.6). In these calculations we assumed a nuclear shape characterized by β_2=0.14 and γ=0, which are typical values for the lowest energy bands in the TRS calculations. According to Fig. 5.6 the lowest energy positive-parity quasineutron states correspond to the [420]1/2 and the [422]3/2 Nilsson orbitals originating from the $(d_{5/2}, g_{7/2})$ subshell, while the lowest negative-parity quasineutron states are the [550]1/2 orbitals originating from the $h_{11/2}$ subshell. On the proton side the lowest lying positive and negative parity orbitals correspond to the [413]7/2 $g_{9/2}$ and to the [301]1/2 $p_{1/2}$ states, respectively. The [413]7/2 proton orbitals show a crossing at $\hbar\omega \approx$0.4 MeV which corresponds to the alignment of a $g_{9/2}$ proton pair. This is the first (lowest frequency) predicted alignment in this nucleus. The alignment of the [550]1/2 neutrons takes place well above this frequency, at $\hbar\omega \approx$0.55 MeV according to the calculations.

It can be seen from Fig. 5.5 that the experimental positive-parity ground-state band (band 1) with α=0 signature is yrast up to spin 17, where it is crossed by the negative-parity α=1 signature band (band 2). Above the crossing spin, band 1 is seen only up to spin 18 while band 2 is observed up to spin 25. The calculated lowest-energy $\pi(\mathrm{vac})\otimes\nu(\mathrm{vac})$ configuration and the $\pi(\mathrm{vac})\otimes\nu(-,1)$ configuration show very similar behaviour. The $\pi(\mathrm{vac})\otimes\nu(\mathrm{vac})$ configuration has positive parity and α=0 signature, and it is calculated to be yrast up to spin $\sim$19 where it is crossed by the negative-parity α=1 signature $\pi(\mathrm{vac})\otimes\nu(-,1)$ configuration. These configurations are predicted to terminate at spins 22 and 25, respectively. According to these similarities between the behaviour of the two observed and the two calculated bands we assign the $\pi(\mathrm{vac})\otimes\nu(\mathrm{vac})$ TRS configuration to band 1 and the $\pi(\mathrm{vac})\otimes\nu(-,1)$ configuration to band 2. These assignments are also supported by the similar slopes of the experimental and the corresponding calculated excitation energy curves for the two bands.

Based on the above assignment, the ground-state band does not contain quasiparticle excitations at low rotational frequencies. At $\hbar\omega \approx 0.4$ MeV an alignment of a pair of $g_{9/2}$ protons takes place. As shown in panel (a) of Fig. 5.7, the frequency of this alignment is in good agreement with that of the experimental alignment. Above this abrupt alignment the TRS calculations predict the gradual alignments of the $(d_{5/2}, g_{7/2})$ neutrons and the second pair of $g_{9/2}$ protons, which drive the shape of the nucleus towards smaller β_2 and larger γ values. Due to these alignments the

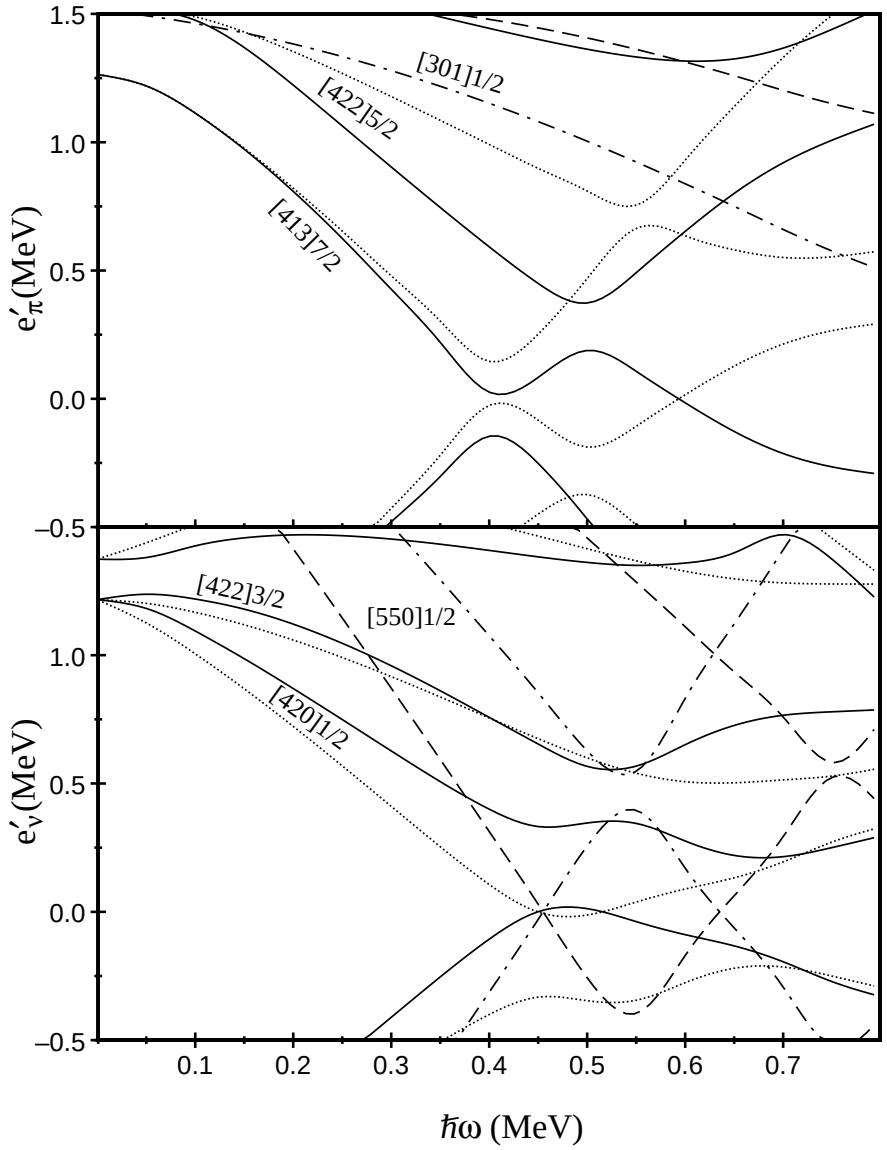

Figure 5.6: Cranked Woods-Saxon quasiparticle Routhians for protons (top) and neutrons (bottom) calculated for ^{100}Pd as functions of rotational frequency $\hbar\omega$. Solid (dashed) and dotted (dashed-dotted) lines correspond to positive (negative) parity states with signature $\alpha = +1/2$ and $\alpha = -1/2$ ($\alpha = -1/2$ and $\alpha = +1/2$), respectively. The labels indicate the asymptotic quantum numbers of the Nilsson states to which the Routians correspond at $\hbar\omega = 0$.

band looses its collective nature and the single-particle character of the excitation becomes dominant. At around spin 22 the calculated β_2 value is close to zero and the calculated γ value reaches 60° corresponding to non-collective spherical shape characteristic for band-terminating states, where the total spin of the nucleus is built up solely from the spin of the aligned single-particles.

This spin 22 value is the maximal spin which can be built from the four $g_{9/2}$ proton holes and four $(d_{5/2}, g_{7/2})$ neutrons. The highest observed spin in this band is 18 (the state at 8303 keV), which is below the expected terminating spin by four units. As for the structure of this state, it is highly probable that it corresponds to the maximally aligned $\nu(g_{7/2}, d_{5/2})^4 \pi g_{9/2}^2$ configuration as the break-up of the second proton pair takes place around the maximal available angular momentum of the smaller subspace.

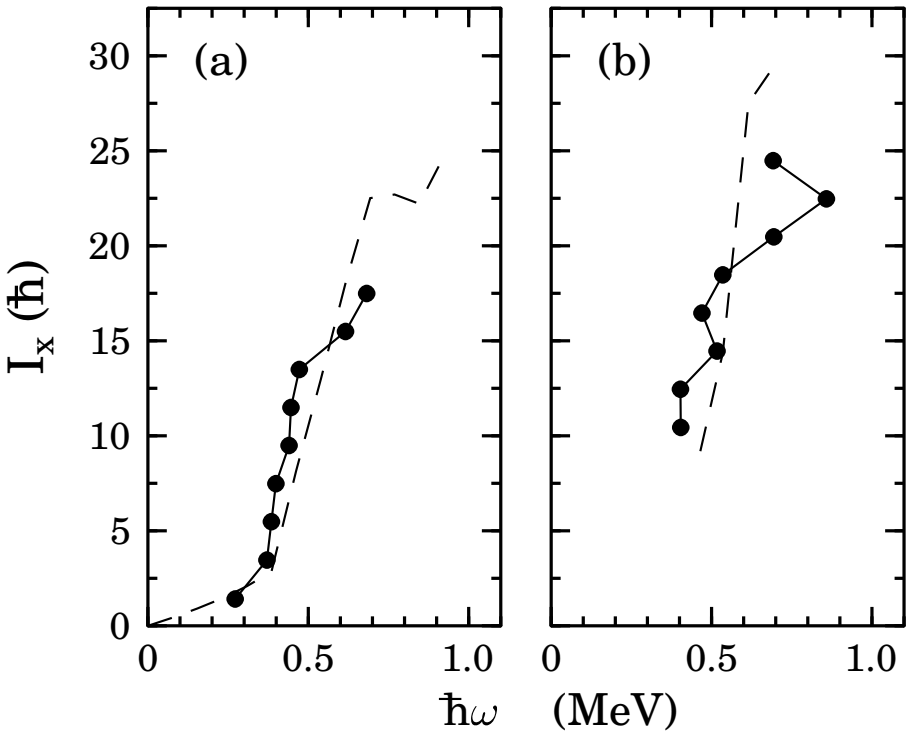

Figure 5.7: I_x versus rotational frequency for the ground state band (a) and for the negative parity side-band (b) of ^{100}Pd (solid lines). The theoretical values (dashed line) are taken from the TRS calculation.

Band 2 corresponds to the $\pi(\text{vac}) \otimes \nu(-,1)$ TRS configuration. At low frequency, according to Fig. 5.6, this configuration is built up from the two-quasineutron excitation in which the $\alpha = -1/2$ signature branch of the [420]1/2 $(d_{5/2}, g_{7/2})$ orbital is combined with the $\alpha = -1/2$ signature branch of the [550]1/2 $h_{11/2}$ orbital. According to the TRS calculations, this configuration, similarly to the case of the ground-state band, also undergoes the first $g_{9/2}$ proton alignment, the gradual $(d_{5/2}, g_{7/2})$ neutron alignment and the second $g_{9/2}$ proton alignment. The observed and calculated alignments of this band are shown in panel (b) of Fig. 5.7.

At spin 25 the band is predicted to reach the maximum angular momentum which can be built from the single-particle spins of the four $g_{9/2}$ protons and five

$(d_{5/2}, g_{7/2})$ neutrons plus one $h_{11/2}$ neutron. At this spin the calculated shape is again characterised by small β_2 value and γ=60°. In the experiment a strong E2 cascade goes up to spin 21 which, similarly to the case of the 18^+ state in band 1, could correspond to the $\nu(g_{7/2}, d_{5/2})^3 h_{11/2} \pi g_{9/2}^2$ configuration combining the maximally aligned neutron configuration with one aligned proton pair. The presence of the Δ=1 side structure above that state may result from the competing $g_{7/2}$ and $d_{5/2}$ neutron configurations that can couple to similar angular momentum states. According to the good agreement between the behaviour of the observed band and the calculated configuration, the highest energy state of band 2 at 13205 keV with spin 25 corresponds probably to the $[\nu(g_{7/2}, d_{5/2})^3 h_{11/2} \pi g_{9/2}^4)]_{25^-}$ terminating state. This assignment is also supported by the fact that, in spite of the relatively strong feeding of this state, no γ-transitions could be found to the 25^- state.

The configuration of the negative-parity coupled band (band 3) cannot be determined unambiguously from the present data. Negative parity coupled bands can be formed either by the combination of the $\alpha = +1/2$ signature branch of the [301]1/2 $p_{1/2}$ and both signatures of the [413]7/2 $g_{9/2}$ proton orbitals or by the combination of the $\alpha = -1/2$ signature branch of the [550]1/2 $h_{11/2}$ and the two signatures of the [422]3/2 $g_{7/2}$ neutron orbitals. As seen in Fig. 5.5, TRS calculations predict the two-quasiproton configuration at an excitation energy close to the assigned configuration of band 1 in accordance with the experimental findings. This assignment is favoured for very small deformation because in that case the proton $p_{1/2}$ quasiparticle energy is closer to the Fermi level than the neutron $h_{11/2}$ quasiparticle energy. However, neither the calculated rotational frequency nor the calculated spin ranges agree satisfactorily with the observed frequency and spin ranges for band 3. Another argument against this assignment is the observed abrupt alignment of the band at the $\hbar\omega$=0.4 MeV rotational frequency. According to Fig. 5.6 this frequency corresponds to the first $g_{9/2}$ proton alignment which is blocked for the above configuration. We note here that Fig. 5.6 is calculated for β_2=0.14, but for smaller β_2 values the calculated alignment frequencies would increase. Alternatively, similarly to the case of the negative-parity bands in ^{102}Pd [24], band 3 could correspond to the above mentioned $\nu(h_{11/2}, g_{7/2})$ two-quasineutron configuration, which assignment would be supported by the observed alignment, too. This configuration has the same TRS configuration as assigned to band 2 and to its signature partner $\pi(\mathrm{vac}) \otimes \nu(-, 0)$. Note, however, that we calculated only the lowest-energy bands for each TRS configuration, therefore this 'higher-energy' configuration is not described in our calculations.

The strongly mixed structures in the spin $10-16$ region on the left-hand side of Fig. 5.4 may easily correspond to similar configuration than that of band 1 in the same spin region, i.e. $\nu(g_{7/2},d_{5/2})^4$ coupled to an aligned proton pair, but with different distribution of the neutrons in the $\nu(g_{7/2},d_{5/2})$ subshell. Consequently, these configurations would correspond to 'higher-energy' bands of the same TRS configuration, but, as mentioned above, they are not described in the present calculations. This scenario is, however, qualitatively supported by the experimental observation of many cross-linking transitions among these levels and those of band 1 and among these levels themselves. In analogy with the level scheme of ^{102}Pd, we propose that band 4 corresponds to the configuration containing an aligned pair of $h_{11/2}$ neutrons.

The high-energy high-spin band (band 5) probably corresponds to four- or more-quasiparticle excitation. From the present data, however, one cannot unambiguously decide which of the positive-parity configurations are observed. For positive parity, the maximal spins available in the subspace with one $h_{11/2}$ neutron can be achieved at the $[\nu(g_{7/2}^3h_{11/2})\pi(g_{9/2}^3p_{1/2})]_{24^+}$ and the $[\nu(g_{7/2}^2d_{5/2}h_{11/2})\pi(g_{9/2}^3p_{1/2})]_{25^+}$ configurations. The observed 13502 keV and 15013 keV states could correspond to these configurations. However, the terminating state of the $\nu(g_{7/2}^2d_{5/2}h_{11/2})\pi(g_{9/2}^3p_{1/2})$ configuration is close in energy to the terminating state of the $\nu(g_{7/2}^2h_{11/2}^2)\pi g_{9/2}^4$ configuration which terminates at $I=28\hbar$, so the observed highest-spin states of band 5 could correspond to this other configuration, either. Note, that octupole correlations, will mix the two different configurations.

Recent studies on high-spin band terminations in $A\approx100$ Pd, Rh and Ru nuclei [24, 28, 95] have shown that configuration dependent cranked Nilsson-Strutinsky calculations reproduce reasonably well the relative positions and terminating spins of different bands observed at high spin ($\geq 15-20\hbar$), where the pairing interaction is assumed to play a minor role [97]. We calculated the terminating states with the cranked Woods-Saxon potential. Here, pairing correlations are treated fully self-consistently, implying that the interaction with states above the terminating state is taken into account. The slope of the positive and negative parity branches are reproduced rather well as is the crossing between the two bands, giving confidence to the position of the $h_{11/2}$ neutron shell. However, the terminating $I^\pi=25^-\hbar$ state is lower in energy in the calculation than in the experiment. The reason for this discrepancy needs further investigation. It may reflect the fact that the pairing strength is not determined appropriatly, which is reflected especially in states of high seniority [98].

Octupole correlations

The study of octupole correlations in atomic nuclei is an interesting subject, since the question of stable and dynamic deformations is always under debate and in addition, strong octupole correlations are observed only in selected regions of the nuclear chart [99]. In the very light Xe-Ba region, strong octupole effects have been predicted, related to the fact that the Fermi surface is between the $h_{11/2}$ and $d_{5/2}$ configuration for proton and neutron numbers N=Z=56(54) [3].

The fingerprint of the octupole vibrations would be a low-lying 3^- state, which is clearly absent in our level scheme. However, as discussed in Ref. [100], the excitation of $h_{11/2}$ neutrons may induce some octupole correlations, related to the fact that the deformed $g_{7/2}$ Woods-Saxon orbit has a strong $d_{5/2}$ component and hence, the excitations into the $h_{11/2}$ orbit are favoured by coupling to the octupole phonon. Strong ΔI=1 E1 transitions may serve as indicators of octupole collectivity.

The E1 operator connects states from two different shells, implying that they are always very hindered. The actual single-particle hindrance factor can be obtained from the known lifetimes of single-particle E1 transitions in the region. In our case, the single proton E1 transitions are hindered by a factor of 1–3$\times10^{-6}$ in odd Ag and In isotopes, while the single neutron transitions are hindered by a factor of 1–2$\times10^{-5}$ in odd Cd isotopes. These are the numbers compared to which the enhancement can be deduced.

Although we have not measured the lifetimes of the states, the B(E1) values can be estimated for the E1 transitions linking the negative and the positive parity states. Taking the quadrupole deformation for the negative parity band from the TRS-calculations, the lifetime of its members can be calculated. The reduced E1 transition probabilities can then be obtained from the I_γ(E1)/I_γ(E2) branching ratios using the following expression:

$$\frac{B(E1;I\rightarrow I-1)}{B(E2;I\rightarrow I-2)} = \frac{1}{1.3\times10^6}\frac{E_\gamma^5(E2)}{E_\gamma^3(E1)}\frac{I_\gamma(E1)}{I_\gamma(E2)}\left(\mathrm{fm}^{-2}\right), \qquad (5.1)$$

where the energies of the γ-rays are given in MeV. The B(E2) values were calculated as

$$B(E2;I\rightarrow I-2) = \frac{5}{16\pi}Q_0^2|<J_iK20|J_fK>|^2, \qquad (5.2)$$

where the K=1 and Q_0=2 eb values obtained from the prediction of the TRS for the negative parity band were used. The deduced B(E1) probabilities are given in Table 5.4.

It can be seen from Table 5.4 that at the bottom of the band the hindrance factors are a few times 10^{-5}, while for spin 17^- it can reach 10^{-4}. As the negative

Table 5.4: The reduced E1 transition probabilities in ^{100}Pd estimated from branching ratios compared to known values in ^{117,119}Cd.

Nucleus	E_γ(keV)	$I_i^\pi \rightarrow I_f^\pi$	B(E1)(W.u.)
^{100}Pd	994	$11^- \rightarrow 10^+$	$1.5(3)\times10^{-5}$
	718		$3.9(3)\times10^{-5}$
	908	$13^- \rightarrow 12^+$	$1.4(3)\times10^{-5}$
	591		$5.1(4)\times10^{-5}$
	998	$15^- \rightarrow 14^+$	$1.6(4)\times10^{-5}$
	786		$3.2(4)\times10^{-5}$
	706	$17^- \rightarrow 16^+$	$1.2(2)\times10^{-4}$
^{117}Cd	205		$2.0(2)\times10^{-5}$
	220		$9.4(9)\times10^{-6}$
^{119}Cd	199		$1.1(1)\times10^{-5}$
	213		$9.4(2)\times10^{-6}$

parity band is based on the $\nu g_{7/2}h_{11/2}$ configuration, these values are to be compared with those obtained for the Cd isotopes. It means that the observed E1 transitions are only slightly enhanced, if they are enhanced at all, at the bottom of the band, while they may be enhanced up to a factor of 10 already at the middle of the band. This low value of enhancement means that there is certainly no permanent octupole deformation in ^{100}Pd, at low spins, but at higher spins some octupole collectivity may develop. The development of octupole softness with increasing spin can be followed in Fig. 5.8, where the $\beta_2 - \beta_3 - \beta_4$ total Routhian surfaces are shown. As discussed previously, the ground state band starts out at a rather modest quadrupole deformation and in the process of proton alignment it changes the shape of the nucleus to become spherical. This shape change is associated with an excursion into the β_3 deformation plane, shown in Fig. 5.8. This β_3 softness reflects the mixing of the $h_{11/2}$ and $d_{5/2}$ neutron configurations which may cause the enhancement of the E1 transitions. Note that the presence of octupole correlations will alter also the possible terminating states scheme.

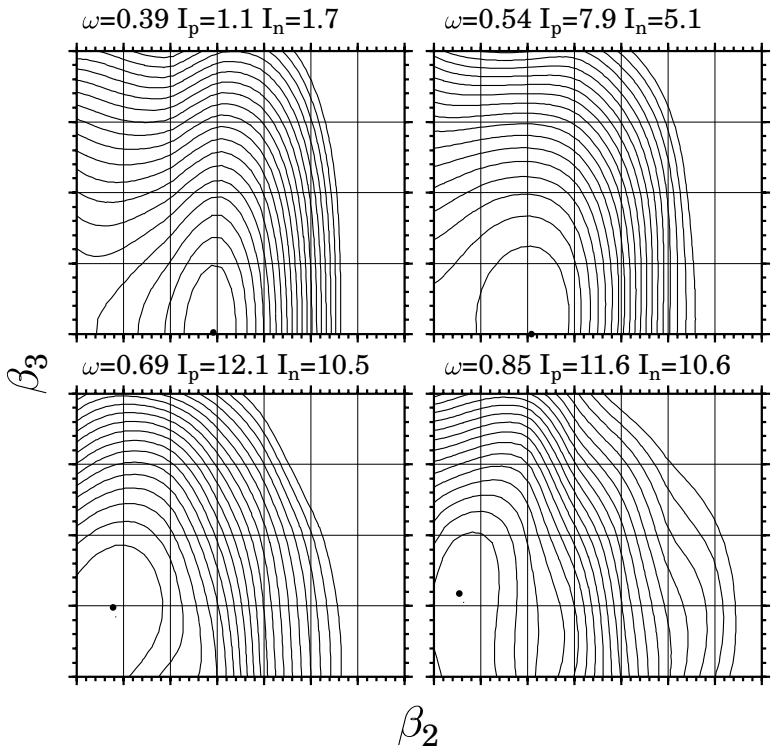

Figure 5.8: Development of octupole collectivity for the ground-state band calculated by use of Total Routhian Surface method.

Chapter 6

Summary

In this thesis I have studied the structure of the very neutron deficient ^{108,109,110}Te and ^{98,100}Pd nuclei by means of in-beam γ-ray spectroscopy. The obtained experimental results have been interpreted in the framework of various nuclear models. As a result, our experimental and theoretical knowledge of these nuclei has been considerably enhanced.

In addition, it has been proved that in-beam γ-ray spectroscopy based on large γ-detector arrays in combination with ancillary detectors, is one of the most powerful tools today to experimentally study the structure of atomic nuclei far from the β-stability line.

In the enourmous experimental work I was aided by a large group of physicist, taking part in the international research program. I have played a major role in the achievement of the results which form part of this thesis, namely: the preparation and analysis of the experimental data, the evaluation of the experimental results, and their theoretical interpretation.

In what follows, I give a summary of the main results obtained for each nuclei studied in this thesis.

6.1 Neutron deficient Te nuclei

The neutron deficient ^{108,109,110}Te nuclei were studied in-beam using the ^{54}Fe + ^{58}Ni reaction at 270 MeV beam energy. From the compound nucleus ^{112}Xe, they originated by the evaporation of two protons and the emission of two-, one- or no neutrons, respectively. The detection of the evaporated particles and the emitted γ-rays was performed with the NORDBALL detector array, equipped with 15 Compton-suppressed HPGe detectors, a Si ball of 21 ΔE-type charged-particle detectors, a

neutron wall of 11 liquid scintillators, and an inner ball of 30 BaF_2 crystals. The obtained experimental data was sorted into particle-gated E_γ-E_γ matrices, from which the level schemes of the studied nuclei were deduced, mainly on the basis of the coincidence relations, and γ-ray energy and intensity balance. The spin values of the excited states were inferred using a simplified γ-γ angular correlation analysis, which is sensitive to the angular momentum transferred by the γ-rays.

The present work constitutes the first in-beam study of these nuclei. No excited states of ^{108,109}Te were known prior to our work and for ^{110}Te only the energy of the $2^+ \rightarrow 0^+$ ground- state transition had been deduced from the α-decay of ^{114}Xe. The new experimental results obtained in this work for ^{108,109,110}Te are summarised below:

- Ten new γ-ray transitions have been assigned to ^{108}Te, and the level scheme of this nucleus has been constructed up to spin $8\hbar$. The $I^\pi = 2^+$ value for the first excited state in ^{108}Te is well established, but for the other states the spin assignments are only tentative, based on the systematics of heavier Te isotopes.

- The proposed level scheme of ^{110}Te was extended up to $I^\pi = (21^-)$ and 8.5 MeV in excitation energy. Energies, relative intensities and spin values were deduced from the experimental data. The low-lying states of the ground-state band formed a positive-parity sequence up to spin 8^+. Above that level, a cascade of stretched quadrupole transitions has been observed on a band head, which was suggested to have $I^\pi = 9^{(-)}$. At spin about $17\hbar$ a band crossing (backbend) was observed.

- The low-lying 2^+, 4^+, 6^+ yrast states of ^{108,110}Te were suggested to be mainly vibrational phonon excitations. The negative-parity band in ^{110}Te was interpreted as built on the $\nu g_{7/2} \otimes \nu h_{11/2}$ two-quasiparticle configuration. Calculations performed in the framework of the cranked shell model gave a quadrupole deformation $\beta_2 \approx 0.15$ for the ground state of ^{110}Te. The model explained the observed crossing as the alignment of two $h_{11/2}$ neutrons, but failed to predict the crossing frequency. Since only quadrupole and hexadecapole deformation parameters were included in the calculations, this was interpreted as an indication that other degrees of freedom, like octupole correlations could play an important role in high-spin excitations of light Te nuclei.

- A new level scheme of ^{109}Te has been obtained extending up to 6716 keV in

excitation energy and containing about 30 new γ-ray transitions. Energies, relative intensities and multipolarities have been deduced for these transitions. A strongly fed, negative-parity band has been observed up to a well established spin 35/2, with states connected by stretched E2 transitions. A weakly populated positive-parity band was also observed up to spin 15/2.

- The structure of ^{109}Te was discussed in the particle-vibration limit of the interacting boson-fermion model (IBFM). According to the calculations the ground state is the $d_{5/2}$ quasi-neutron state, while the positive-parity excited states involved the members of the $\nu d_{5/2} \otimes 2^+$ and $\nu g_{7/2} \otimes 2^+$, 4^+, 6^+ mutiplets. The negative-parity band was interpreted as the coupling of the $h_{11/2}$ neutron states to the yrast states of the ^{108}Te core. Above the IBFM spin limit of $27/2\hbar$, the experimentally observed increase in angular momentum at $\hbar\omega \approx 0.45$ MeV could not be totally reproduced by the alignment of $g_{7/2}$ neutrons in cranked Strutinsky calculations. The discrepance was tentatively explained as due to vibration-rotation coupling.

6.2 Neutron deficient Pd nuclei

High-spin states of the neutron deficient ^{98}Pd and ^{100}Pd isotopes were studied with the NORDBALL array using the reaction ^{50}Cr + ^{58}Ni at a beam energy of 261 MeV. For the analysis of the high-spin part of ^{100}Pd, data from the reaction ^{70}Zn(^{36}S,6n) at 130 MeV beam energy, obtained with the EUROGAM II spectrometer was also used. Particle-gated E_γ-E_γ matrices from the NORDBALL data, and a γ-gated E_γ-E_γ-E_γ cube from the EUROGAM II experiment were created to construct the level schemes of the studied nuclei. For spin and parity assignments γ-γ angular correlation data, and in the case of ^{100}Pd, DCO ration and linear polarisation data were used.

In this work, the previously known level schemes of ^{98}Pd and ^{100}Pd have been considerably extended to high-spin, and new structures has been observed for the first time in these nuclei. The new experimental results obtained for ^{98,100}Pd are summarised below:

- About 40 new γ-ray transitions have been assigned to ^{98}Pd, extending its previous level scheme to 10.9 MeV. Energies, relative intensities and the angular momentum, taken away by the γ-rays have been deduced from the experimental data. Our analysis confirmed the previous results for the positive-parity even-spin band up to spin $14\hbar$, above that level a modification and extension of

the band was proposed. A maximum spin of $18\hbar$ and positive-parity was tentatively assigned to a level at 8508 keV. Based on qualitative arguments, this level was interpreted as a mixture of the $[\pi g_{9/2}^{-4}\nu g_{7/2}^{2}]_{18^+}$ and $[\pi g_{9/2}^{-4}\nu g_{7/2}d_{5/2}]_{18^+}$ terminating configurations. For the first time we have observed a sequence of negative-parity states starting at the 5^- level at 2620 keV. This structure up to $I^\pi = 11^-$ has been interpreted as the 4-quasiparticle states of the $\pi g_{9/2}^{-3}\pi p_{1/2}^{-1}$ configuration. For the negative-parity state, observed above spin $11\hbar$, it is suggested to be a 6-quasiparticle state, corresponding to the first 2^+ state (neutron excitation) in ^{102}Sn coupled to the proton 4-quasiparticle configuration.

- About 50 new γ-ray transitions have been assigned to ^{100}Pd, extending its level scheme up to $\sim$16 MeV in excitation energy and $\sim 25\hbar$ of angular momentum. Previous spin and parity assignments have been reviewed on the basis of γ-ray angular correlation, DCO ratio and linear polarisation data. It has been found that a level at 4054 keV in ^{100}Pd has $I^\pi = 9^-$, contradicting the assignment of 8^- from a previous study. A negative-parity odd-spin sequence built on this state has been established up to $I^\pi = 25^-$. Electric dipole ($E1$) transitions connecting the states of this negative-parity band and the positive-parity states of the ground-state band have been found to persist up to spin 17^-. Two interconnected negative-parity sequence of states have been observed at low-spin, having a 5^- and a tentative 4^- states as bandheads. Above the yrast 10^+ level a non-rotational, less regular level structure has also been found.

- Comparison of the high-spin states of ^{100}Pd with cranked Woods-Saxon calculations has yield that the negative-parity band 'terminates' at spin 25^- with the $[\nu(g_{7/2}, d_{5/2})^3 h_{11/2}\pi g_{9/2}^4)]_{25^-}$ maximum spin alignment. The $[\nu(g_{7/2}d_{5/2})^6\pi g_{9/2}^2]_{22^+}$ terminating configuration is also predicted for the positive-parity band. However, in our data, the highest observed spin had maximum at spin 18^+, which is the maximum spin available before the break-up of the second proton pair. Finally, the observed enhancement of E1 transitions between the positive- and negative-parity bands has been thought to reveal signs of octupole correlations in ^{100}Pd at high spins.

6.3 Perspectives

The results obtained in this work and in the references listed in Appendix B make me feel optimistic that with the experimental devices and techniques available today

and the future devices already under construction, nuclear physicists will gradually be reaching nuclei further away from the β-stability line, and up to even much higher spins than we do now.

A few events corresponding to the $Z = N$ doubly magic ^{100}Sn nucleus have been recently observed in projectile-fragmentation experiments [101, 102]. Evidence for excited states in the two-valence neutron ^{102}Sn nucleus has been reported in Ref. [94]. I have no doubt that excited states in the 'holy grail' of nuclear physics, the ^{100}Sn will be observed in-beam in a few-years time.

In Europe, much effort is being put onto the construction of the next generation γ-spectrometer EXOGAM (see, e.g. [103]), planned to be used with SPIRAL, a radioactive beam facility at GANIL. Not only will EXOGAM be a highly efficient spectrometer (the relative efficiency of detecting 1.3 MeV γ-rays will be $\geq 20\%$), but it has been designed to make full use of the selective power of ancillary detectors as well. Leading physicists of our research group at the ATOMKI, have joined the EXOGAM project, and amongst other activities, are building an array of charged-particle CsI detectors with its corresponding electronics for use at EXOGAM. (I myself have had the opportunity to take active part in the first phase of this detector development, but that work does not form part of this thesis.)

Chapter 7

Összefoglalás

Jelen értekezésben az erősen neutronhiányos ^{108,109,110}Te és ^{98,100}Pd atommagok szerkezetét vizsgáltam in-beam γ-spektroszkópiai módszerekkel. A kapott kísérleti eredményeket különböző magmodellek segítségével értelmeztem. Ennek eredményeképpen, ezen atommagokra vonatkozó ismereteink mind kísérleti, mind elméleti szempontból jelentősen bővültek. Egyúttal, bizonyítást nyert, hogy a segéd detektorrendszerekkel ellátott összetett γ-spektrométerek a β-stabilitási sávtól távol eső atommagok kísérleti kutatásának egyik leghatékonyabb eszköze. A következőkben munkámnak a vizsgált atommagok szempontjából legfontosabb eredményeit foglalom össze.

A kollektív munkát igénylő mérések a nemzetközi kutatási programban résztvevő társszerzők segítségével történtek. Jelen értekezésben leírt mérésekből nyert adatok feldolgozásában, és a kísérleti eredmények kimutatásában, továbbá a kísérleti eredmények magfizikai értelmezésében, valamint az alább felsorolt eredmények elérésében meghatározó szerepem volt.

7.1 Neutronhiányos Te atommagok

Az erősen neutronhiányos Te izotópokat a ^{54}Fe + ^{58}Ni nehézion reakcióban állítottuk elő, 270 MeV bombázó energiánál. A ^{108,109,110}Te izotópokat úgy kaptuk meg, hogy a ^{112}Xe közbenső magból két proton, s két, egy vagy nulla neutron párolgott el.

A kilépő részecskék és γ-sugárzások azonosítását a 15 db Compton-elnyomásos hipertiszta (HP) Ge detektorból, 21 db ΔE-típusú Si töltöttrészecske detektorból, a neutronok detektálását szolgáló 11 db folyadék szcintillátorból és egy 30-elemes BaF_2 kristálygömb γ-kaloriméterből álló NORDBALL detektorrendszerrel végeztük. A részecske-gamma típusú koincidencia eseményekből "kapuzott" E_γ-E_γ mátrixokat

állítottuk elő, a kilépő részecskék számára és típusára megkövetett olyan kapuzási feltételekkel, melyek az egyes reakció csatornáknak feleltek meg.

A ^{108,109,110}Te atommagok nívósémáit a így kapott γ-γ koincidencia adatok alapján építettük fel. A gerjesztett állapotok spin értékeinek meghatározásánál egy egyszerűsített $\gamma\gamma$ szögkorrelációs analízis eredményeit használtuk fel.

A ^{108,109,110}Te atommagokra vonatkozó – az értekezésemben bemutatott – eredmények ezen magok legelső in-beam módszerekkel való tanulmányozásából született eredmények. Ezelőtt a munka előtt a ^{108,109}Te magok egyik gerjesztett állapota sem volt ismert. A ^{110}Te izopót esetében is csak a $2^+ \rightarrow 0^+$ alapállapoti átmenet energiáját tudták meghatározni a ^{114}Xe mag α-bomlásának vizsgálatából.

A ^{108,109,110}Te atommagokra vonatkozó új tudományos eredményeket az alábbiakban foglalom össze.

- A ^{108}Te atommaghoz 10 új γ-átmenetet rendeltem hozzá, és felépítettem ezen mag $8\hbar$ spin értékig terjedő nivósémáját. Bizonyossággal megállapítottam az első gerjesztett állapot $I^\pi = 2^+$ értékét a mért szögkorrelációs hányados alapján. A többi nívóra javasolt spin értéke a nehezebb Te izotópok szisztematikáján alapul.

- A ^{110}Te nívósémáját $I^\pi = (21^-)$ spin értékig és 8.5 MeV gerjesztési energiáig építettem fel. A mért kísérleti adatokra alapozva meghatároztam a mag nívóinak energiáját és spin értékét. Az alapállapoti sáv alacsonyan fekvő állapotai pozitív paritásúak 8^+ spin értékig. Efelett a nívó felett, egy negatív paritású sávot figyeltünk meg, amely egy $9^{(-)}$ nívóra épül. Körülbelül $17\hbar$ spin értéknél egy sávkereszteződés volt megfigyelhető.

- A ^{108,110}Te magok alacsonyan fekvő 2^+, 4^+, 6^+ yrast állapotai szerkezete leginkább vibrációs fonon-gerjesztésnek felelnek meg. A ^{110}Te atommag negatív paritású sávjához a $\nu g_{7/2} \otimes \nu h_{11/2}$ két-kvázirészecske konfigurációt rendeltük. A kurblis-héjmodell számolások alapján a ^{110}Te alapállapota $\beta_2 \approx 0.15$ deformációval rendelkezik. A megfigyelt sávkereszteződés két $h_{11/2}$ neutron spinjének a forgási tengely irányába történő beállásával értelmezhető, a kereszteződés frekvenciáját azonban a modell nem adta meg pontosan. Mivel a számolásokban csak kvadrupól és hexadekupól deformációs paramétereket használtunk, arra lehetett következtetni, hogy más szabadsági fokok, mint például az oktupol korrelációk, jelentős szerepet játszhatnak a könnyű Te magokban magas spinű gerjesztésekben.

- A ^{109}Te atommaghoz több mint 30 új átmenetet rendeltünk, és felépítettük ezen mag új nívósémáját E_x=6716 keV gerejsztési energiáig. A kísérleti adatokra alapozva meghatároztuk a γ átmenetek pontos energiáját, relatív intenzitását és az általuk elvitt impulzusmomentumot. Megfigyeltünk egy $E2$ típusú intraband átmenetekből álló erősen gerjesztett negatív paritású sávot 35/2 spin értékig. Egy másik, gyengébben gerjesztett pozitív paritású sávot 15/2 spin értékig sikerült azonosítanunk.

- A ^{109}Te magszerkezetét a kölcsönható bozon-fermion model keretében tárgyaltuk. A számolások alapján a ^{109}Te alapállapota a $d_{5/2}$ kvázineutron állapot, a pozitív paritású gerjesztett állapotok pedig a $\nu d_{5/2}\otimes 2^+$ és $\nu g_{7/2}\otimes 2^+$, 4^+, 6^+ multipletek tagjai. A negatív paritású sávot $h_{11/2}$ neutron állapotok és a ^{108}Te törzs yrast állapotai csatolódásával értelmeztük. A $27/2\hbar$ spin felett, ami az IBFM alapján számolt legmagasabb spin érték, a $\hbar\omega \approx 0.45$ MeV-nél megfigyelt spin-növekedést cranked Strutinsky számolások alapján nem lehetett értelmezni két neutron spinbeállásával. Az eltérést valószínűleg a vibráció-rotáció csatolódása okozza.

7.2 Neutronhiányos Pd atommagok

A ^{98}Pd és ^{100}Pd magas spinű állapotait a ^{50}Cr + ^{58}Ni nehézion reakcióban 261 MeV bombázó energiánál vizsgáltuk a NORDBALL detektorrendszer segítségével. A ^{100}Pd magas spinű állapotai analízisénél a ^{70}Zn(^{36}S,6n) reakcióból az EUROGAM II spektrométer segítségével nyert kísérleti adatokat is használtuk.

A vizsgált magok nívósémájának felépítése céljából, a NORDBALL adatokból különböző számú és típusú részecskével koincidenciában mért γ-γ eseményeket tároló két dimenziós mátrixokat, míg az EUROGAM II adatokból egy kapuzott γ-γ-γ koincidencia 'kockát' hoztunk létre, ahol kapuzási feltételként, a ^{100}Pd legerősebb γ-átmeneteivel való koincidenciát követeltük meg. A nívók spinjét és paritását γ-γ szögkorrelációs analízis, DCO arányok és lineáris polárizáció adatok alapján határoztuk meg.

Munkám eredményeként a ^{98}Pd és ^{100}Pd magokról korábban ismert nívósémákat jelentősen kiterjesztettem, új szerkezeteket figyeltem meg bennük. Az elért eredményeket az alábbiakban ismertetem..

- Közel 40 új γ átmenetet azonosítottam a ^{98}Pd atommagban, és felépítettem egy, az eddiginél teljesebb nívósémát 10.9 MeV gerjesztési energiáig. A kísérleti

adatokra alapozva meghatároztam a mag nívóinak energiáját, a γ átmenetek relatív intenzitását és az általuk elvitt impulzusmomentumot. A feldolgozás során megerősítettük a pozitív paritású páros spinű állapotok a nívósémában történő korábbi elhelyezését $14\hbar$ spin értékig. Efelett a nívó felett a korábbi eredmények módosítását és kiterjesztét javasoltuk. Az 8508 keV-es állapotra $18\hbar$ spin és pozitív paritás hozzárendelést javasoltuk. Kvalitatív megfontolások alapján a szóban forgó állapot a $[\pi g_{9/2}^{-4}\nu g_{7/2}^2]_{18^+}$ és a $[\pi g_{9/2}^{-4}\nu g_{7/2}d_{5/2}]_{18^+}$ sávlezáró konfigurációk keveredéséből eredhet. Először ebben a munkában figyeltünk meg egy, az 2620 keV-es 5^- spinű nívóra épülő, negatív paritású sávot. Az $I^\pi = 11^-$ értékig a sáv szerkezete egy négy-kvázi-részecskés $\pi g_{9/2}^{-3}\pi p_{1/2}^{-1}$ konfigurációval írható le. A $11\hbar$ spin fölött a legvalószínűbb egy olyan 6-kvázi-részecskés konfiguráció, ahol az ^{102}Sn első (neutron) 2^+ állapotához egy 4-kvázirészecskés proton gerjesztés csatolódik.

- Közel 50 új γ átmenetet azonosítottam a ^{100}Pd atommagban és felépítettem annak 16 MeV gerjesztési energiáig és $\sim 25\hbar$ impulzusmomentum-ig terjedő nívósémáját. A kísérleti adatokra alapozva meghatároztam a mag nívóinak energiáját, a γ átmenetek relatív intenzitását és az általuk elvitt impulzusmomentumot. Adataink alapján a 4054 keV-es állapothoz egyértelműen $I^\pi = 9^-$ értéket rendeltünk hozzá. Az erre az állapotra épülő negatív paritású sávot 25^- spinig figyeltük meg. Elektromos dipol ($E1$) átmeneteket mutattunk ki ezen negatív paritású sáv (17^--ig) és a pozitív paritású alapállapoti sáv között. Továbbá megfigyeltünk két alacsony spinű, csatolt negatív paritású sávot, melyek egy 5^- és egy valószínűleg 4^- állapotra épülnek. Számos – szabálytalan nívószerkezetet alkotó – pozitív paritású nívót azonosítottunk a 10^+ yrast nívónál feletti energiáknál.

- A ^{100}Pd magas spinű állapotait a cranked héjmodell számolásokkal értelmeztük. Az összevetés eredményeként a negatív paritású sáv 25^- állapotánál sávlezárás figyelhető meg a maximális spin beállású $[\nu(g_{7/2},d_{5/2})^3 h_{11/2}\pi g_{9/2}^4)]_{25^-}$ konfiguráció révén. A pozitív paritású sávra is ki lehetett mutatni a $[\nu(g_{7/2}d_{5/2})^6\pi g_{9/2}^2]_{22^+}$ másik sávlezáró konfigurációt, de a kísérletileg megfigyelt maximális spin érték 18^+ volt. Ez a legmagasabb elérhető spin, ha a második proton pár még nem hasadt fel. A pozitív és negatív paritású sávok között megfigyelt felerősödött $E1$ átmenetekből arra lehetett következtetni, hogy az oktupol korrelációk meghatározó szerepet játszhatnak a ^{100}Pd magas spinű állapotainak szerkezetében.

Bibliography

[1] W. Gelletly, *Proceedings of the Conference Structure of Nuclei under Extreme Conditions, March 31 - April 4 1998, Padova*, Società Italiana di Fisica, edited by S. Lunardi, R. A. Ricci and W. von Oertzen, p.757.

[2] G. A. Leander, J. Dudek, W. Nazarewitz, J. R. Nix and Ph. Quentin, *Phys. Rev. C* **30** (1984) 416.

[3] J. Skalski, Phys. Lett. **B238** (1990) 6.

[4] I. Ragnarsson, A. V. Afanasjev and J. Gizon, *Z. Phys. A* **355** (1996) 383.

[5] H. Ejiri and M. J. A. de Voigt, *Gamma-ray and electron spectroscopy in nuclear physics*, Clarendon Press, Oxford (1989).

[6] D. Seweryniak, B. Cederwall, J. Nyberg, C. Fahlander, A. Johnson, A. Kerek, J. Kownacki, L.-O. Norlin, E. Adamides, A. Ataç, J. Blomqvist, H. Grawe, E. Ideguchi, R. Julin, S. Juutinen, W. Karczmarczyk, S. Mitarai, M. Piiparinen, R. Schubart, G. Sletten, S. Törmänen and A. Virtanen, *Z. Phys.* **A345** (1993) 243.

[7] D. Seweryniak, J. Cederkäll, B. Cederwall, J. Blomqvist, C. Fahlander, A. Johnson, L.-O. Norlin, J. Nyberg, A. Ataç, A. Kerek, J. Kownacki, R. Wyss, E. Adamides, H. Grawe, E. Ideguchi, R. Julin, S. Juutinen, W. Karczmarczyk, S. Mitarai, M. Piiparinen, R. Schubart, G. Sletten, S. Törmänen and A. Virtanen, *Phys. Lett.* **B321** (1994) 323.

[8] J. Cederkäll, B. Cederwall, A. Johnson, D. Seweryniak, J. Nyberg, L.-O. Norlin, J. Blomqvist, C. Fahlander, R. Wyss, A. Kerek, J. Kownacki, A. Ataç, E. Adamides, E. Ideguchi, R. Julin, S. Juutinen, W. Karczmarczyk, S. Mitarai, M. Piiparinen, R. Schubart, G. Sletten, S. Törmänen and A. Virtanen, *Nucl. Phys.* **A581** (1995) 189.

[9] Zs. Dombrádi, B. M. Nyakó, G. Perez, A. Algora, C. Fahlander, D. Seweryniak, J. Nyberg, A. Ataç, B. Cederwall, A. Johnson, A. Kerek, J. Kownacki, L.-O. Norlin, R. Wyss, E. Adamides, E. Ideguchi, R. Julin, S. Juutinen, W. Karczmarczyk, S. Mitarai, M. Piiparinen, R. Schubart, G. Sletten, S. Törmänen and A. Virtanen, *Z. Phys.* **A350** (1994) 3.

[10] Zs. Dombrádi, B. M. Nyakó, G. Perez, A. Algora, C. Fahlander, D. Seweryniak, J. Nyberg, A. Ataç, B. Cederwall, A. Johnson, A. Kerek, J. Kownacki, L.-O. Norlin, R. Wyss, E. Adamides, E. Ideguchi, R. Julin, S. Juutinen, W. Karczmarczyk, S. Mitarai, M. Piiparinen, R. Schubart, G. Sletten, S. Törmänen and A. Virtanen, *Phys. Rev.* **C51** (1995) 2394.

[11] M. Karny, J. Kownacki, D. Seweryniak, A. Ataç, B. Cederwall, C. Fahlander, A. Johnson, A. Kerek, L.-O. Norlin, J. Nyberg, E. Adamides, E. Ideguchi, R. Julin, S. Juutinen, W. Karczmarczyk, S. Mitarai, M. Piiparinen, R. Schubart, G. Sletten, S. Törmänen and A. Virtanen, *Z. Phys.* **A350** (1994) 179.

[12] C. Fahlander, D. Seweryniak, J. Nyberg, Zs. Dombrádi, G. Perez, M. Józsa, B. M. Nyakó, A. Ataç, B. Cederwall, A. Johnson, A. Kerek, J. Kownacki, L.-O. Norlin, R. Wyss, E. Adamides, E. Ideguchi, R. Julin, S. Juutinen, W. Karczmarczyk, S. Mitarai, M. Piiparinen, R. Schubart, G. Sletten, S. Törmänen and A. Virtanen, *Nucl. Phys.* **A577** (1994) 773.

[13] M. Lipoglavšek, J. Cederkäll, M. Palacz, J. Persson, A. Ataç, H. Grawe, C. Fahlander, A. Johnson, A. Kerek, W. Klamra, J. Kownacki, A. Likar, , L.-O. Norlin, J. Nyberg, R. Schubart, D. Seweryniak, G. de Angelis, P. Bernadczyk, Zs. Dombrádi, D. Foltescu, D. Jerrestam, , S. Juutinen, E. Mäkelä, G. E. Perez, M. de Poli, H. A. Roth, T. Schizuma, Ö. Skeppstedt, G. Sletten, S. Törmänen and T. Vass, *Phys. Rev. Lett.* **76** (1996) 888

[14] J. Cederkäll, M. Lipoglavšek, M. Palacz, J. Persson, A. Ataç, C. Fahlander, H. Grawe, A. Johnson, W. Klamra, J. Kownacki, A. Likar, , L.-O. Norlin, J. Nyberg, R. Schubart, D. Seweryniak, G. de Angelis, P. Bernadczyk, Zs. Dombrádi, D. Foltescu, D. Jerrestam, , S. Juutinen, E. Mäkelä, B. M. Nyakó, G. Perez, M. de Poli, H. A. Roth, T. Schizuma, Ö. Skeppstedt, G. Sletten and S. Törmänen, *Phys. Rev.* **C53** (1996) 1955.

[15] J. Kownacki, M. Lipoglavšek, D. Seweryniak, L-O. Norlin, J. Nyberg, J. Cederkäll, M. Palacz, J. Persson, A. Atac, B. Cederwall, F. Lindén, C. Fahlander,

H. Grawe, A. Johnson, A. Kerek, W. Klamra, M. Karny, A. Likar, R. Schubart, R. Wyss, E. Adamides, G. de Angelis, P. Bednarczyk, Zs. Dombrádi, D. Foltescu, E. Ideguchi, D. Jerrestam, R. Julin, S. Juutinen, S. Mitarai, E. Mäkelä, G. Perez, M. Piiparinen, M. de Poli, H. A. Roth, T. Shizuma, Ö. Skeppstedt, G. Sletten, S. Törmämen, T. Vass, A. Virtanen, Nucl. Phys. **A 627** (1997) 239.

[16] M. Palacz, J. Cederkäll, M. Lipoglavšek, J. Persson, A. Atac, J. Blomqvist, C. Fahlander, H. Grawe, A. Johnson, A. Kerek, J. Kownacki, A. Likar, L-O. Norlin, J. Nyberg, R. Schubart, D. Seweryniak, R. Wyss, G. de Angelis, P. Bednarczyk, Zs. Dombrádi, D. Foltescu, D. Jerrestam, S. Juutinen, E. Mäkelä, G. Perez, M. de Poli, H. A. Roth, T. Shizuma, Ö. Skeppstedt, G. Sletten, S. Törmämen, T. Vass, Nucl. Phys. **A 608** (1996) 227.

[17] J. Persson, J. Cederkäll, M. Lipoglavšek, M. Palacz, A. Ataç, J. Blomquist, C. Fahlander, H. Grawe, A. Johnson, A. Kerek, W. Klamra, J. Kownacki, A. Likar, L-O. Norlin, J. Nyberg, R. Schubart, D. Seweryniak, G. de Angelis, P. Bednarczyk, Zs. Dombrádi, D. Foltescu, D. Jerrestam, S. Juutinen, E. Mäkelä, G. Perez, M. de Poli, H. A. Roth, T. Shizuma, Ö. Skeppstedt, G. Sletten, S. Törmämen, T. Vass, Nucl. Phys. **A 627** (1997) 101.

[18] M. Palacz, J. Cederkäll, M. Lipoglavšek, J. Persson, A. Ataç, J. Blomqvist, H. Grawe, C. Fahlander, J. Iwanicki, A. Johnson, A. Kerek, J. Kownacki, A. Likar, L-O. Norlin, J. Nyberg, R. Schubart, D. Seweryniak, Z. Sujkowski, R. Wyss, G. de Angelis, P. Bednarczyk, Zs. Dombrádi, D. Foltescu, D. Jerrestam, S. Juutinen, E. Mäkelä, G. Perez, M. de Poli, H. A. Roth, T. Shizuma, Ö. Skeppstedt, G. Sletten, S. Törmämen, T. Vass, Nucl. Phys. **A 624** (1997) 210.

[19] J . Cederkäll, M. Lipoglavšek, M. Palacz, J. Persson, J. Blomqvist, A. Ataç, C. Fahlander, H. Grawe, A. Johnson, W. Klamra, J. Kownacki, A. Likar, L-O. Norlin, J. Nyberg, R. Schubart, D. Seweryniak, G. de Angelis, P. Bednarczyk, Zs. Dombrádi, D. Foltescu, M. Gorska, D. Jerrestam, S. Juutinen, E. Mäkelä, B. M. Nyakó, G. Perez, M. de Poli, H. A. Roth, T. Shizuma, Ö. Skeppstedt, G. Sletten, S. Törmanen, Eur. Phys. Jour. A **1** (1998) 7.

[20] D. Sohler, Zs. Dombrádi, J. Timár, J . Cederkäll, M. Lipoglavšek, M. Palacz, J. Persson, J. Blomqvist, A. Atac, C. Fahlander, H. Grawe, A. Johnson, W.

Klamra, J. Kownacki, A. Likar, L-O. Norlin, J. Nyberg, R. Schubart, D. Seweryniak, G. de Angelis, P. Bednarczyk, D. Foltescu, M. Gorska, D. Jerrestam, S. Juutinen, E. Mäkelä, B. M. Nyakó, G. Perez, M. de Poli, H. A. Roth, T. Shizuma, Ö. Skeppstedt, G. Sletten, S. Törmanen, to be published.

[21] J. Cederkäll, G. Perez, M. Lipoglavšek, M. Palacz, J. Persson, A. Atac, J. Blomquist, C. Fahlander, H. Grawe, A. Johnson, W. Klamra, J. Kownacki, A. Likar, L-O. Norlin, J. Nyberg, R. Schubart, D. Seweryniak, G. de Angelis, P. Bednarczyk, Zs. Dombrádi, D. Foltescu, D. Jerrestam, S. Juutinen, E. Mäkelä, B. M. Nyakó, M. de Poli, H. A. Roth, T. Shizuma, Ö. Skeppstedt, G. Sletten, S. Törmämen, Z. Phys. A **359** (1997) 227.

[22] G. E. Perez, Zs. Dombrádi, A. Algora, B. M. Nyakó, D. Sohler, J. Timár, R. Wyss, J. Cederkäll, M. Lipoglavšek, M. Palacz, J. Persson, A. Atac, A. J. Boston, C. Fahlander, A. Gizon, J. Gizon, H. Grawe, A. Johnson, D. T. Joss, A. Kerek, W. Klamra, J. Kownacki, A. Likar, L.-O. Norlin, J. Nyberg, R. Schubart, D. Seweryniak, G. de Angelis, P. Bednarczyk, D. Foltescu, D. Jerrestam, S. Juutinen, E. Mäkelä, E. S. Paul, M. de Poli, H. A. Roth, T. Shizuma, Ö. Skeppstedt, G. Sletten, and S. Törmänen, to be submitted to Nucl. Phys. A.

submitted to Nucl. Phys. A

[23] B. M. Nyakó *et al*, Conference proceedings, Cape Town (1999)

[24] J. Gizon, B. M. Nyakó, J. Timár, A. Gizon, L. Zolnai, A. J. Boston, Gh. Cata-Danil, J. Genevey, D. T. Joss, N. J. O'Brien, C. M. Parry, E. S. Paul, D. Santos, A. T. Semple, A. V. Afanasjev, I. Ragnarsson, Phys. Lett. **B 410** (1997) 95.

[25] B. M. Nyakó, J. Gizon, A. Gizon, J. Timár, L. Zolnai, A. J. Boston, D. T. Joss, E. S. Paul, A. T. Semple, N. J. O'Brien, C. M. Parry, A. V. Afanasjev, I. Ragnarsson, *Phys. Rev. C* **60** (1999).

[26] A. Gizon, Gh. Cata-Danil, J. Gizon, J. Timár, B. M. Nyakó, L. Zolnai, A. J. Boston, D. T. Joss, E. S. Paul, A. T. Semple, N. J. O'Brien, C. M. Parry, Eur. Phys. Jour. A **2** (1998) 325.

[27] J. Timár, J. Gizon, A. Gizon, L. Zolnai, B. M. Nyakó, Gh. Cata-Danil, D. Bucurescu, A. J. Boston, D. T. Joss, E. S. Paul, A. T. Semple, N. J. O'Brien, C. M. Parry, A. V. Afanasjev, I. Ragnarsson, Eur. Phys. Jour. A **4** (1999) 11

[28] J. Gizon, Gh. Cata-Danil, A. Gizon, J. Timár, B. M. Nyakó, L. Zolnai, D. Bucurescu, A. J. Boston, D. T. Joss, N. J. O'Brien, C. M. Parry, E. S. Paul, A. T. Semple, A. V. Afanasjev, I. Ragnarsson, Phys. Rev. C **59** (1999) R570

[29] B. Herskind, Nucl. Phys. **A447**, (1985) 395.

[30] G. Sletten, *Proc. Int. Seminar on The Frontiers of Nuclear Spectroscopy*, Kyoto 1992, World Scientific (1993).

[31] M. Moszyński *et al.*, Nucl. Instr. Meth. **A280** (1989) 73.

[32] T. Kuroyanagi, S. Mitarai, S. Suematsu, B. J. Min, H. Tomuza, J. Mukai, T. Maeda, R. Nahatani, G. Sletten, J. Nyberg, and D. Jerrestam, Nucl. Instr. Meth. **A316** (1992) 289.

[33] S. E. Arnell, H. A. Roth, Ö. Skeppstedt, J. Białkowski, M. Moszyński, D. Wolski, and J. Nyberg, Nucl. Instr. Meth. **A300** (1991) 303.

[34] J. Białkowski, M. Moszyński and D. Wolski, Nucl. Instr. Meth. **A275** (1989) 322.

[35] A. Holm, *ACQ-91, NBI Data Acquisition System*, Niels Bohr Institute, 1991.

[36] T. Ramsøy, *NORDBALL Front-End Electronics User's Guide*, Niels Bohr Institute, 1992.

[37] M. Palacz, PhD thesis, Sołtan Institute for Nuclear Studies, Świerk, 1996.

[38] P. J. Nolan, F. A. Beck, D. B. Fossan, Annu Rev. Nucl. Part. Sci. 45 (1995) 561.

[39] M. Palacz, J. Cederkäll, M. Lipoglavsek, J. Persson, L.-O. Norlin and J. Nyberg, Nucl. Instr. Meth. **A383** (1996) 473.

[40] A. Johnson *et al.*, Nucl. Phys. A 557 (1993) 401c.

[41] D. Wolski, M. Moszýnski, T. Ludziejewski, A. Johnson, W. Klamra and Ö. Skeppstedt, Nucl. Instr. Meth. **A360** (1995) 584.

[42] D. C. Radford, Nucl. Instr. Meth. **A361** (1995) 290.

[43] Zs. Dombrádi, B. M. Nyakó, M. Józsa, Atomki Annual Report 1994, 1995, p.11

[44] L. P. Ekström and A. Norlund, Nucl. Instr. Meth. **A313** (1992) 421.

[45] M. Palacz *al*, to be published.

[46] K. S. Krane, R. M. Steffen and R. M. Wheeler, Nuclear Data Tables **A 11** (1973) 351

[47] L. P. Ekström, Internal Report, LUIP9108, Lund, 1991

[48] P. M. Jones, L. Wei, F. A. Beck, P. A. Butler, T. Byrski, G. Duchene, G. deFrance, F. Hannachi, G. D. Jones and B. Kharraja,

[49] P. J. Twin, *Nucl. Instr. Meth.* **106** (1973) 481

[50] A. de Shalit and I. Talmi, *Nuclear shell theory*, Academic Press, New York, 1963

[51] P. J. Brussard and P. W. M. Glaudemans, *Shell-model applications in nuclear spectroscopy*, North-Holland Publishing Co., 1977

[52] K. Heyde, *The Nuclear Shell Model*, Springer-Verlag, 1990

[53] M. G. Mayer, *Phys. Rev.* **75** (1949) 1969

[54] O. Haxel, J. H. D. Jensen and H. E. Suess, *Phys. Rev.* **75** (1949) 1766

[55] A. Arima and F. Iachello, Phys. Rev. Lett. **35** (1975) 1069; D. Janssen, R. V. Jolos and F. Dönau, Nucl. Phys. **A224** (1974) 93

[56] F. Iachello and P. Van Isacker, *The Interacting Boson-Fermion Model*, Cambridge University Press, Cambridge, 1991

[57] F. Iachello and O. Sholten, Phys. Rev. Lett. **43** (1979) 679; V. Paar, S. Brant, L. F. Canto, G. Leander and M. Vouk, Nucl. Phys. **A378** (1982) 41

[58] W. Nazarewicz, J. Dudek, R. Bengtsson and I. Ragnarsson, Nucl. Phys. **A435** (1985) 397

[59] D. R. Inglis, Phys. Rev. **96** (1954) 1059; D. R. Inglis, Phys. Rev. **103** (1956) 1786

[60] V. M. Strutinsky, *Nucl. Phys.* **A95** (1967) 420.

[61] A. Luukko, A. Kerek, I. Rezanka and C. J. Herrlander, Nucl. Phys. **A135** (1969) 49.

[62] T. Lönnroth, A. Virtanen and J. Hattula, Physica Scripta **34** (1986) 682.

[63] A. Sharma, J. Goswamy, D. Mehta, J. Singh, H. Kaur, B. Chand, N. Singh, R. K. Bhowmik, P. N. Trehan, *Z. Phys. A* **346** (1993) 321.

[64] C.-B. Moon, J. U. Kwon, S. J. Chae, J. C. Kim, S. H. Bhatti, C. S. ... Phys. Rev. C **51** (1995) 2222.

[65] I. Thorslund, D. B. Fossan, D. R. LaFosse, H. Schnare, K. Hauschild, I. M. Hibbert, S. M. Mullins, E. S. Paul, I. Ragnarsson, J. M. Sears, P. Vaska and R. Wadsworth Phys. Rev. C **52** (1995) R2839.

[66] J. M. Sears, D. B. Fossan, I. Thorslund, P. Vaska, E. S. Paul, K. Hauschild, I. M. Hibbert, R. Wadsworth, S. M. Mullins, A. V. Afanasjev, I. Ragnarsson *Phys. Rev. C* **55** (1997) 2290.

[67] E. S. Paul, C. W. Beausang, S. A. Forbes, S. J. Gale, A. N. James, P. M. Jones, M. J. Joyce, H. R. Andrews, V. P. Janzen, D. C. Radford, D. Ward, R. M. Clark, K. Hauschild, I. M. Hibbert, R. Wadsworth, R. A. Cunningham, J. Simpson, T. Davinson, R. D. Page, P. J. Sellin, P. J. Woods, D. B. Fossan, D. R. LaFosse, H. Schnare, M. P. Waring, A. Gizon, J. Gizon, T. E. Drake, J. DeGraaf, S. Pilotte, *Phys. Rev. C* **50** (1994) 698.

[68] J. Blachot, Nucl. Data Sheets **62** (1991) 803.

[69] J. Blachot, Nucl. Data Sheets **64** (1991) 913.

[70] D. De Frenne, E. Jacobs, Nucl. Data Sheets **67** (1992) 809.

[71] D. Schardt, R. Kirchner, O. Klepper, W. Reisdorf, E. Roeckl, P. Tidemand-Petersson, G. T. Ewan, E. Hagberg, B. Jonson, S. Mattsson, G. Nyman *Nucl. Phys.* **A326** (1979) 65.

[72] D. Schardt, T. Batsch, R. Kirchner, O. Klepper, W. Kurcewicz, E. Roeckl, P. Tidemand-Petersson *Nucl. Phys.* **A368** (1981) 153.

[73] P. Tidemand-Petersson, R. Kirchner, O. Keppler, E. Roeckl, D. Schardt, A. Płochocki and J. Żylicz, *Nucl. Phys.* **A437** (1985) 342.

[74] F. Heine, T. Faestermann, A. Gillitzer, J. Homolka, M. Köpf and W. Wagner, *Z. Phys. A* **340** (1991) 225.

[75] W. Nazarewicz, R. Wyss and A. Johnson, Nucl. Phys. **A503** (1989) 285.

[76] D. Sohler, J. Cederkäll, Zs. Dombrádi, J. Persson, B. Cederwall, A. Johnson, L.-O. Norlin, M. Weiszflog, A. Atac, J. Blomquist, R.A. Bark, A. Kerek, W. Klamra, J. Kownacki, M. Lipoglavšek, S. Mitarai, J. Nyberg, H.A. Roth and G. Sletten, Eur. Phys. J. **A3** (1998) 209.

[77] G. J. Lane, D. B. Fossan, J. M. Sears, J. F. Smith, J. A. Cameron, R. M. Clark, I. M. Hibbert, V. P. Janzen, R. Krucken, I.-Y. Lee, A. O. Macchiavelli, C. M. Parry, R. Wadsworth, Phys. Rev. **C57** (1998) R1022.

[78] R. Bengtsson and S. Frauendorf, Nucl. Phys. **A327** (1979) 139.

[79] E. S. Paul, H. R. Andrews, T. E. Drake, J. DeGraaf, V. P. Janzen, S. Pilotte, D. C. Radford, D. Ward Phys. Rev. C **50** (1994) R534.

[80] I. Thorslund, C. Fahlander, J. Nyberg, S. Juutinen, R. Julin, M. Piiparinen, R. Wyss, A. Lampinen, T. Lönnroth, D. Müller, S. Törmänen and A. Virtanen, *Nucl. Phys.* **A564** (1993) 285.

[81] S. Juutinen *et al*, *Z. Phys.* **A336** (1990) 475.

[82] D. De Frenne and E. Jacobs, Nucl. Data Sheets **68**, 935 (1993) 935.

[83] D. De Frenne, E. Jacobs, M. Verboven and P. De Gelder, Nucl. Data Sheets **47** (1986) 261.

[84] L. S. Kisslinger and R. A. Sorensen, Rev. Mod. Phys. **35** (1963) 853.

[85] F. Dönau and D. Janssen, Nucl. Phys. **A209** (1973) 109.

[86] M. Huyse, K. Cornelis, G. Dumont, G. Lhersonneau, J. Versplancke and W. B. Walters, *Z. Phys. A* **288** (1978) 107.

[87] C. E. Thorn, P. D. Bond, M. J. LeVine, W. F. Piel, Jr., and A. Gallman, *Phys. Rev. C* **25** (1982) 331.

[88] W. F. Piel and G. Scharff-Goldhaber, *Phys. Rev. C* **30** (1984) 902.

[89] J. Sau et al. Nucl. Phys. **A410** 14 (1983)

[90] W. F. Piel, G. Scharff-Goldhaber, A. H. Lumpkin, Y. K. Lee, and D. C. Stromswold, Phys. Rev. C **23**, 708 (1981).

[91] S. K. Tandel, S. B. Patel, Pragya Das, R.¶. Singh and R. K. Bhowmik, Z. Phys. A **357** (1997) 3.

[92] G. E. Perez, B.M. Nyakó, Zs. Dombrádi *et al* Atomki Annual Report 1995 (1996) 12; CENBG, Bordeaux (1996), unpublished.

[93] J. A. Grau, L. E. Samuelson, F. A. Rickey, P. C. Simms, and G. J. Smith, Phys. Rev. C **14** (1976) 2297.

[94] M. Lipoglavšek et al. Z. Phys. **A356** 239 (1996)

[95] J. Timár, J. Gizon, A. Gizon, B. M. Nyakó, D. Sohler, L. Zolnai, A. J. Boston, D. T. Joss, E. S. Paul, A. T. Semple, N. J. O'Brien, C. M. Parry, I. Ragnarsson, to be submitted to Phys. Rev. C.

[96] W. Satuła, R.Wyss and P. Magierski, Nucl. Phys. **A578** (1994) 45.

[97] A. V. Afanasjev, D. B. Fossan, G. J. Lane, I. Ragnarsson, to be published in Phys. Rep.

[98] F. R. Xu, P. Walker, J. Sheikh and R. Wyss, *Phys. Lett.* **B435**(1998) 257.

[99] P. A. Butler and W. Nazarewicz, *Rev. Mod. Phys.* **68** (1996) 349.

[100] G. de Angelis, . Fahlander, A. Gadea, E. Farnea, D. Bazzaco, N. Belcari, N. Blasi, P. G. Bizzeti, A. Bizzeti-Sona, D. de Acuna, M. De Poli, H. Grawe, A. Johnson, G. Lo Bianco, S. Lunardi, D. R. Napoli, J. Nyberg, P. Pavan, J. Persson, C. Rossi Alvarez, D. Rudolph, R. Schubart, P. Spolaore, R. Wyss, F. Xu, Phys. Lett. B 437 (1998) 236.

[101] R. Shcneider *et al Z. Phys. A* **348** (1994) 241.

[102] M. Lewitowitcz *et al Phys. Lett. B* **332** (1994) 20.

[103] F. Azaiez, W. Korten, *Nuclear Physics News* Vol. 7, No. 4 (1997) 21.

Appendix A

Acknowledgements

This thesis is not only the fruit of my work in the field of nuclear spectroscopy. It has many components, which can not simply be described in terms of broken pairs or smooth band terminations.

First of all, I would like to express my gratitude to my supervisor, dr. Barna Nyakó, who accepted me as his nuclear physics apprentice when I was a recent Cuban immigrant, arrived from Russia, and without the slightest idea about superdeformation. Thank you for your guidance during more than three years in the ATOMKI, and afterwards as well. Thank you also for dedicating a great part of your family time to help me finalising the work on this thesis.

I had and continue to have a very pleasant time in the department of Nuclear Spectroscopy, in the company of Zoltán Máté and László Zolnai. Zsolt Dombrádi was always ready to answer my numerous questions of practical, theoretical, and also 'impractical' character. I am grateful to him, too. I also appreciate the help of Alejandro Algora, Dora Sohler and János Timár specially during the EUROGAM II data analysis.

Most of what I learned about the NORDBALL detector array and data analysis I owe to a few-month scholarship in Sweden. I am indebted for this to Arne Johnson, Andras Kerek and Johan Nyberg. My tribulations in Stockholm and Uppsala cannot be remembered without mentioning also the names of Marcin Palacz, Joakim Cederkäll, Lars-Olov Norlin, Ramon Wyss, Janne Persson, and many others.

My participation in the experimental work leading to this thesis and my research work at the ATOMKI was partially supported by grants from the Hungarian Fund for Scientific Research (OTKA). The final preparation of this dissertation was supported through a 'Belföldi Doktorandusz Ösztöndíj' scholarship granted by the Hungarian Soros Foundation.

Finally, I dedicate my special thanks to my wife, for her continuous encouragement and support, for making me believe that this thesis could become a reality; and to my little son, who forgave me not playing with him while I was writing these lines.

Appendix B

Publications

The work presented in this thesis is based on the following publications:

1. Zs. Dombrádi, B. M. Nyakó, **G. E. Perez**, A. Algora, C. Fahlander, D. Seweryniak, J. Nyberg, A. Ataç, B. Cederwall, A. Johnson, A. Kerek, J. Kownacki, L.-O. Norlin, R. Wyss, E. Adamides, E. Ideguchi, R. Julin, S. Juutinen, W. Karczmarczyk, S. Mitarai, M. Piiparinen, R. Schubart, G. Sletten, S. Törmänen and A. Virtanen,
   Identification and spectroscopy of ^{108}*Te.*
   Z. Phys. **A350** (1994) 3.

2. Zs. Dombrádi, B. M. Nyakó, **G. E. Perez**, A. Algora, C. Fahlander, D. Seweryniak, J. Nyberg, A. Ataç, B. Cederwall, A. Johnson, A. Kerek, J. Kownacki, L.-O. Norlin, R. Wyss, E. Adamides, E. Ideguchi, R. Julin, S. Juutinen, W. Karczmarczyk, S. Mitarai, M. Piiparinen, R. Schubart, G. Sletten, S. Törmänen and A. Virtanen,
   High-spin spectroscopy of ^{109}*Te.*
   Phys. Rev. **C51** (1995) 2394.

3. C. Fahlander, D. Seweryniak, J. Nyberg, Zs. Dombrádi, **G. E. Perez**, M. Józsa, B. M. Nyakó, A. Ataç, B. Cederwall, A. Johnson, A. Kerek, J. Kownacki, L.-O. Norlin, R. Wyss, E. Adamides, E. Ideguchi, R. Julin, S. Juutinen, W. Karczmarczyk, S. Mitarai, M. Piiparinen, R. Schubart, G. Sletten, S. Törmänen and A. Virtanen,
   In-beam spectroscopy of ^{110}*Te.*
   Nucl. Phys. **A577** (1994) 773.

4. J. Cederkäll, **G. E. Perez**, M. Lipoglavšek, M. Palacz, J. Persson, A. Atac, J. Blomquist, C. Fahlander, H. Grawe, A. Johnson, W. Klamra, J. Kownacki,

A. Likar, L-O. Norlin, J. Nyberg, R. Schubart, D. Seweryniak, G. de Angelis, P. Bednarczyk, Zs. Dombrádi, D. Foltescu, D. Jerrestam, S. Juutinen, E. Mäkelä, B. M. Nyakó, M. de Poli, H. A. Roth, T. Shizuma, Ö. Skeppstedt, G. Sletten, S. Törmämen,
New spectroscopic information on ^{98}Pd.
Z. Phys. A **359** (1997) 227.

5. **G. E. Perez**, A. Algora, Zs. Dombrádi, B. M. Nyakó, D. Sohler, J. Timár, R. Wyss, J. Cederkäll, M. Lipoglavšek, M. Palacz, J. Persson, A. Atac, A. J. Boston, C. Fahlander, A. Gizon, J. Gizon, H. Grawe, A. Johnson, D. T. Joss, A. Kerek, W. Klamra, J. Kownacki, A. Likar, L.-O. Norlin, J. Nyberg, R. Schubart, D. Seweryniak, G. de Angelis, P. Bednarczyk, D. Foltescu, D. Jerrestam, S. Juutinen, E. Mäkelä, E. S. Paul, M. de Poli, H. A. Roth, T. Shizuma, Ö. Skeppstedt, G. Sletten, and S. Törmänen,
Structure of High Spin States in ^{100}Pd.
being submitted to Nucl. Phys. A.

Other results obtained from the experiments described in this thesis with the author's contribution have been published in the following papers:

1. J. Cederkäll, M. Lipoglavšek, M. Palacz, J. Persson, A. Ataç, C. Fahlander, H. Grawe, A. Johnson, W. Klamra, J. Kownacki, A. Likar, , L.-O. Norlin, J. Nyberg, R. Schubart, D. Seweryniak, G. de Angelis, P. Bernadczyk, Zs. Dombrádi, D. Foltescu, D. Jerrestam, , S. Juutinen, E. Mäkelä, B. M. Nyakó, G. Perez, M. de Poli, H. A. Roth, T. Schizuma, Ö. Skeppstedt, G. Sletten and S. Törmänen,
First evidence for excited states in ^{101}In.
Phys. Rev. **C53** (1996) 1955.

2. M. Lipoglavšek, J. Cederkäll, M. Palacz, J. Persson, A. Ataç, H. Grawe, C. Fahlander, A. Johnson, A. Kerek, W. Klamra, J. Kownacki, A. Likar, , L.-O. Norlin, J. Nyberg, R. Schubart, D. Seweryniak, G. de Angelis, P. Bernadczyk, Zs. Dombrádi, D. Foltescu, D. Jerrestam, , S. Juutinen, E. Mäkelä, **G. E. Perez**, M. de Poli, H. A. Roth, T. Schizuma, Ö. Skeppstedt, G. Sletten, S. Törmänen and T. Vass,
Stability of $^{100}_{50}Sn_{50}$ *deduced from excited states in* $^{99}_{48}Sn_{51}$.
Phys. Rev. Lett. **76** (1996) 888.

3. M. Palacz, J. Cederkäll, M. Lipoglavšek, J. Persson, A. Atac, J. Blomqvist, C. Fahlander, H. Grawe, A. Johnson, A. Kerek, J. Kownacki, A. Likar, L-O. Norlin, J. Nyberg, R. Schubart, D. Seweryniak, R. Wyss, G. de Angelis, P. Bednarczyk, Zs. Dombrádi, D. Foltescu, D. Jerrestam, S. Juutinen, E. Mäkelä, **G. E. Perez**, M. de Poli, H. A. Roth, T. Shizuma, Ö. Skeppstedt, G. Sletten, S. Törmämen, T. Vass,
In-beam gamma-ray spectroscopy of ^{101}*Cd.*
Nucl. Phys. **A 608** (1996) 227.

4. J. Persson, J. Cederkäll, M. Lipoglavšek, M. Palacz, A. Ataç, J. Blomquist, C. Fahlander, H. Grawe, A. Johnson, A. Kerek, W. Klamra, J. Kownacki, A. Likar, L-O. Norlin, J. Nyberg, R. Schubart, D. Seweryniak, G. de Angelis, P. Bednarczyk, Zs. Dombrádi, D. Foltescu, D. Jerrestam, S. Juutinen, E. Mäkelä, **G. E. Perez**, M. de Poli, H. A. Roth, T. Shizuma, Ö. Skeppstedt, G. Sletten, S. Törmämen, T. Vass,
New spectroscopic data on ^{102}*Cd.*
Acta Physica Polonica B **27** (1996) 2910.

5. J. Kownacki, M. Lipoglavšek, D. Seweryniak, L-O. Norlin, J. Nyberg, J. Cederkäll, M. Palacz, J. Persson, A. Atac, B. Cederwall, F. Lindén, C. Fahlander, H. Grawe, A. Johnson, A. Kerek, W. Klamra, M. Karny, A. Likar, R. Schubart, R. Wyss, E. Adamides, G. de Angelis, P. Bednarczyk, Zs. Dombrádi, D. Foltescu, E. Ideguchi, D. Jerrestam, R. Julin, S. Juutinen, S. Mitarai, E. Mäkelä, **G. E. Perez**, M. Piiparinen, M. de Poli, H. A. Roth, T. Shizuma, Ö. Skeppstedt, G. Sletten, S. Törmämen, T. Vass, A. Virtanen,
High-spin studies of the nuetron deficient nuclei ^{103}*In,* ^{105}*In,* ^{107}*In and* ^{109}*In.*
Nucl. Phys. **A 627** (1997) 239.

6. M. Palacz, J. Cederkäll, M. Lipoglavšek, J. Persson, A. Ataç, J. Blomqvist, H. Grawe, C. Fahlander, J. Iwanicki, A. Johnson, A. Kerek, J. Kownacki, A. Likar, L-O. Norlin, J. Nyberg, R. Schubart, D. Seweryniak, Z. Sujkowski, R. Wyss, G. de Angelis, P. Bednarczyk, Zs. Dombrádi, D. Foltescu, D. Jerrestam, S. Juutinen, E. Mäkelä, **G. E. Perez**, M. de Poli, H. A. Roth, T. Shizuma, Ö. Skeppstedt, G. Sletten, S. Törmämen, T. Vass,
In-beam gamma-ray spectroscopic of very neutron deficient odd-cadmium isotopes.
Acta Physica Polonica B **28** (1997) 309.

7. M. Palacz, J. Cederkäll, M. Lipoglavšek, J. Persson, A. Ataç, J. Blomqvist, H. Grawe, C. Fahlander, J. Iwanicki, A. Johnson, A. Kerek, J. Kownacki, A. Likar, L-O. Norlin, J. Nyberg, R. Schubart, D. Seweryniak, Z. Sujkowski, R. Wyss, G. de Angelis, P. Bednarczyk, Zs. Dombrádi, D. Foltescu, D. Jerrestam, S. Juutinen, E. Mäkelä, **G. E. Perez**, M. de Poli, H. A. Roth, T. Shizuma, Ö. Skeppstedt, G. Sletten, S. Törmämen, T. Vass,
In-beam gamma-ray spectroscopic of ^{103}*Cd.*
Nucl. Phys. **A 624** (1997) 210.

8. J. Persson, J. Cederkäll, M. Lipoglavšek, M. Palacz, A. Ataç, J. Blomquist, C. Fahlander, H. Grawe, A. Johnson, A. Kerek, W. Klamra, J. Kownacki, A. Likar, L-O. Norlin, J. Nyberg, R. Schubart, D. Seweryniak, G. de Angelis, P. Bednarczyk, Zs. Dombrádi, D. Foltescu, D. Jerrestam, S. Juutinen, E. Mäkelä, **G. E. Perez**, M. de Poli, H. A. Roth, T. Shizuma, Ö. Skeppstedt, G. Sletten, S. Törmämen, T. Vass,
In-beam gamma-ray spectroscopic of ^{102}*Cd.*
Nucl. Phys. **A 627** (1997) 101.

9. J . Cederkäll, M. Lipoglavšek, M. Palacz, J. Persson, J. Blomqvist, A. Ataç, C. Fahlander, H. Grawe, A. Johnson, W. Klamra, J. Kownacki, A. Likar, L-O. Norlin, J. Nyberg, R. Schubart, D. Seweryniak, G. de Angelis, P. Bednarczyk, Zs. Dombrádi, D. Foltescu, M. Gorska, D. Jerrestam, S. Juutinen, E. Mäkelä, B. M. Nyakó, **G. E. Perez**, M. de Poli, H. A. Roth,T. Shizuma, Ö. Skeppstedt, G. Sletten, S. Törmanen,
Eur. Phys. Jour. A **1** (1998) 7.

10. D. Sohler, Zs. Dombrádi, J. Timár, J . Cederkäll, M. Lipoglavšek, M. Palacz, J. Persson, J. Blomqvist, A. Atac, C. Fahlander, H. Grawe, A. Johnson, W. Klamra, J. Kownacki, A. Likar, L-O. Norlin, J. Nyberg, R. Schubart, D. Seweryniak, G. de Angelis, P. Bednarczyk, D. Foltescu, M. Gorska, D. Jerrestam, S. Juutinen, E. Mäkelä, B. M. Nyakó, **G. E. Perez**, M. de Poli, H. A. Roth, T. Shizuma, Ö. Skeppstedt, G. Sletten, S. Törmanen,
to be published.